Relaxation dynamics and failures in dense particulate suspensions

Sachidananda Barik

Supervisor: **Dr. Sayantan Majumdar**

Soft and Adaptive Materials Lab
Soft Condensed Matter Group
Raman Research Institute
Bengaluru, India
2024

A thesis submitted for the degree of **Doctor of Philosophy** *to*
Jawaharlal Nehru University, New Delhi

Dedication

to my mother...

Declaration

I hereby declare that the work reported in this doctoral thesis titled **"Relaxation dynamics and failures in dense particulate suspensions"** is entirely original and is the result of the research work carried out by me in the **Soft Condensed Matter Group, Raman Research Institute, Bengaluru, India** under the supervision of **Dr. Sayantan Majumdar**. No part of this work was previously presented for the award of any degree, diploma, fellowship, or similar title to any University or Institution. I have also run the thesis through DrillBit plagiarism software.

Dr. Sayantan Majumdar
(Thesis supervisor)
Raman Research Institute
Bengaluru 560080, INDIA

Sachidananda Barik

Certificate

This is to certify that the dissertation/thesis titled "**Relaxation dynamics and failures in dense particulate suspensions**" submitted by Mr. **Sachidananda Barik**, in partial fulfillment of the requirements for the award of the degree of **Doctor of Philosophy** at the Jawaharlal Nehru University, New Delhi, has not been previously submitted in part or in full for any other degree of this university or any other university/institution.

Prof. Tarun Souradeep
Director
Raman Research Institute
Bengaluru 560080, INDIA

Dr. Sayantan Majumdar
Thesis supervisor
Raman Research Institute
Bengaluru 560080, INDIA

Acknowledgements

From the dawn of time, the beauty and mystery of nature have always inspired human curiosity. The pursuit of research offers a profound opportunity to understand these mysteries and embrace it's beauty. As I take the first step in this endless journey by submitting my PhD thesis, I would like to take this opportunity to express my heartfelt gratitude to all those who have supported and guided me along the way.

My PhD journey has been a remarkable quest for truth, largely due to the exceptional mentorship of my supervisor, Dr. Sayantan Majumdar. His guidance has always been open and welcoming, allowing me to deeply discuss all my doubts and questions without hesitation. He has created an environment free of fear, encouraging me to express my thoughts and feelings openly. His patience in tolerating my occasional immaturity and ignorance has been invaluable. For your outstanding mentorship, advice, and inspiration, I will remain deeply grateful throughout my life.

Throughout my PhD journey, my father has been my pillar of strength and courage. Without his unwavering support, this thesis would not have reached its completion. His words have always inspired me to embrace challenges and pursue my path fearlessly. I am profoundly grateful to have such an exceptional person in my life. I also extend my heartfelt gratitude to my elder brothers (Dipu Bhai and Debu Bhai), whose significant contributions have been vital in realizing this dream. Additionally, I am deeply thankful to my family members (Tapu, Soni, Dada, Khudi, Vandana Di, and Mauni Di) for their continuous encouragement and support throughout this journey.

The teachings from my ashram (Matrubihar) have been invaluable in helping me navigate the challenges and ups and downs of this journey. I am profoundly grateful to Matrubihar and all its members for their benevolence. In particular, I extend my deepest gratitude to my teachers, Sanjay Kumar Mohapatra and Chinmaya Kumar Mahapatra, for their visionary advice and guidance, which have been invaluable assets throughout

this journey.

My initial inspiration to pursue a PhD came from Prof. Lambodar Prasad Singh. During my master's program, our in-depth discussions encouraged me to view science as a way to explore the mysteries of nature and deepened my passion for the field. His unwavering motivation throughout this journey has been invaluable. I am deeply grateful for his guidance and encouragement.

I would like to express my gratitude to Prof. Ajay K. Sood for his valuable input in my research. Working with him has been a remarkable experience and an important learning opportunity.

I extend my sincere thanks to Prof. Ranjini Bandyopadhyay and Prof. Pramod Pullarkat for being on my thesis advisory committee. Their constructive feedback and suggestions have significantly strengthened my work. During my time at RRI, I had the opportunity to learn from an outstanding group of professors. I would like to thank Prof. V. A. Raghunathan, Prof. Yashodhan Hatwalne, Prof. Arun Roy, and Dr. Gautam Vivek Soni for their insightful teachings in Soft matter science during my coursework.

I would like to express my heartfelt gratitude to Radhakrishna Sir, who served as our department secretary during the first half of my PhD, for his exceptional personality and outstanding secretarial skills. I also appreciate our former secretary Amudha and our current secretary Chaithanya for their seamless management of all general departmental tasks. A special thanks to Murali Anna, Raja Anna, Mahadeva Anna, and Shiva Anna for their continuous efforts in maintaining our department and lab workspace.

Furthermore, I am deeply grateful to K.M. Yatheendran for his invaluable assistance with SEM, Confocal, and AFM during my research work.

I am profoundly thankful to the RRI workshop team for their exceptional craftsmanship in designing and constructing the crucial setups and components required for my research. My appreciation also extends to the RRI library staff, IT department, canteen staff, and security personnel for their consistent support. A heartfelt thank you goes to the RRI Administration for their steadfast support and assistance throughout these years. Their dedication, especially during the challenging periods of the COVID lockdowns, was instrumental in helping us manage and overcome those difficult times.

I am deeply thankful to my lab senior, Dr. Sebanti Chattopadhyay, for her exceptional dedication to maintaining a healthy research environment. Her passion for research and strong leadership qualities have greatly influenced me. On a personal level, her care for my mental and physical well-being, her guidance in cultivating patience, and the opportunities for open and rigorous scientific discussions have significantly shaped my

approach to addressing research challenges. I would like to express my sincere gratitude to all my collaborators: Akhil Mohanan for his ultimate sincerity and dedication, Dr. Pradip Kumar Bera, and Dr. Vinutha H.A., for their insightful discussions and unwavering support in my research work. I am grateful to Subhransu Dhar and Swarnadeep Bakshi for their significant contributions in fostering my sincerity and learning during the early stages of my PhD. My heartfelt thanks to Vaisakh V M and Sharadhi Nagaraja for their many useful discussions and moral support, both personally and professionally. A big thanks to Abhishek Ghadai for taking care of numerous responsibilities in the lab and for his constant support throughout this journey. I appreciate Soumen Bhukta, and Soumyajit Pradhan for their extraordinary talent which has inspired me on many occasions, and Maitri Mandal for her exceptional sincerity and discipline, which have greatly enhanced my own sincerity and dedication to research. I am also grateful to Maneesa, Nandana, and Sukanya for the many memorable moments we shared toward the end of my PhD. I extend my special thanks to Harshini for her unwavering moral support during some of the more difficult times in the final phase of my journey.

Finally, I would like to express my gratitude to all the people with whom I had the opportunity to share my time and gain valuable experiences. I believe that each of you has come into my life for a reason, helping to guide me toward my best possible future. I offer my heartfelt gratitude at the lotus feet of the divine Mother constantly reminding me of the wisdom in the words:

"The path is long, but self-surrender makes it short;
the way is difficult, but perfect trust makes it easy."

Preface

Soft matter encompasses materials that show flow and deformation properties intermediate between Newtonian liquids and crystalline solids. This broad category includes diverse systems like suspensions, polymers, paints, surfactants, food and cosmetic products, granular materials, and biological substances, etc. These materials play a crucial role in our daily lives. What makes these materials particularly fascinating is the fact that the mesoscopic length scales and the relatively weak entropic forces govern their behavior. Because of these weak interactions and the involvement of longer length scales, soft materials exhibit easy deformability and long relaxation time scales. These properties make them suitable candidates for studying non-equilibrium physics and understanding various catastrophic natural phenomena by using them as model systems. Thus, from both the fundamental scientific and industrial application perspectives, the study of these systems is crucial.

This thesis focuses on the flow properties of dense particulate suspensions that form an important class of soft materials. Dense suspensions are formed by dispersing solid particles in a Newtonian liquid at a high volume fractions. Dense suspensions exhibit striking non-Newtonian behaviors, in particular, the phenomena of shear thickening and shear-induced jamming. Many dense particulate suspensions show a stress-induced increase in viscosity known as shear thickening (ST). Depending on the particle volume fraction, applied stress, and nature of interparticle interactions, dense suspensions show a mild or, drastic shear thickening known as continuous shear thickening (CST) or discontinuous shear thickening (DST), respectively. For high enough particle volume fraction and applied stress, many of these systems show a remarkable transformation from a liquid-like state to a solid-like shear jammed (SJ) state. Apart from a fundamental scientific standpoint, these phenomena hold significant potential applications, such as in the development of adaptive materials, liquid body armor, shock absorbers, sensors, and more.

Throughout this thesis, using various model systems, we delve deeply into critical aspects of shear thickening and shear jamming phenomena, including relaxation dynamics, memory effects, shear-induced flow and deformation behavior, the effects of solvent and particle properties, etc. Using shear rheology, in-situ boundary imaging, Particle Imaging Velocimetry (PIV), and various other techniques, we explore the microscopic particle scale dynamics that control the properties of shear thickening systems.

Chapter 1 of this thesis serves as a general introduction to soft matter physics. We particularly focus on what makes soft matter systems unique and why they are so important to study. We also explain some fundamental physics that controls the interesting behavior of these systems. Additionally, we touch upon some essential models that help us grasp the fundamentals of soft matter systems. Lastly, we provide an overview of some important topics related to this thesis.

Chapter 2 is dedicated to the various experimental techniques, particle synthesis protocols, and sample preparation processes used in the thesis.

In Chapter 3, we explore the transient stress relaxation behavior of shear jammed (SJ) dense suspension. For high enough particle volume fraction and applied stresses, many ST dense suspensions show a remarkable transformation from a liquid-like state to a solid-like shear jammed (SJ) state. Interestingly, such solid-like shear jammed state again goes back to the liquid-like state under removal of applied stress or shear rate. However, the underlying particle-scale dynamics leading to such striking, reversible transition of the bulk remains unknown. Here, we study the transient stress relaxation behavior of SJ states formed by a well-characterized dense suspension under a step strain perturbation. We use dense suspension of polystyrene microspheres with polyethylene glycol (PEG) as the solvent. We observe a dramatic transition in stress relaxation behavior that depends on the peak stress developed due to transient step strain perturbation. The stress relaxation behavior changes from a smooth single-step relaxation following a power law cutoff by stretched exponential behavior to a two-step relaxation behavior that develops a sharp discontinuous stress drop at a short time for high enough peak-stress values. Additionally, we observe an interesting behavior of normal stress during the stress relaxation process, which is significantly different from the steady state measurement. We use high-resolution in-situ boundary imaging techniques to understand the particle scale dynamics that control such interesting stress relaxation behavior. High resolution boundary imaging and normal stress measurements confirm that such stress discontinuity originates from the localized plastic events, whereas system spanning dilation controls the slower relaxation process. We also find an intriguing correlation between the nature of transient relaxation

and the steady-state shear jamming phase diagram obtained from the Wyart-Cates model.

In Chapter 4, we investigate the structural memory in the shear jammed system. In Chapter 3 we find that such shear jammed systems show very fast relaxation dynamics where the stress in the system relaxes quickly, so that, the solid like jammed state comes back to the liquid like state when no shear is applied. Here we study the effect of such drastic stress relaxation on the structural relaxation of the particles. Using shear rheology, a step strain of a certain magnitude is applied and the strain is maintained for a time scale much larger than the stress relaxation time-scales. After the complete stress relaxation, we again apply the step strain of the same magnitude and repeat the same process. We observe that under a series of unidirectional step strain perturbation, there is an enhancement in the mechanical response, whereas, under step strain perturbation in the alternative directions, the mechanical response becomes gradually weaker. This is suggestive of the structural memory in the system despite the dramatic stress relaxation process where the stress changes over a few orders of magnitude. We further find that this structural memory is significant only for the volume fractions larger than the minimum volume fraction required for the shear jamming. Using in-situ boundary imaging, shear reversal experiments, and numerical simulations, we explore the possible microscopic mechanism and propose a model that can explain such structural memory in SJ dense suspensions.

Chapter 5 deals with the study of shear thickening behavior in fractal particulate systems. Recent studies indicate that ST systems formed by fractal particles are promising candidates for various practical applications. However, ST in fractal systems remains poorly explored. Here, we experimentally study the ST behavior in suspensions of hydrophilic fumed silica (FS) particles in glycerol. Such a fractal system shows ST behavior at a significantly smaller volume fraction compared to the non-fractal particulate system. Remarkably, unlike nonfractal systems, we observe a strong dependence of the onset stress for ST on the volume fraction of fractal objects. Additionally, we observe a reversible weakening of the ST response that depends strongly on the particle volume fraction as well as the properties of the FS system. Using in-situ boundary imaging, we map out the spatio-temporal flow properties during ST for different FS systems. Using six different types of hydrophilic fumed silica systems of different structural properties, we find that the fractal nature and structural properties, like the internal branching of the fractal aggregates, can qualitatively explain the complex ST behavior of fumed silica systems. We summarized the results by showing the difference in the phase diagram for two different FS systems of completely different structural properties.

In chapter 6, we study the spatio-temporal flow behavior of two well-studied shear-thickening granular suspensions, in the context of the recently reported universal scaling behavior in shear-thickening systems. A phenomenological model proposed by Wyart and Cates shows that the proliferation of stress-activated interparticle frictional contacts can give rise to the phenomena of DST and SJ. Building on this model, recent work proposes and verifies a universal scaling relation for ST systems where two different power-law regimes with a well-defined crossover point are obtained. Nonetheless, the difference in the nature of the flow in these two scaling regimes remains unexplored. Here, using rheology in conjugation with high-speed optical imaging, we study the flow and local deformations in various ST systems. Here we use two standard shear thickening dense suspensions:(i) Cornstarch particles dispersed in glycerol and (ii) Polystyrene particles dispersed in polyethylene glycol (PEG) 400. We observe that with increasing applied stress, the smooth flow changes into a spatio-temporally varying flow across the scaling crossover. We show that such fluctuating flow is associated with intermittent dilatancy, shear-band plasticity, and fracture induced by system-spanning frictional contacts.

Chapter 7 summarizes the critical findings of the thesis. Additionally, the possible open directions and questions that remain to be explored in the future are also highlighted.

Dr. Sayantan Majumdar
(Thesis supervisor)
Raman Research Institute
Bengaluru 560080, INDIA

Sachidananda Barik

List of Publications

1. **S. Barik**, H. A. Vinutha and S. Majumdar, "Signature of structural memory in shear jammed dense suspensions", to be submitted for publication (2024).

2. **S. Barik**, P. K. Bera, A. K. Sood, and S. Majumdar, "Shear thickening of dilute suspensions of fractal silica aggregates", Journal of Non-Newtonian Fluid Mechanics, vol. 328, p. 105 246, (2024).

3. **S. Barik**, A. Mohanan, and S. Majumdar, "Role of plasticity in the universal scaling of shear-thickening dense suspensions" Rheol Acta 63, 291–300 (2024).

4. **S. Barik**, and S. Majumdar, "Origin of two distinct stress relaxation regimes in shear jammed dense suspensions", Physical Review Letters 128 (25), 258002 (2022).

Dr. Sayantan Majumdar
(Thesis supervisor)
Raman Research Institute
Bengaluru 560080, INDIA

Sachidananda Barik

Contents

Dedication i

Declaration iii

Certificate v

Acknowledgements ix

Preface xiv

List of Publications xv

1 Introduction 1

1.1 General introduction to soft matter 2

1.2 Interactions in soft matter 2

1.2.1 van der Waals interaction 2

1.2.2 Electrostatic double layer interactions 3

1.2.3 Steric repulsion 3

1.2.4 Depletion interaction 4

1.2.5 Hydrogen bonding 5

1.2.6 Hydrophobic interactions 5

1.3 Viscoelasticity 5

1.3.1 Linear viscoelastic models 6

1.3.2 Measurement of linear viscoelasticity 8

1.4 Nonlinear Phenomena 9

1.4.1 Normal stress difference 9

1.4.2 Non-Newtonian behavior . . . 9
1.5 Introduction to some special topics . . . 10
1.5.1 Shear thickening . . . 10
1.5.2 Proposed mechanisms for shear thickening . . . 11
1.5.3 Jamming . . . 14
1.5.4 Memory formation in disordered system . . . 17
1.6 Thesis Overview . . . 19
Bibliography . . . 21

2 Experimental Techniques **29**
2.1 Introduction . . . 30
2.2 Experimental Techniques . . . 30
2.2.1 Rheological measurements . . . 30
2.2.2 The MCR 702 Rheometer . . . 31
2.2.3 In-situ optical boundary imaging . . . 34
2.2.4 Scanning Electron Microscope . . . 34
2.3 Particle Synthesis . . . 36
2.3.1 Polystyrene microsphere . . . 36
2.3.2 Silica microsphere . . . 37
2.4 Sample preparation . . . 39
Bibliography . . . 41

3 Origin of two distinct stress relaxation regimes in shear jammed dense suspensions **43**
3.1 Introduction . . . 44
3.2 Materials and methods . . . 45
3.3 Results and discussion . . . 46
3.4 Conclusion . . . 57
3.5 Appendix . . . 60
3.5.1 Appendix-1: Movie description . . . 60
3.5.2 Appendix-2: Shear Jamming Boundary from Wyart-Cates Model: . . . 61
3.5.3 Appendix-3: Estimation of area of contact between the particles: . . . 62
3.5.4 Appendix-4: Estimation of plastic center relaxation time: . . . 63
3.5.5 Appendix-5: Diffusion time scales for the system . . . 64
Bibliography . . . 65

4 Signature of structural memory in shear jammed dense suspension 71
4.1 Introduction . . . 72
4.2 Materials and methods . . . 73
4.3 Results and discussion . . . 74
4.4 Conclusion . . . 85
Bibliography . . . 86

5 Shear thickening of dilute suspensions of fractal silica aggregates 89
5.1 Introduction . . . 90
5.2 Materials and Methods . . . 91
5.3 Results and Discussion . . . 91
5.4 Conclusion . . . 102
Bibliography . . . 103

6 Role of plasticity in the universal scaling of shear thickening dense suspensions 107
6.1 Introduction . . . 108
6.2 Materials and methods . . . 110
6.3 Results and discussions . . . 111
6.4 Conclusions . . . 121
6.5 Appendix . . . 122
6.5.1 Appendix-1: Movie description . . . 122
6.5.2 Appendix-2: Scaling relation . . . 123
Bibliography . . . 125

7 Summary and outlook 131

CHAPTER

ONE

Introduction

"The scientist does not study nature because it is useful; he studies it because he delights in it, and he delights in it because it is beautiful."

- Henri Poincare -

1.1 General introduction to soft matter

The term "Soft Condensed Matter" indicates a wide variety of materials that possess intermediate properties between simple Newtonian liquids and crystalline solids. Materials like polymers, colloids, gels, liquid crystals, foams, emulsions, and bio-materials are few examples of Soft matter [1, 2, 3]. These materials are viscoelastic in nature as they exhibit both viscous and elastic characteristics. As a matter of fact, these are the essential part of our daily life. Soft matter science brings together the principles from physics, chemistry, biology, and material engineering [4, 5, 6]. Such interdisciplinary nature broadens the expertise and also fosters collaborative approaches to problem-solving. The study of soft materials is crucial in various processes of industries like food, cosmetics, pharmaceuticals, and bio-medical industries, or the development of eco-friendly smart and adaptive materials, or addressing the critical environmental concerns.

In soft matter systems, the important length scale occupies a middle ground, bridging atomic dimensions and macroscopic scales. The energy associated with the structural reorganization is comparable to the thermal energy levels in these systems. This confluence of a mesoscopic length scale and the interplay between energy and entropy propels soft materials towards the spontaneous formation of hierarchical, self-assembled structures. Such low energy scales make the system flexible which can be easily deformed through the external stresses induced by electric and magnetic fields, as well as thermal fluctuations. Thus, the influence of Brownian motion emerges as a pivotal factor in these systems. Consequently, the structural relaxation time in typical soft materials is considerably longer compared to that of atomic systems, spanning a range from 10^{-3} to 1 second. Due to such low energy scale and the longer relaxation time, soft materials can be easily driven into the out of equilibrium state. Thus, these systems are the ideal candidates to study the non-equilibrium phenomena.

1.2 Interactions in soft matter

1.2.1 van der Waals interaction

The van der Waals force is a fundamental interaction between any pairs of atoms or molecules even when the atoms have no net charge or permanent dipole moment. Such interaction arises from the interaction between the fluctuating dipoles originating from the fluctuations in their electron distributions [7, 2].

There are three major contributing term to the total van der Waals interaction each of which varies as the inverse sixth power of the distance (r) between two interacting particles ($1/r^6$). These are (i) Keesom interaction: This represents the interaction between two permanent dipoles of polar molecules. (ii) Debye interaction: This is the dipole-dipole interaction between the permanent dipole present in a polar molecule and the induced dipole developed in a non-polar molecule. (iii) London dispersion interaction: The fluctuation in the electron distribution of a non-polar molecule give rise to an instantaneous dipole which can further induce dipole in the neighbouring molecule. The interaction between such transient dipoles refers to London dispersion interaction.

1.2.2 Electrostatic double layer interactions

When the macromolecules are suspended in the liquid with dissolved ions, the surfaces of the macromolecules get charged due to the ionization of the surface group or the absorption of ions to the uncharged surface. As a result, a layer of counter ions will be attracted towards the charged surface. Some of them will form a tight layer of counter ions which are bound to the surface called the Stern layer while others will form a diffused layer of ions close to the surface known as diffuse electric double layer. The presence of such a double layer essentially screens the electrostatic interactions between the macromolecules. Incorporating the Debye-Huckel approximation the electrostatic potential $\psi(r)$ at a distance r from the surface can be expressed as

$$\psi(r) = \psi_0 exp(-\kappa r) \tag{1.1}$$

where $\kappa = \left(\frac{2e^2 z^2 n_0}{\epsilon\epsilon_0 k_B T}\right)^{1/2}$, n_0 = ionic concentration in the bulk solution, ze = charge of the ions [2].

Here, the characteristic length scale κ^{-1} is known as the Debye screening length, which is inversely proportional to the square root of the concentration of the electrolyte. The electrostatic interaction between the charged objects drastically drops to negligible value at a distance greater than the Debye screening length.

1.2.3 Steric repulsion

When two particles, grafted with a polymer layer, approach one another in very close proximity, the concentration of the polymers inside the gap increases (Figure 1.1).

The reduction of entropy of the polymer chains increases the osmotic pressure that leads to a repulsive force. For better colloidal stabilization, the strength of the bond between the polymer and the particle surface needs to be greater than k_BT, and there should not be any significant net attractive interaction between polymers. Here, the interaction strength is influenced by factors such as the length of the polymer chains, the density of the grafted polymers on the particle surface, and the interaction strength between polymer segments and the solvent [2].

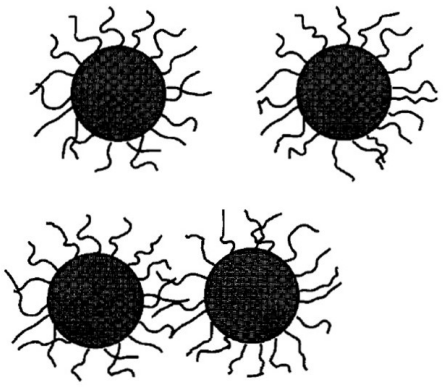

Figure 1.1:
Colloids stabilized with grafted polymers experience a repulsive force in close proximity (figure adapted from [2]).

1.2.4 Depletion interaction

This is an attractive interaction that arises due to osmotic pressure. In addition to the suspended particles, if the solution contains any other particles of intermediate size between suspended particles and the size of the solvent molecules, the depletion interaction becomes important. A classic example is the suspension with dissolved polymers, which do not adsorb to the surface of the particles (Figure 1.2). Around each particle, a region is impassable to the center of the smaller polymeric coils due to the particle and polymeric coil interaction. Whenever two suspended bigger particles come close to each other, the region between the bigger particles becomes inaccessible to the smaller particles. So that the concentration of the smaller particles in this region is less compared to the bulk solution. As a result, the difference in osmotic pressure pushes the particles together [2]. Depletion interaction is always attractive in nature, and its strength primarily depends on the size of the depleting agents (such as polymers or smaller particles) relative to the larger particles,

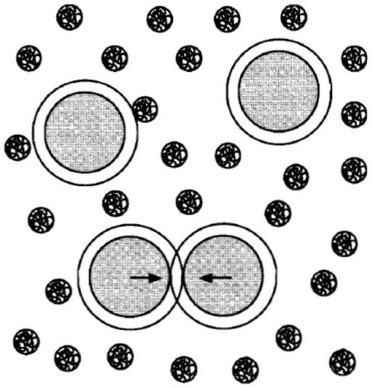

Figure 1.2: Polymer coils of smaller size along with suspended bigger particle result in the depletion attractive force (figure adapted from [2]).

their concentration, and temperature. These factors influence the osmotic pressure and the excluded volume between the particles, which together determine the strength of the depletion interaction.

1.2.5 Hydrogen bonding

Hydrogen bonds exist between electronegative atoms (Oxygen, Nitrogen, Fluorine, and Chlorine) and hydrogen (H) atoms covalently bound with similar electronegative atoms. As the hydrogen atoms get positively polarized and due to their small size, they can strongly interact with the nearby electronegative atom, which results in a hydrogen-mediated bond between two electronegative atoms. The best example is water, where the oxygen atom with its two hydrogens, participates in forming hydrogen bonds with other water molecules (Figure 1.3). The typical strength of hydrogen bonds (10 to $40 kJmol^{-1}$) are typically stronger than the van der Waals bond ($\sim 1 kJmol^{-1}$) and weaker than the covalent or ionic bonds ($\sim 500 kJmol^{-1}$) [7].

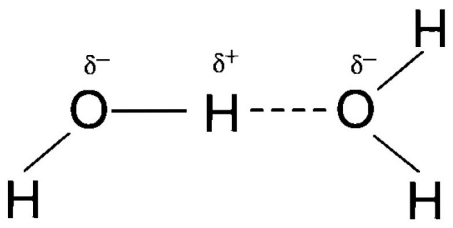

Figure 1.3: Electronegative oxygen atom of a water molecule makes a hydrogen bond with the hydrogen atom of another water molecule (figure adapted from [2]).

1.2.6 Hydrophobic interactions

Such interaction originates due to the entropic effects. The immiscibility or the incompatibility of some inert substances with water is known as the hydrophobic effect. Hydrocarbons and fluorocarbons are some classic examples of hydrophobic substances. Now the significantly strong interactions between these hydrophobic substances in water, which is stronger than their interactions in free space, is considered as the hydrophobic interaction. This interaction plays a crucial role in a wide variety of phenomena such as molecular self-assembly, micelle formation, formation of biological membrane structure, etc.

1.3 Viscoelasticity

Solid and liquid are two common forms of matter. When subjected to an external force or stress, a solid deforms, but it exhibits a remarkable ability to return to its original

shape once the stress is removed, known as elasticity, which arises from the restoring forces within the material. Whereas a key characteristic of liquids is viscosity. It is the measure of a liquid's resistance to flow, which also involves an inherent dissipation of energy. High-viscosity liquids, like honey, resist flow more strongly, while low-viscosity liquids flow more easily, akin to water. But many materials, called viscoelastic materials, exhibit both viscous (liquid-like) and elastic (solid-like) properties, depending on the applied stress or strain and the deformation rate. This dual nature is a consequence of the material's internal structure and molecular interactions [8, 9, 10, 11]. Pitch, gum rubber, silk, and glass are a few examples of viscoelastic materials [9].

1.3.1 Linear viscoelastic models

The stress (σ) applied to a solid is directly proportional to the resulting strain (γ) within the material, as long as the material remains within its elastic limit, known as Hooke's law for solids.

$$\sigma = G\gamma \tag{1.2}$$

where G is the elastic modulus of the material.

Similarly for a liquid, the applied stress is proportional to the strain rate ($\dot{\gamma}$), within the fluid, known as Newton's law of liquids.

$$\sigma = \eta\dot{\gamma} \tag{1.3}$$

where η is the dynamic viscosity of the liquid.

But for a viscoelastic materials both σ and γ could be function of time. In general one can express it as

$$\left(1 + \alpha_1\frac{\partial}{\partial t} + \alpha_2\frac{\partial^2}{\partial t^2} + ... + \alpha_n\frac{\partial^n}{\partial t^n}\right)\sigma = \left(\beta_0 + \beta_1\frac{\partial}{\partial t} + \beta_2\frac{\partial^2}{\partial t^2} + ... + \beta_n\frac{\partial^m}{\partial t^m}\right)\gamma \tag{1.4}$$

In some special case, if β_0 is the only non-zero coefficient and $\beta_0 = G$, then we have the Hooke's law for linear solid behavior ($\sigma = G\gamma$). Similarly if β_1 is the only non-zero coefficient and $\beta_1 = \eta$, then we have the Newton's law of liquids ($\sigma = \eta\dot{\gamma}$).

Now, taking both $\beta_0(= G)$ and $\beta_1(= \eta)$ as non-zero and other coefficients to be zero, we have

$$\sigma = G\gamma + \eta\dot{\gamma} \tag{1.5}$$

which is a simple viscoelastic model called "Kelvin-Voigt (KV) model". For a constant

stress $\bar{\sigma}$ at $t = 0$, from KV model we can have the growth of strain γ as

$$\gamma = (\bar{\sigma}/G)\,[1 - exp(-t/\tau_k)] \tag{1.6}$$

where $\tau_k = \eta/G$ is called the "retardation time". In a simplified term one can express the KV model as the parallel combination of a spring and a dashpot (Figure 1.4(a)), where the spring and dashpot represent the elastic and viscous components, respectively.

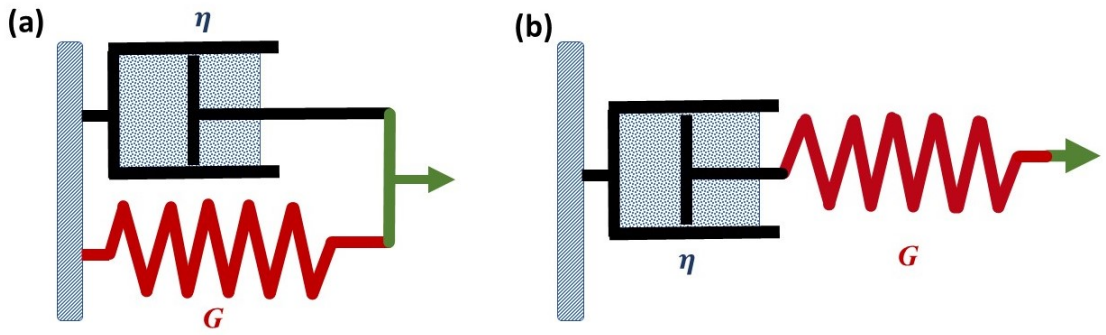

Figure 1.4: Simple linear viscoelastic models: (a) The Kelvin-Voigt model (b) The Maxwell model.

Another simple viscoelastic model is the "Maxwell model", which can be obtained from the general viscoelastic equation if α_1 and β_1 become the only non-zero coefficient. Taking $\alpha_1 = \tau_m$ and $\beta_1 (= \eta)$ as before, we have

$$\sigma + \tau_m \dot{\sigma} = \eta \dot{\gamma} \tag{1.7}$$

For a constant strain rate ($\bar{\dot{\gamma}}$) at $t = 0$, we can have the stress growth as

$$\sigma = \eta \bar{\dot{\gamma}}\,[1 - exp(-t/\tau_m)] \tag{1.8}$$

If $\dot{\gamma}$ is constant for $t < 0$ and $\dot{\gamma} = 0$ at $t = 0$, then for $t \geq 0$ we have

$$\sigma = \eta \bar{\dot{\gamma}} exp(-t/\tau_m). \tag{1.9}$$

This indicates the stress relaxation behavior from its equilibrium value where τ_m is the "relaxation time". One can express the Maxwell model as the series combination of a spring and a dashpot (Figure 1.4(b)) [8].

1.3.2 Measurement of linear viscoelasticity

To gain insight into the viscoelastic properties exhibited by materials, one must delve into the field of rheology, the study of the flow and deformation behavior of the systems. Mostly two different rheological methods are used to study the linear viscoelastic properties of the system: static and dynamic [8].

In the static method, a step stress or strain is applied and the variation of subsequent strain or stress is observed. The constant stress measurements are known as the "creep" tests and the constant strain measurements are known as relaxation tests.

In dynamic testing, an oscillatory strain is employed, which enables coverage across an extensive frequency range and indeed particularly beneficial for materials with a broad spectrum of relaxation times. When a small amplitude sinusoidal strain is applied to the system the stress in the system will also oscillate sinusoidally at the same frequency but with a phase shift of δ (Figure 1.5).

$$\gamma = \gamma_0 \sin \omega t \tag{1.10}$$

$$\sigma = \sigma_0 \sin(\omega t + \delta) \tag{1.11}$$

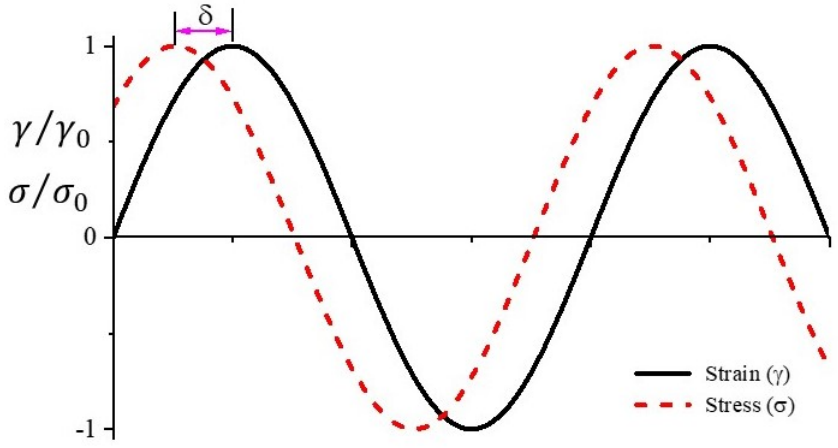

Figure 1.5: Oscillatory input strain γ and corresponding stress σ with a phase shift δ.

The stress can be decomposed into two parts with the same frequency. One part is in phase with the strain wave and other is 90° out of phase with strain. In general sinusoidally varying stress can be written as

$$\sigma = \gamma_0 \left[G'(\omega) \sin(\omega t) + G''(\omega) \cos(\omega t)\right] \tag{1.12}$$

where G' is known as "storage" modulus which represents the storage of elastic energy and G'' is called as "loss modulus" which represents the viscous dissipation of energy [8, 9, 11].

1.4 Nonlinear Phenomena

While the linear viscoelastic framework can accommodate a diverse array of rheological behaviors, the range of stress or strain over which the material behaves linearly is very limited. Beyond this range, material properties can undergo changes under applied stress or strain and can also exhibit time dependence. Beyond the linear regime, significant nonlinear effects may arise, such as the development of normal stress differences, shear thinning, and shear thickening.

1.4.1 Normal stress difference

When a viscoelastic material undergoes shear, it experiences a shear stress component and a normal stress component [8, 9]. Under small deformations within the linear viscoelastic regime, the three normal stress components have the same value, equivalent to isotropic ambient pressure. In the case of simple shear flow in the x-direction with a velocity gradient in the y-direction, the three normal stress components can be denoted as σ_{xx}, σ_{yy}, and σ_{zz}. As deformation increases, the generation of unequal normal stress components gives rise to a non-zero normal stress difference, denoted as $N_1 = \sigma_{xx} - \sigma_{yy}$ and $N_2 = \sigma_{yy} - \sigma_{zz}$. While for Newtonian fluids like water, the values of N_1 and N_2 are typically zero, for non-Newtonian fluids, N_1 is often larger than N_2. One notable example of a non-zero normal stress difference is the rod-climbing phenomenon, also known as the Weissenberg effect, where an elastic solution gravitates towards the axis of rotation under stirring, unlike in Newtonian fluids.

1.4.2 Non-Newtonian behavior

As discussed earlier, viscosity in a fluid signifies the extent of energy dissipation under shear, defined as the ratio of shear stress to the corresponding shear rate. For a Newtonian fluid, it is an inherent material property that is independent of the shear rate. Dispersing small particles or polymers in a Newtonian liquid can induce non-Newtonian behavior, wherein viscosity becomes a function of applied shear rate [11, 10].

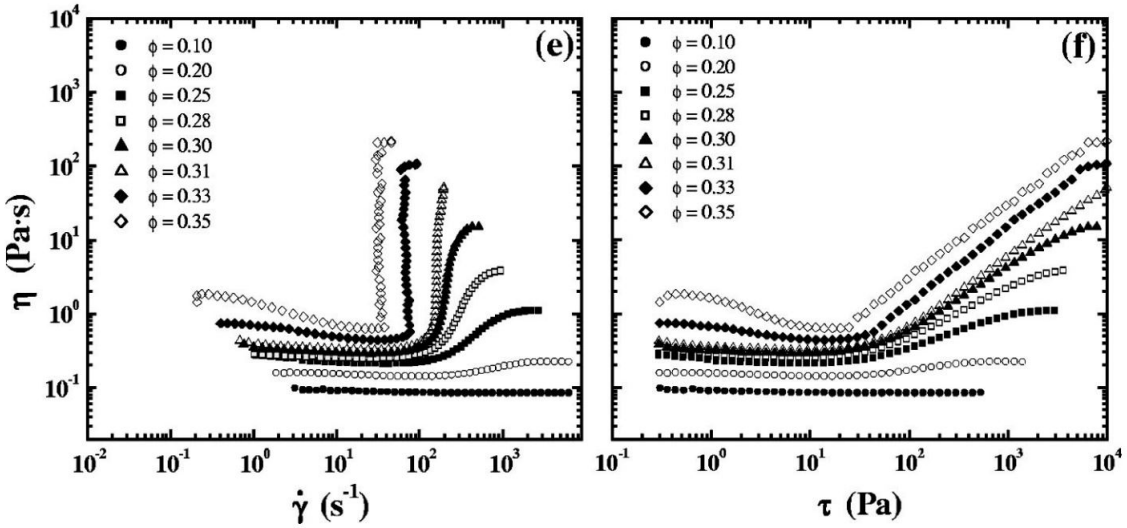

Figure 1.6: Variation of viscosity with shear rate (e) and stress (f) reflects the CST to DST transition with increasing volume fraction ϕ for the suspension of calcium carbonate in poly-ethylene glycol (PEG) (figure adapted from [12]).

When the energy dissipation rate or the viscosity of the system decreases with increasing shear rate, the process is known as shear thinning. A notable example of a shear-thinning sample is a common household product: paint. When the paint is at rest, it has a certain viscosity, but the viscosity decreases as shear is applied during stirring or brushing. This shear-thinning behavior allows the paint to flow more easily, facilitating smooth application on surfaces.

Conversely, the increase in energy dissipation rate with the applied shear rate is considered as shear thickening. In other words, the viscosity increases with an increase in shear rate or shear stress for a shear thickening suspension. A widespread example is the dense suspension of cornstarch particles in water. It behaves like a liquid at rest, but its resistance to flow increases significantly under shear and can exhibit properties like a solid.

1.5 Introduction to some special topics

1.5.1 Shear thickening

As discussed earlier, the shear-induced enhancement of the viscosity is considered as shear thickening. The increase in viscosity with shear rate or stress significantly depends on the volume fraction of the suspension, representing the fraction of solid particles in the liquid.

Above a minimum volume fraction, shear thickening begins to develop gradually with increasing shear rate. When the rise in viscosity is relatively modest, typically several tens of percentage points over a few decades of shear rate, it is considered continuous shear thickening (CST) [13, 14, 15].

In many shear-thickening systems, as the sample's volume fraction increases, the rise in viscosity becomes more prominent and pronounced. Above a specific volume fraction and beyond a certain shear rate, the viscosity and shear stress exhibit a discontinuous jump by orders of magnitude. This abrupt increase in viscosity under shear is known as discontinuous shear thickening (DST). Although this dramatic increase in viscosity distinguishes DST from continuous shear thickening (CST), the minimum stress required for the onset of shear thickening remains more or less independent of the volume fraction for both CST and DST regimes (Figure 1.6) [12, 16, 17, 18, 19, 20].

1.5.2 Proposed mechanisms for shear thickening

Flow-induced Hydroclustering

When two colloidal particles come into proximity, increasing hydrodynamic pressure between them results in the expulsion of fluid from the intervening gap. At short distances, the hydrodynamic force rises inversely with the separation between the surfaces of the particles. Therefore, when external shear stresses drive the particles close together, lubrication hydrodynamics strongly couple the relative motion of the particles (Figure 1.7). This robust hydrodynamic coupling leads to the formation of hydroclusters, which are nothing but flow-induced density fluctuations driven and sustained by the applied shear stress [21, 13].

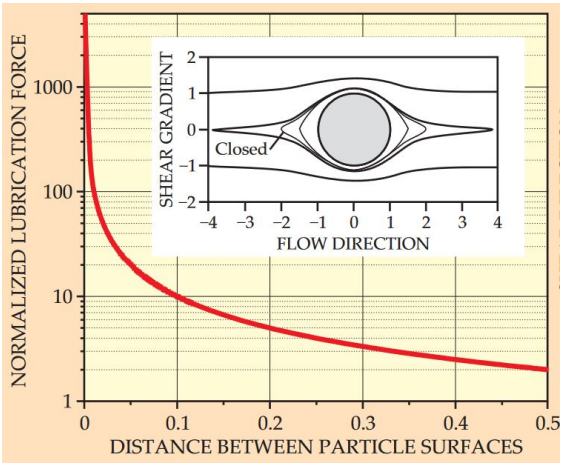

Figure 1.7: Lubrication force variation with the distance between the particles surface. Inset: trajectory of a particle around a reference particle under shear flow (figure adapted from [13]).

As the particle concentration is higher in the hydrocluster, they are capable of dissipating significant energy. When a signif-

icant number of hydroclusters are formed under shear, the flow can be significantly disrupted. This results in an enhancement of the viscosity of the system. [22].

These transient hydroclusters stand out as the distinctive characteristic of the shear-thickening state. The formation of hydroclusters, as it turns out, is reversible in nature. Consequently, by reducing the applied shear rate, one can restore the suspension to a stable state with lower viscosity.

In principle, an increase in volume fraction should allow particle clusters to grow larger and become system-spanning, potentially leading to Discontinuous Shear Thickening (DST). However, it is observed that the hydrocluster model can only explain a mild increase in viscosity, approximately a factor of 2, and it fails to reproduce the order of magnitude increase in viscosity as observed in experiments. Nevertheless, the model successfully reproduces the onset stress for shear thickening [23, 24, 25].

Order–disorder transition

In some studies, it has been observed that the transition to DST results from a change in microstructure – specifically, a transition from ordered layers to a disordered state as the shear rate increases from a lower to a higher value [26, 27]. In other words, the interaction between the shear force and the interparticle force leads to the formation of layers of surfaces that glide over each other in the flow direction. When the relative velocity between these neighboring surfaces increases, this results in an increase in the shear stress transmitted from one surface to the next through the interstitial fluid. At a critical shear stress, the coupling of shear stress between the different layers of surfaces becomes just enough to overcome the forces between the spheres in a single layer, which initially held them in place. As a result, some sections of the ordered surfaces move into eddies and cause the onset of disordered flow. The additional energy these disordered spheres require when they interact during flow causes them to jam into each other, resulting in a discontinuous jump in the apparent viscosity at the instability point.

However, in many cases, DST is observed without a clear order-disorder transition in microstructure [12, 28, 29]. This suggests that while the order-disorder transition is a plausible explanation for DST, it is not a necessary condition. Nevertheless, the model also successfully predicts the onset of shear thickening.

Dilatancy

Dilatancy is a shear-induced mechanism frequently observed in granular systems. When a densely packed granular system experiences shear forces, the particles cannot easily take a direct path and attempt to navigate around each other. This results in an overall increase in the volume of the granular packing, a phenomenon referred to as dilation.

In the case of dense particulate suspensions, when the particle packing dilates under shear, it creates additional space within the packing. This dilation causes the liquid from the boundary to be drawn into the interparticle voids. Visually, this transformation can be observed as the surface of the suspension shifts from being wet and shiny to becoming rough.

Such dilatancy is often observed in conjunction with DST. However, it has been noted through various observations that not all dilatant systems necessarily exhibit shear thickening. Subsequent studies have revealed that while dilation is a necessary condition, it alone is not sufficient for the occurrence of DST.

According to more recent studies [30, 17], during shear flow, when a particulate system undergoes dilation, it imparts normal stress on the confining boundary. This confinement, in turn, applies a restoring stress to the system, transmitted through the particle contact network spanning the entire system. As the shear rate increases, this frictional contact network supports the rise in shear stress, which is proportional to the normal stress, ultimately causing DST. While this picture successfully explains the normal stress behavior and the influence of boundary conditions on shear thickening, it could not predict the slope of the viscosity curve.

Lubrication to frictional contact

As discussed previously, although the hydrocluster mechanism can successfully explain the onset of shear thickening and mild increase in viscosity, such model is not sufficient to capture the drastic increase in viscosity experimentally observed during DST. Incorporating both hydrodynamic and frictional interactions between particles, Seto et al. [18] introduced a numerical model that successfully captures the strong shear thickening, including the drastic increase in viscosity during DST in dense suspension. They observed that the DST is completely absent if the particles become frictionless, even at high volume fractions approaching the jamming point. The essential feature of their model is the stress induced transition from a lubrication dominated regime to friction dominated regime. It further highlights the importance of critical stress that separates the low viscosity, fric-

tionless state from the high viscosity, frictional DST/shear jammed state. Remarkably, the critical stress encompasses the repulsive interaction strength between the particles ensuring the homogeneity of the dense suspension. The role of friction becomes more pronounced as the volume fraction increases. They further show that friction leads to the formation of a percolating network of frictional contacts among particles when subjected to shear (Figure 1.8). This network is essential for the system to sustain applied stress, which is a characteristic feature of DST. The presence of frictional contacts enhances the mechanical properties of the suspension, allowing it to transition from a low-viscosity to a high-viscosity state.

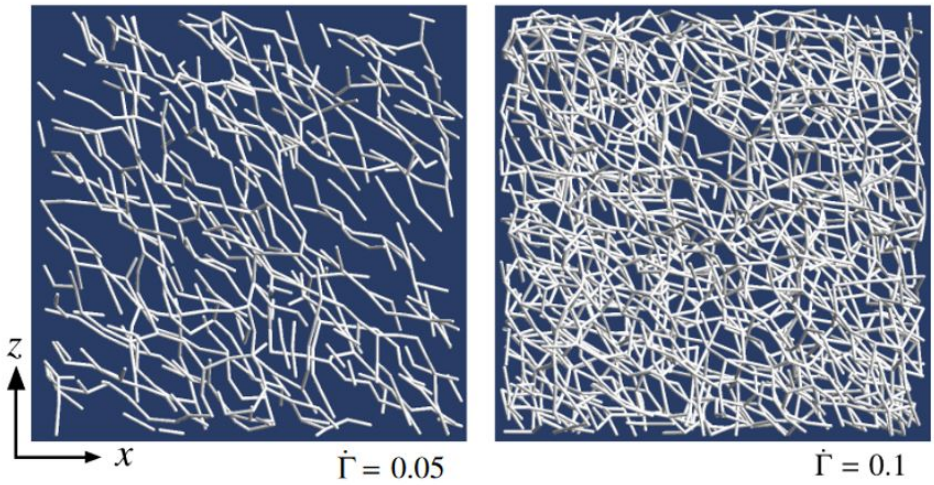

Figure 1.8: Frictional contacts represented as bonds at the two different shear rate (figure adapted from [18]).

Apart from this study, incorporating the frictional contacts into consideration, the Wyart-Cates (W-C) model also gives a microscopic insight into the shear-induced increase in viscosity for the steady-state flow that we will discuss in chapters 3 and 6 [19].

1.5.3 Jamming

When the system can bear any significant applied stress without showing any structural deformation, then the system is said to be in jammed condition. More precisely, jamming refers to the emergence of mechanical rigidity in a disordered system due to the formation of stress-bearing contact networks under applied load. A wide variety of systems comes under the category of 'jammed system,' which includes foams, dense granular matter, colloids, etc [31, 32, 33, 34, 35, 36, 37, 38, 39]. Most of these systems are inherently

jammed and possess a well-defined yield stress. In general, there are two basic parameters that control the jamming transition: (1) Density of the system, (2) Applied stress/load. Depending on the value of these parameters, a system can be found in the jammed or unjammed state. The jamming phase diagram proposed by Liu and Nagel beautifully represents this picture of the jamming transition (Figure 1.9) [32]. Such jamming transition is often associated with increased correlation length and relaxation time scales [40]. This type of jamming, which occurs at zero stress (on the density axis of Figure. 1.9) is a purely geometric phenomenon.

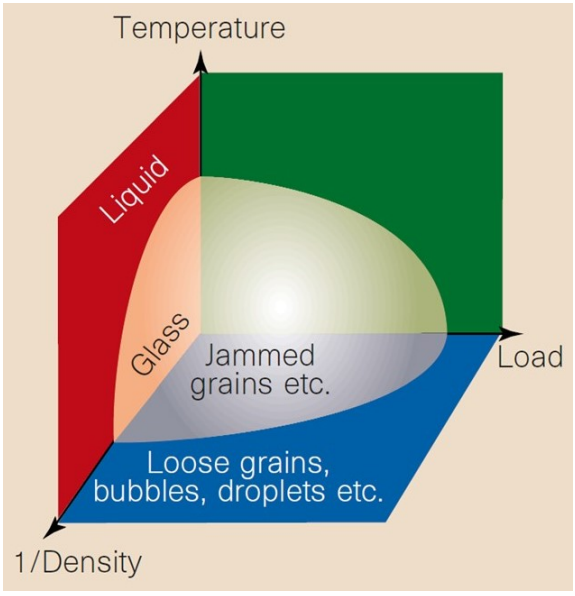

Figure 1.9: The general jamming phase diagram proposed by Liu and Nagel (figure adapted from [32]).

From the Liu and Nagel jamming phase diagram, it is known that for a system to be in a jammed state the density of the system must be above a critical value. Such a jammed state is known as an isotropic jammed state. In the Liu and Nagel jamming phase diagram, LOAD always leads to "flow". If we increase the load at a fixed density, jammed solids can become loose. But in certain cases, even if the density of the system is below the critical density for isotropic jamming, the system can be driven into the jammed state under applied shear stress known as the shear jamming (SJ) [41, 42, 43, 44, 45]. Such a shear jammed state is apparent within two critical densities. Below the lower critical density, there will be no shear jamming, and at the higher critical density, the system will be in the isotropic jammed state (Figure 1.10). Such shear jammed state sometimes referred as a fragile state, as it is highly sensitive to the direction of the shear [46].

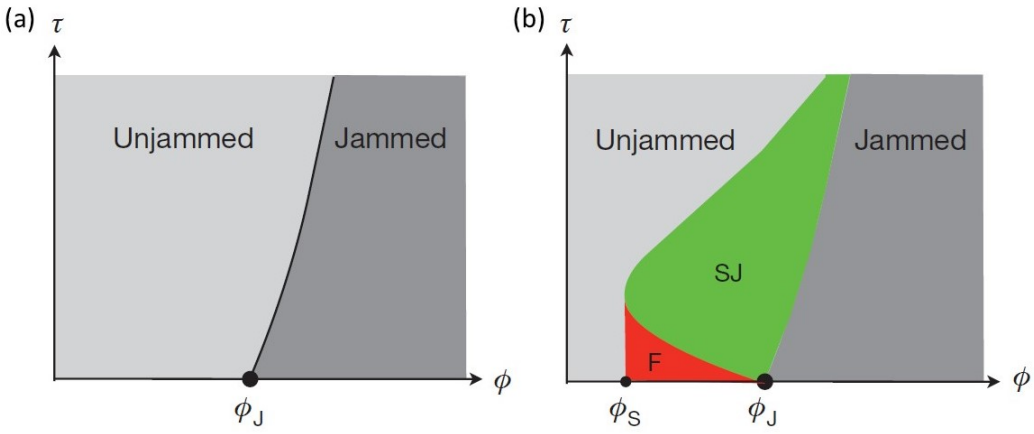

Figure 1.10: (a)The Liu– Nagel jamming phase diagram in the load-density plane (b) Modified jamming phase diagram showing shear jammed (SJ) and fragile (F) regime. ϕ_S and ϕ_J are the lower and upper critical densities, respectively (figure adapted from [41]).

In the case of dense particulate suspensions showing DST, the system can also transformed into the solid-like jammed state under appropriate conditions of the density of the solid particles and applied shear stress (Figure 1.11) [47, 48, 49, 50, 51]. However, unlike static jammed systems and dry granular systems, the shear jammed state of a dense particulate suspension shows rapid relaxation dynamics upon shear cessation [52, 53]. This makes the shear jamming in dense particulate systems very special. Such systems show a dramatic transition from a liquid-like state to a solid-like state under shear, but once the applied shear rate or stress is removed, they immediately return to the liquid-like state—and this is what makes shear jamming in dense suspensions so exciting and interesting [47].

So far, the microscopic mechanism governing the transition from DST to SJ is not understood properly and has been an intense topic of research. Recent simulation pictures highlight that the shear-induced constraints on sliding and rolling degrees of freedom can induce shear jamming in dense particulate suspension (Figure 1.12) [51]. Such constraints can arise from various properties of the particle such as particle shape, surface roughness, and surface chemistry [54, 55, 48]. Experimental observation also highlights the importance of surface chemistry, which shows that inter-particle hydrogen bonding can play an important role in controlling shear jamming [48].

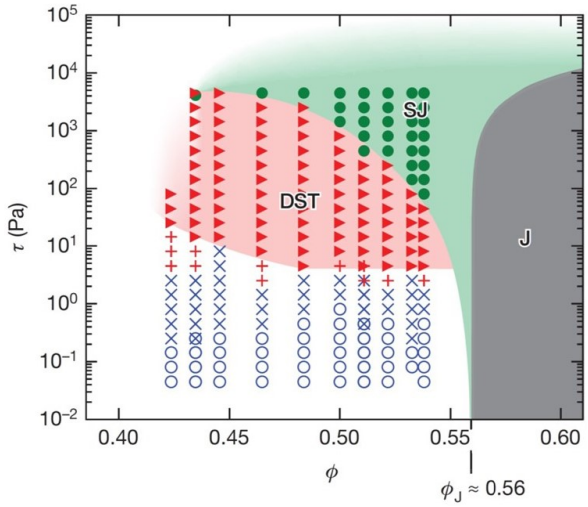

Figure 1.11: State diagram for the shear thickening dense suspension of cornstarch in water, showing DST and shear jamming (SJ) (figure adapted from [47]).

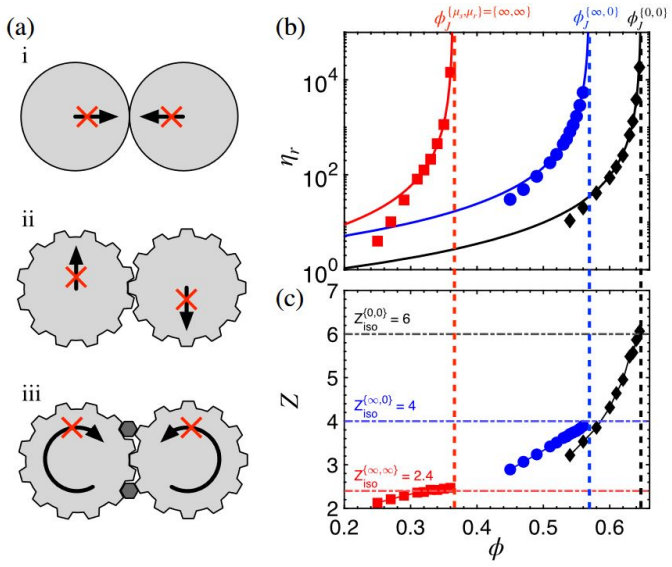

Figure 1.12: (a) Cartoon representation of different types of constraints. (i) hard sphere, (ii) sliding friction, (iii) both sliding and rolling friction. (b) Relative viscosity and (c) contact number as a function of volume fraction (figure adapted from [51]).

1.5.4 Memory formation in disordered system

Disordered, out-of-equilibrium materials can retain information about their perturbation/structural history. Understanding how memory is encoded, stored, and retrieved in these disordered systems can uncover underlying mechanisms related to structural rearrangements, energy landscapes, dynamical processes, and the fundamental principles

governing the complex behavior of these materials. In addition, this knowledge can be the backbone of the design and development of stimuli-responsive materials with optimized performance and tailored properties [56].

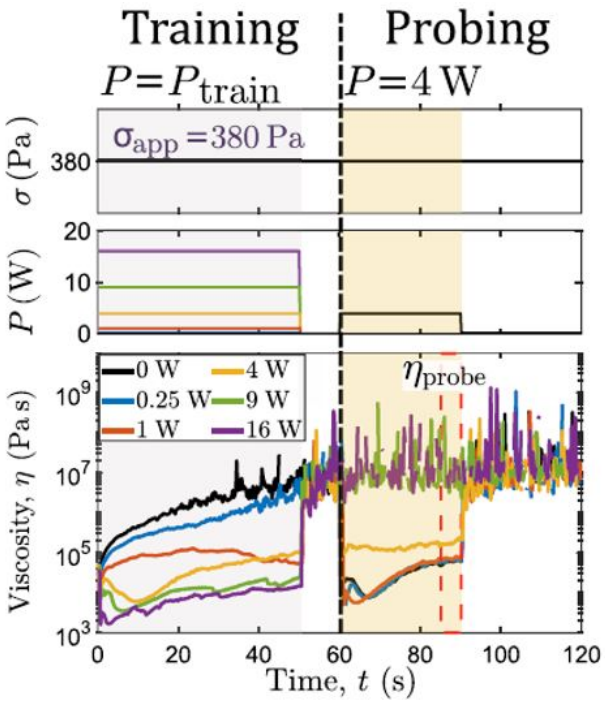

Figure 1.13: Experimental protocol and corresponding result for encoding memory in SJ system. The variation of stress σ, acoustic power $P(W)$, and viscosity η with time is shown in the top, middle, and bottom panels respectively. A constant shear stress σ_{app} = 380 Pa was applied to make the system shear jammed. The acoustic perturbation of different powers $P(W)$, as marked in the legend, was applied for 50 s as the training (grey patch) and then a constant acoustic power of 4 W was applied from 60 to 90 s (yellow patch) in all case as the probing (figure adapted from [57]).

In nature, we find these disordered out-of-equilibrium systems sometimes remember the most recent direction in which it was driven by some external influence [58, 59], and sometimes the magnitude of the specific stimulus it has experienced [60, 61]. Under repeated or cyclic deformation, these systems can remember the amplitude of the deformation applied to it [62, 63, 64, 65]. Apart from this simplest form of memory, systems can also exhibit the return point memory where the system retains the information of its previous configuration when subjected to cyclic loading [66, 67]. In many cases, one can also store and retrieve multiple memories in the system [67, 68, 65].

Often these interesting memory phenomena are observed in slowly relaxing systems such as yield stress or glassy systems [59, 69, 70, 63, 64, 65]. Recent studies also focus on

the memory effect in the fast-relaxing systems, such as shear thickening or shear jammed dense suspension [57, 71, 72, 73]. In shear thickening system, a recent study observed the formation of heterogeneous high-stress regions that retain their shape under cyclic perturbation [72]. It is also observed that the speed of the jamming front propagation is quite sensitive to the pre-shear applied to the shear-jammed system [73]. A very recent work nicely encoded structural memory in the shear-jammed state through acoustic perturbations [57]. Here, the shear-jammed state is formed under constant stress application, and the evolution of the force chain network is observed under acoustic training of different powers (Figure 1.13). They demonstrate that the shear jammed state trained with high-power acoustic perturbation does not get affected by the further perturbation of lower power. In addition to the primary force chain network in the compressive axis, which is primarily responsible for shear jamming, the high-power acoustic perturbation in training can generate many secondary force chain networks along the maximum extensional axis. The presence of these secondary force chain networks plays a crucial role in maintaining the shear-jammed state during the external acoustic perturbation of lesser power than the training power.

1.6 Thesis Overview

In this section, we are giving a brief description of the construction of this thesis.

Chapter 2: In this chapter, we discuss the details of the experimental techniques like Rheology and different microscopic techniques that we used in this thesis work. We also discuss the synthesis protocol for polystyrene microspheres, and silica microspheres in this chapter. Furthermore, It also covers the preparation protocols for the samples used for this thesis work.

Chapter 3: In this chapter, we study the transient stress relaxation phenomena in SJ dense suspensions and explore the particle scale dynamics controlling its behavior.

Chapter 4: Here we explore the effect of stress relaxation on structural relaxation of the shear jammed state where we investigate the microscopic origin of a novel structural memory.

Chapter 5: In chapter 5, we study the shear thickening behavior of the fractal system. Here, we use fumed silica samples of different structural properties and explore the effect of complex internal structure of the particles on shear thickening phenomena.

Chapter 6: In this chapter, we investigate the spatiotemporal fluctuation in the flow profile during shear thickening phenomena and establish its correlation with the universal

scaling relation proposed for such systems.

Chapter 7: The thesis concludes with this chapter which also gives the outlook for the possible future direction related to this thesis work.

Bibliography

[1] Pierre-Gilles De Gennes. Soft matter. *Science*, 256(5056):495–497, 1992.

[2] R.A.L. Jones. *Soft Condensed Matter*. Oxford Master Series in Physics. OUP Oxford, 2002.

[3] M. Doi. *Soft Matter Physics*. OUP Oxford, 2013.

[4] Daan Frenkel. Soft condensed matter. *Physica A: statistical mechanics and its applications*, 313(1-2):1–31, 2002.

[5] T.C. Lubensky. Soft condensed matter physics. *Solid State Communications*, 102(2):187–197, 1997. Highlights in Condensed Matter Physics and Materials Science.

[6] Sidney R Nagel. Experimental soft-matter science. *Reviews of modern physics*, 89(2):025002, 2017.

[7] Jacob N. Israelachvili. *Intermolecular and Surface Forces (Third Edition)*. Academic Press, Boston, 2011.

[8] H.A. Barnes. *A Handbook of Elementary Rheology*. Raymond F. Boyer Library Collection. University of Wales, Institute of Non-Newtonian Fluid Mechanics, 2000.

[9] C.W. Macosko. *Rheology: Principles, Measurements, and Applications*. Advances in interfacial engineering series. VCH, 1994.

[10] R.G. Larson. *The Structure and Rheology of Complex Fluids*. Topics in Chemical Engineering. OUP USA, 1999.

[11] T.G. Mezger. *The Rheology Handbook: For Users of Rotational and Oscillatory Rheometers*. Coatings compendia. Vincentz Network, 2006.

[12] Ronald G. Egres and Norman J. Wagner. The rheology and microstructure of acicular precipitated calcium carbonate colloidal suspensions through the shear thickening transition. *Journal of Rheology*, 49(3):719–746, 05 2005.

[13] H. A. Barnes. Shear-thickening ("dilatancy") in suspensions of nonaggregating solid particles dispersed in newtonian liquids. *Journal of Rheology*, 33(2):329–366, 1989.

[14] John R. Melrose and Robin C. Ball. Continuous shear thickening transitions in model concentrated colloids—the role of interparticle forces. *Journal of Rheology*, 48(5):937–960, 2004.

[15] Norman J. Wagner and John F. Brady. Shear thickening in colloidal dispersions. *Physics Today*, 62(10):27–32, 2009.

[16] Eric Brown, Nicole A Forman, Carlos S Orellana, Hanjun Zhang, Benjamin W Maynor, Douglas E Betts, Joseph M DeSimone, and Heinrich M Jaeger. Generality of shear thickening in dense suspensions. *Nature materials*, 9(3):220–224, 2010.

[17] Eric Brown and Heinrich M Jaeger. Shear thickening in concentrated suspensions: phenomenology, mechanisms and relations to jamming. *Reports on Progress in Physics*, 77(4):046602, apr 2014.

[18] Ryohei Seto, Romain Mari, Jeffrey F. Morris, and Morton M. Denn. Discontinuous shear thickening of frictional hard-sphere suspensions. *Phys. Rev. Lett.*, 111:218301, Nov 2013.

[19] M. Wyart and M. E. Cates. Discontinuous shear thickening without inertia in dense non-brownian suspensions. *Phys. Rev. Lett.*, 112:098302, Mar 2014.

[20] Romain Mari, Ryohei Seto, Jeffrey F. Morris, and Morton M. Denn. Shear thickening, frictionless and frictional rheologies in non-brownian suspensions. *Journal of Rheology*, 58(6):1693–1724, 2014.

[21] John F Brady and Georges Bossis. The rheology of concentrated suspensions of spheres in simple shear flow by numerical simulation. *Journal of Fluid mechanics*, 155:105–129, 1985.

[22] Xiang Cheng, Jonathan H McCoy, Jacob N Israelachvili, and Itai Cohen. Imaging the microscopic structure of shear thinning and thickening colloidal suspensions. *Science*, 333(6047):1276–1279, 2011.

[23] J Bergenholtz, JF Brady, and M Vicic. The non-newtonian rheology of dilute colloidal suspensions. *Journal of Fluid Mechanics*, 456:239–275, 2002.

[24] John R Melrose and Robin C Ball. Continuous shear thickening transitions in model concentrated colloids—the role of interparticle forces. *Journal of Rheology*, 48(5):937–960, 2004.

[25] Ehssan Nazockdast and Jeffrey F Morris. Microstructural theory and the rheology of concentrated colloidal suspensions. *Journal of Fluid Mechanics*, 713:420–452, 2012.

[26] R.L Hoffman. Discontinuous and dilatant viscosity behavior in concentrated suspensions. ii. theory and experimental tests. *Journal of Colloid and Interface Science*, 46(3):491–506, 1974.

[27] Richard L. Hoffman. Discontinuous and dilatant viscosity behavior in concentrated suspensions iii. necessary conditions for their occurrence in viscometric flows. *Advances in Colloid and Interface Science*, 17(1):161–184, 1982.

[28] Ronald G Egres and Norman J Wagner. The rheology and microstructure of acicular precipitated calcium carbonate colloidal suspensions through the shear thickening transition. *Journal of rheology*, 49(3):719–746, 2005.

[29] Brent J Maranzano and Norman J Wagner. Flow-small angle neutron scattering measurements of colloidal dispersion microstructure evolution through the shear thickening transition. *The Journal of chemical physics*, 117(22):10291–10302, 2002.

[30] Eric Brown and Heinrich M Jaeger. The role of dilation and confining stresses in shear thickening of dense suspensions. *Journal of Rheology*, 56(4):875–923, 2012.

[31] A.J. Liu and S.R. Nagel. *Jamming and Rheology: Constrained Dynamics on Microscopic and Macroscopic Scales*. CRC Press, London, 2001.

[32] Andrea J Liu and Sidney R Nagel. Jamming is not just cool any more. *Nature*, 396(6706):21–22, 1998.

[33] ME Cates, JP Wittmer, J-P Bouchaud, and Ph Claudin. Jamming, force chains, and fragile matter. *Physical review letters*, 81(9):1841, 1998.

[34] Veronique Trappe, V Prasad, Luca Cipelletti, PN Segre, and David A Weitz. Jamming phase diagram for attractive particles. *Nature*, 411(6839):772–775, 2001.

[35] Michael Dennin. Discontinuous jamming transitions in soft materials: coexistence of flowing and jammed states. *Journal of Physics: Condensed Matter*, 20(28):283103, 2008.

[36] Martin van Hecke. Jamming of soft particles: geometry, mechanics, scaling and isostaticity. *Journal of Physics: Condensed Matter*, 22(3):033101, 2009.

[37] Andrea J Liu and Sidney R Nagel. Granular and jammed materials. *Soft Matter*, 6(13):2869–2870, 2010.

[38] Andrea J Liu and Sidney R Nagel. The jamming transition and the marginally jammed solid. *Annu. Rev. Condens. Matter Phys.*, 1(1):347–369, 2010.

[39] Robert P Behringer and Bulbul Chakraborty. The physics of jamming for granular materials: a review. *Reports on Progress in Physics*, 82(1):012601, 2018.

[40] Giulio Biroli. A new kind of phase transition? *Nature Physics*, 3:222–223, 2007.

[41] Dapeng Bi, Jie Zhang, Bulbul Chakraborty, and Robert P Behringer. Jamming by shear. *Nature*, 480(7377):355–358, 2011.

[42] HA Vinutha and Srikanth Sastry. Disentangling the role of structure and friction in shear jamming. *Nature Physics*, 12(6):578–583, 2016.

[43] HA Vinutha and Srikanth Sastry. Geometric aspects of shear jamming induced by deformation of frictionless sphere packings. *Journal of Statistical Mechanics: Theory and Experiment*, 2016(9):094002, 2016.

[44] HA Vinutha and Srikanth Sastry. Force networks and jamming in shear-deformed sphere packings. *Physical Review E*, 99(1):012123, 2019.

[45] Pallabi Das, HA Vinutha, and Srikanth Sastry. Unified phase diagram of reversible–irreversible, jamming, and yielding transitions in cyclically sheared soft-sphere packings. *Proceedings of the National Academy of Sciences*, 117(19):10203–10209, 2020.

[46] Ryohei Seto, Abhinendra Singh, Bulbul Chakraborty, Morton M Denn, and Jeffrey F Morris. Shear jamming and fragility in dense suspensions. *Granular Matter*, 21:1–8, 2019.

[47] Ivo R Peters, Sayantan Majumdar, and Heinrich M Jaeger. Direct observation of dynamic shear jamming in dense suspensions. *Nature*, 532(7598):214–217, 2016.

[48] Nicole M James, Endao Han, Ricardo Arturo Lopez de la Cruz, Justin Jureller, and Heinrich M Jaeger. Interparticle hydrogen bonding can elicit shear jamming in dense suspensions. *Nature materials*, 17(11):965–970, 2018.

[49] Endao Han, Ivo R Peters, and Heinrich M Jaeger. High-speed ultrasound imaging in dense suspensions reveals impact-activated solidification due to dynamic shear jamming. *Nature communications*, 7(1):1–8, 2016.

[50] Nicole M James, Huayue Xue, Medha Goyal, and Heinrich M Jaeger. Controlling shear jamming in dense suspensions via the particle aspect ratio. *Soft matter*, 15(18):3649–3654, 2019.

[51] Abhinendra Singh, Christopher Ness, Ryohei Seto, Juan J de Pablo, and Heinrich M Jaeger. Shear thickening and jamming of dense suspensions: The "roll" of friction. *Physical Review Letters*, 124(24):248005, 2020.

[52] Rijan Maharjan and Eric Brown. Giant deviation of a relaxation time from generalized newtonian theory in discontinuous shear thickening suspensions. *Physical Review Fluids*, 2(12):123301, 2017.

[53] Saisai Cao, Qianyun He, Haoming Pang, Kaihui Chen, Wanquan Jiang, and Xinglong Gong. Stress relaxation in the transition from shear thinning to shear jamming in shear thickening fluid. *Smart Materials and Structures*, 27(8):085013, 2018.

[54] Abhinendra Singh, Sidhant Pednekar, Jaehun Chun, Morton M. Denn, and Jeffrey F. Morris. From yielding to shear jamming in a cohesive frictional suspension. *Phys. Rev. Lett.*, 122:098004, Mar 2019.

[55] Chiao-Peng Hsu, Shivaprakash N Ramakrishna, Michele Zanini, Nicholas D Spencer, and Lucio Isa. Roughness-dependent tribology effects on discontinuous shear thickening. *Proceedings of the National Academy of Sciences*, 115(20):5117–5122, 2018.

[56] Nathan C. Keim, Joseph D. Paulsen, Zorana Zeravcic, Srikanth Sastry, and Sidney R. Nagel. Memory formation in matter. *Rev. Mod. Phys.*, 91:035002, Jul 2019.

[57] Edward Y. X. Ong, Anna R. Barth, Navneet Singh, Meera Ramaswamy, Abhishek Shetty, Bulbul Chakraborty, James P. Sethna, and Itai Cohen. Jamming memory into acoustically trained dense suspensions under shear. *Phys. Rev. X*, 14:021027, May 2024.

[58] F Gadala-Maria and Andreas Acrivos. Shear-induced structure in a concentrated suspension of solid spheres. *Journal of rheology*, 24(6):799–814, 1980.

[59] Masahiro Toiya, Justin Stambaugh, and Wolfgang Losert. Transient and oscillatory granular shear flow. *Phys. Rev. Lett.*, 93:088001, Aug 2004.

[60] Kittiwit Matan, Rachel B. Williams, Thomas A. Witten, and Sidney R. Nagel. Crumpling a thin sheet. *Phys. Rev. Lett.*, 88:076101, Jan 2002.

[61] Leonard Mullins. Effect of stretching on the properties of rubber. *Rubber chemistry and technology*, 21(2):281–300, 1948.

[62] Sebanti Chattopadhyay and Sayantan Majumdar. Inter-particle adhesion induced strong mechanical memory in a dense granular suspension. *The Journal of chemical physics*, 156(24), 2022.

[63] Laurent Corte, Paul M Chaikin, Jerry P Gollub, and David J Pine. Random organization in periodically driven systems. *Nature Physics*, 4(5):420–424, 2008.

[64] Nathan C. Keim and Sidney R. Nagel. Generic transient memory formation in disordered systems with noise. *Phys. Rev. Lett.*, 107:010603, Jun 2011.

[65] Joseph D. Paulsen, Nathan C. Keim, and Sidney R. Nagel. Multiple transient memories in experiments on sheared non-brownian suspensions. *Phys. Rev. Lett.*, 113:068301, Aug 2014.

[66] John Adair Barker, DE Schreiber, BG Huth, and Douglas Hugh Everett. Magnetic hysteresis and minor loops: Models and experiments. *Proceedings of the Royal Society of London. A. Mathematical and Physical Sciences*, 386(1791):251–261, 1983.

[67] James P. Sethna, Karin Dahmen, Sivan Kartha, James A. Krumhansl, Bruce W. Roberts, and Joel D. Shore. Hysteresis and hierarchies: Dynamics of disorder-driven first-order phase transformations. *Phys. Rev. Lett.*, 70:3347–3350, May 1993.

[68] Olga Perković and James P Sethna. Improved magnetic information storage using return-point memory. *Journal of applied physics*, 81(3):1590–1597, 1997.

[69] Jie Ren, Joshua A. Dijksman, and Robert P. Behringer. Reynolds pressure and relaxation in a sheared granular system. *Phys. Rev. Lett.*, 110:018302, Jan 2013.

[70] Micah Lundberg, Kapilanjan Krishan, Ning Xu, Corey S O'Hern, and Michael Dennin. Reversible plastic events in amorphous materials. *Physical Review E—Statistical, Nonlinear, and Soft Matter Physics*, 77(4):041505, 2008.

[71] Edward YX Ong, Meera Ramaswamy, Ran Niu, Neil YC Lin, Abhishek Shetty, Roseanna N Zia, Gareth H McKinley, and Itai Cohen. Stress decomposition in laos of dense colloidal suspensions. *Journal of Rheology*, 64(2):343–351, 2020.

[72] Vikram Rathee, Daniel L Blair, and Jeffrey S Urbach. Dynamics and memory of boundary stresses in discontinuous shear thickening suspensions during oscillatory shear. *Soft Matter*, 17(5):1337–1345, 2021.

[73] Endao Han, Matthieu Wyart, Ivo R. Peters, and Heinrich M. Jaeger. Shear fronts in shear-thickening suspensions. *Phys. Rev. Fluids*, 3:073301, Jul 2018.

CHAPTER

TWO

Experimental Techniques

"An experiment is a question which science poses to Nature and a measurement is the recording of Nature's answer."

- Max Planck -

2.1 Introduction

The primary focus of this thesis is to experimentally explore various non-equilibrium properties of shear thickening and shear jammed dense suspensions, such as stress relaxation, memory formation, flow-induced plasticity, and failure, using shear rheology and optical imaging techniques. The bulk rheological properties are measured using a commercial stress-controlled rheometer. The in-situ optical imaging setup is used to probe microscopic aspects governing the bulk flow properties of the sample. Various particulate systems are used to get a generalized understanding of these phenomena. Apart from commercially available systems, we also synthesize various colloidal particles of different sizes and shapes, which helps us to expand our scope of research. The characterization of the systems is mostly done using the Scanning Electron Microscopy (SEM), and Cryo-SEM techniques.

This chapter provides the relevant details of these experimental techniques, synthesis protocol, and sample preparation methods.

2.2 Experimental Techniques

2.2.1 Rheological measurements

One of the most commonly used instrument for studying the bulk flow and deformation behavior of materials is a rotational rheometer [1, 2]. Based on operational principles there are two broad classes of rotational rheometers: **strain-controlled rheometers** and **stress-controlled rheometers**.

- In a strain-controlled rheometer, the motor applies a controlled displacement or speed (related to the strain or strain rate) to the sample. The resulting torque (related to stress) is measured using an additional torque transducer. In this configuration, electrical current is used to generate the motor's displacement or speed. It is particularly well-suited for high-frequency applications [2].

- In stress-controlled rheometers, a specific electrical current is applied to the motor assembly, generating a magnetic field that produces an electrical torque, causing the drive shaft to rotate. Thus, the torque signal is directly inferred from the motor current, eliminating the need for a separate torque transducer. The movement of the motor shaft is precisely monitored using an optical encoder. Stress-controlled

rheometers typically offer superior torque sensitivity but are generally less effective in high-frequency measurements due to the impact of inertial effects of the motor [2].

In recent times, using high-speed feedback circuits the stress-controlled rheometer can also perform reliable strain-controlled measurements and vice versa. The use of an advanced electronic circuit for the feedback loop can precisely control the shear stress as well as the shear rate, irrespective of the primary controlling parameter of the instrument.

2.2.2 The MCR 702 Rheometer

In all our experiments, we use a commercial stress-controlled rheometer MCR 702 from Anton Paar (Austria) (Figure 2.1). This is a rheometer based on twin-drive technology where two air bearings supported electrically commuted (EC) motors can work together[3]. Like many other rheometers, using the EC motor the electromagnetic torque can be adjusted linearly with the stator current, allowing for instantaneous changes in torque when the current changes. This setup enables quick and precise control of strain or shear rate without overshoots. With a high-resolution optical encoder, accurate strain and strain rate control is possible. Unlike a traditional controlled strain (CR) rheometer, a separate torque transducer is not required; instead, the electrical current of the motor serves as the measure of torque. Similar to a controlled stress (CS) rheometer, both the input and measurement of the relevant properties are conducted from the same side of the rheometer.

The use of two rheometer motors allows the instrument to operate with high flexibility and in various operating modes like (i) Counter Rotation mode (ii) Separate Motor Transducer (SMT) mode, (iii) Combined Motor Transducer (CMT) mode.

- Counter Rotation mode is a special mode of operation possible in the twin drive rheometer. Here both the motors are used as the drive units and torque transducers. Here the motors are configured to rotate opposite to each other (left panel of Figure 2.2). The rheological parameters are determined from the difference in speed between the two individual motors and the measured torque on the upper drive. This counter-rotation mode is particularly helpful for in-situ imaging at a high shear rate as the total speed is distributed between the two motors. This mode enables the formation of a stagnation plane in the sample during shear measurement and makes it easier to examine microscopically. Ideally, one can adjust the position

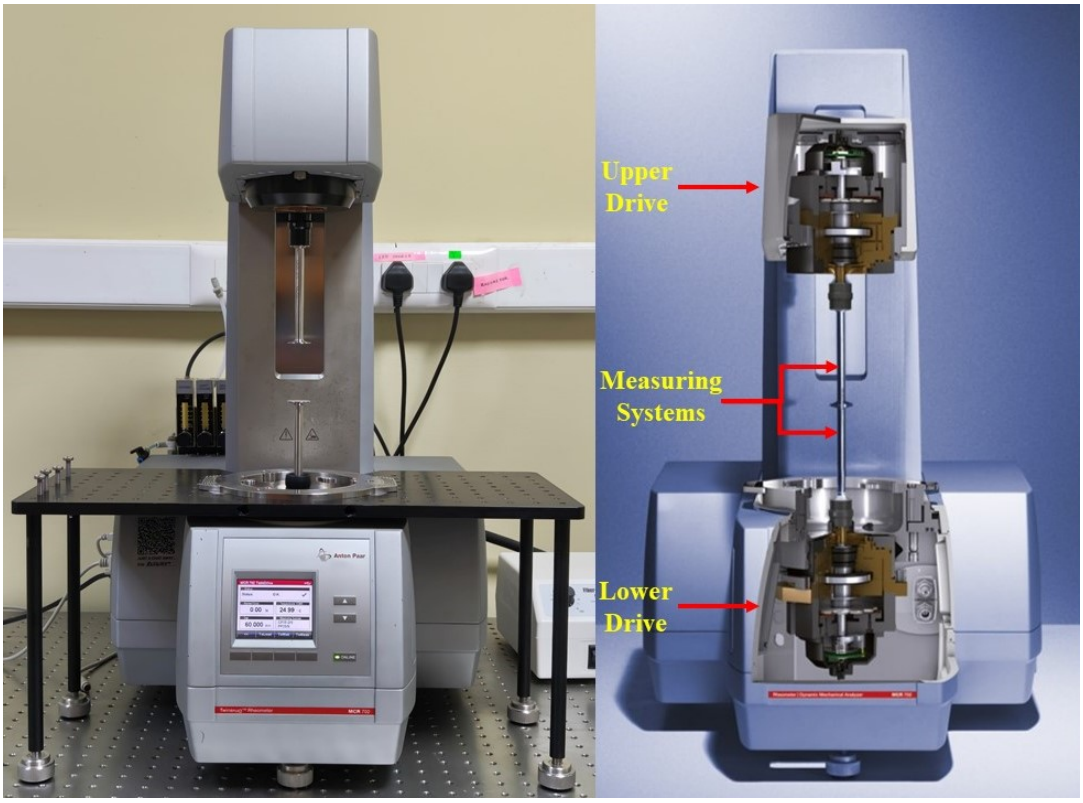

Figure 2.1: Image of Twin drive MCR 702 rheometer used for this thesis work (left) and the corresponding schematics showing the simultaneous arrangement of two fully functional rheometer drives in a single instrument (right) (figure adapted from [3]).

of the stagnation plane by adjusting the speed of the individual motor while keeping the differential speed between the two motors constant.

- In the Separate Motor Transducer (SMT) mode, both motors are utilized in a synchronized manner. One motor remains fixed and serves particularly as a torque transducer, while the other motor acts as a drive unit (middle panel of Figure 2.2). Both the driving unit and torque transducer are in constant communication as they are operated by the same controller electronics. In this configuration, the MCR 702 rheometer can perform rotational and oscillatory tests under SMT mode.

- In Combined Motor Transducer (CMT) mode only the upper motor is used both as a driving unit and torque transducer unit. Here the lower motor is removed and the upper motor simultaneously measures and controls the necessary parameters (right panel of Figure 2.2).

A Peltier unit at the bottom plate is used to control the sample temperature dur-

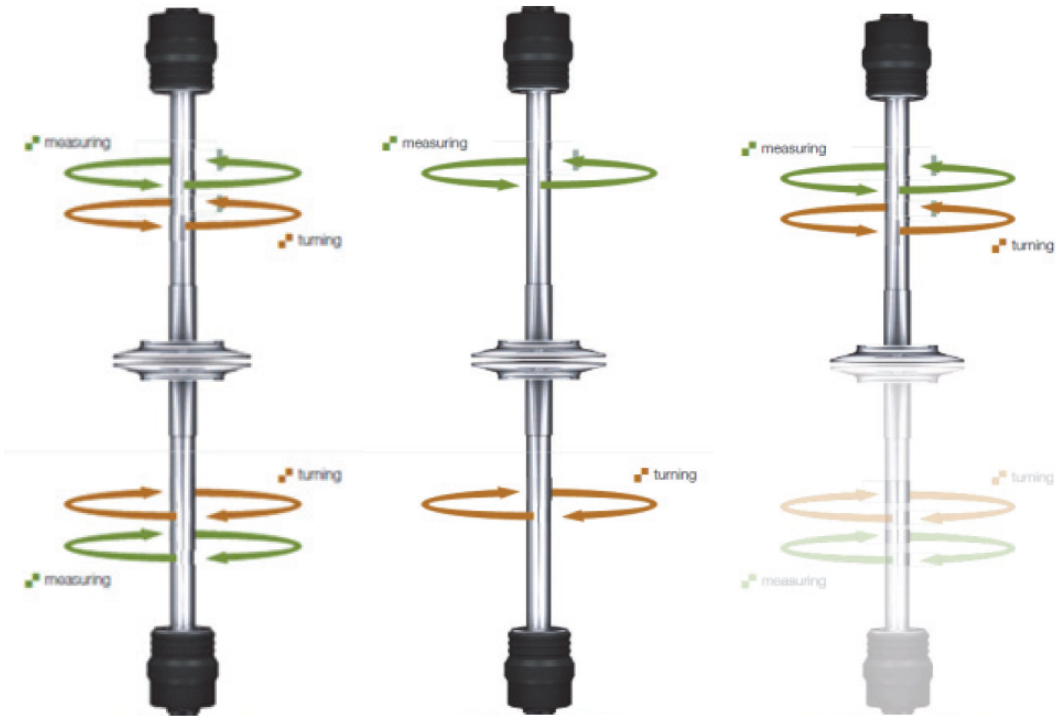

Figure 2.2: Schematics of different possible modes of operation in the twin drive MCR 702 rheometer. Counter rotation mode (left), Separate motor transducer (SMT) mode (middle), and Combined motor transducer (CMT) mode (right) (figure adapted from [3]).

ing the rheological measurements in the single-drive CMT mode. In this thesis, all the temperature-controlled experiments and basic flow curve measurements are done using the single-drive CMT mode, and we use the twin-drive counter-rotation mode for other rheological measurements with in-situ imaging.

Depending on the particle size, we use both parallel plate (PP) and cone-plate (CP) geometries for our measurements (Figure 2.3). In all our cases, the diameter of the cone or the plate is 25 mm, and the surfaces of the geometries are sandblasted to minimize slippage. The CP geometry is helpful in maintaining a constant applied shear rate throughout the sample. Here, the distance between the cone truncation and the plate is fixed, and it should be sufficiently greater than the typical size of the particles. The PP geometry allows the variation of the gap between the plates, which is particularly helpful for the bigger-sized particles.

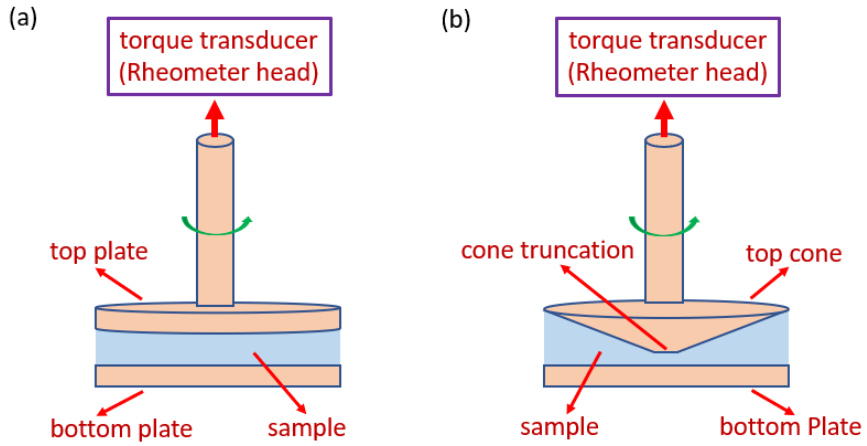

Figure 2.3: Schematics of (a) parallel plate and (b) cone-plate geometry used for rheological measurements.

2.2.3 In-situ optical boundary imaging

We set up in-situ imaging to probe the flow gradient plane during the rheological measurements (Figure 2.4). The imaging setup comprises a camera, a long working distance objective, and an LED light source. Depending on the requirement, we use two different cameras: (1) Lumenera Lt545R and (2) Phantom Miro C210. Lumenera Lt545R camera has a better resolution, which is helpful for studying the micron-sized particle level dynamics, but the frame rate of the camera is around 40 fps at a full resolution of 2464 x 2056. For a higher frame rate, we use the Phantom Miro C210 camera, which is a high-speed monochrome CMOS camera with a maximum frame rate of 1800 fps at a maximum resolution of 1280 x 1024. The suitable camera is coupled with a long working distance objective (Mitutoyo) of appropriate magnification. We use objectives of three different magnifications: 5X, 10X, and 20X. The sample boundary image (Figure 2.4) is taken under reflection mode, where the sample boundary is illuminated using an LED light source (Dolan-Jenner Industries) and image the diffused scattering in the flow gradient plane. In the case of a transparent sample, the system is seeded with a very small amount of polystyrene tracer particles to obtain a clear speckle pattern.

2.2.4 Scanning Electron Microscope

In a scanning electron microscope (SEM), a high energy electron beam is used to study the different surface morphology of the system at the sub-micron and nano-scale level where the sample features can not be resolved in the optical microscope [4, 5].

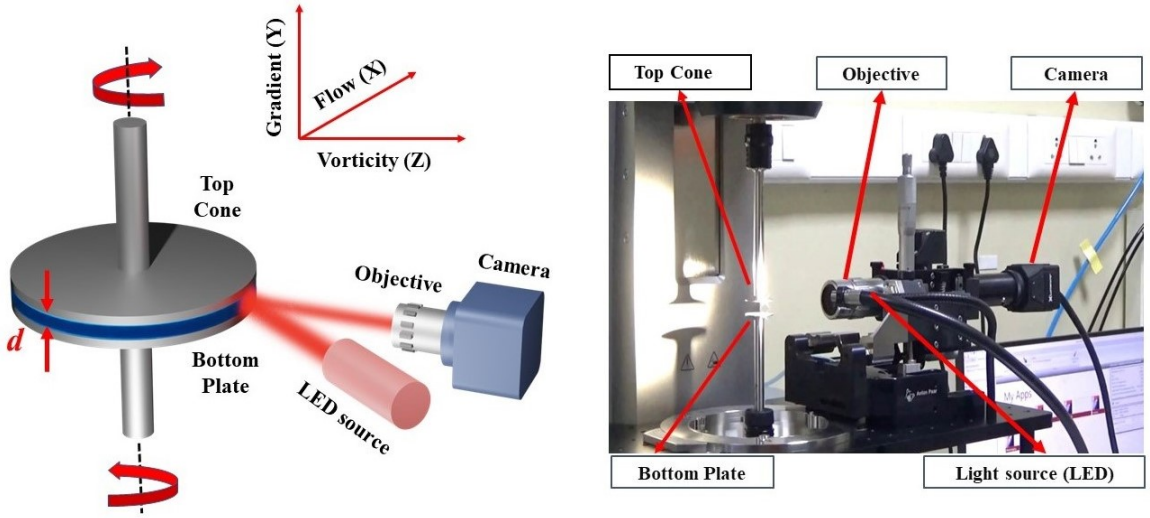

Figure 2.4: Schematic of sample boundary imaging setup. Alongside the actual imaging setup used for in-situ sample boundary imaging.

In general, a beam of electrons is produced by a thermionic or field emission-type electron gun. The interaction of this electron beam and the atoms of the sample can generate various types of signals, including secondary electrons, backscattered electrons, characteristic X-rays, etc. Out of all these signals, secondary electrons have very low energies, and they are produced from a few nanometers on the top at the surface. These highly localized secondary electrons are collected by the secondary electron detector and, depending on the signal intensity or the number of secondary electrons detected can be converted into the image. The electron beam is focused by condenser lenses, and using the scanning coils, the electron beam is deflected to scan the sample surface (Figure 2.5).

In our case, a Carl-Zeiss Field Emission Scanning Electron Microscope (FESEM) is used to characterize the particle size distribution and surface morphology of polystyrene microspheres, silica microspheres, fumed silica particles, and cornstarch particles (Figure 2.5). To prepare the sample for the SEM imaging, we first prepare a dilute suspension by dispersing the particles in water or water-ethanol mixture. Then we put a drop of this suspension on an ITO-coated glass plate and left it overnight to dry. For polystyrene microspheres and cornstarch particles, as the sample is non-conducting, a thin layer of platinum coating is added using the Sputter Coater (Quorum Q150R S) (Figure 2.6 (a)). Then the ITO glass plate is now kept over the sample holder (Figure 2.6 (b)) and then loaded into the instrument for imaging.

In order to image the sample in the presence of solvent, the Cryogenic SEM (Cryo-SEM) technique is used [6]. In this technique, the sample structure is frozen by plunging

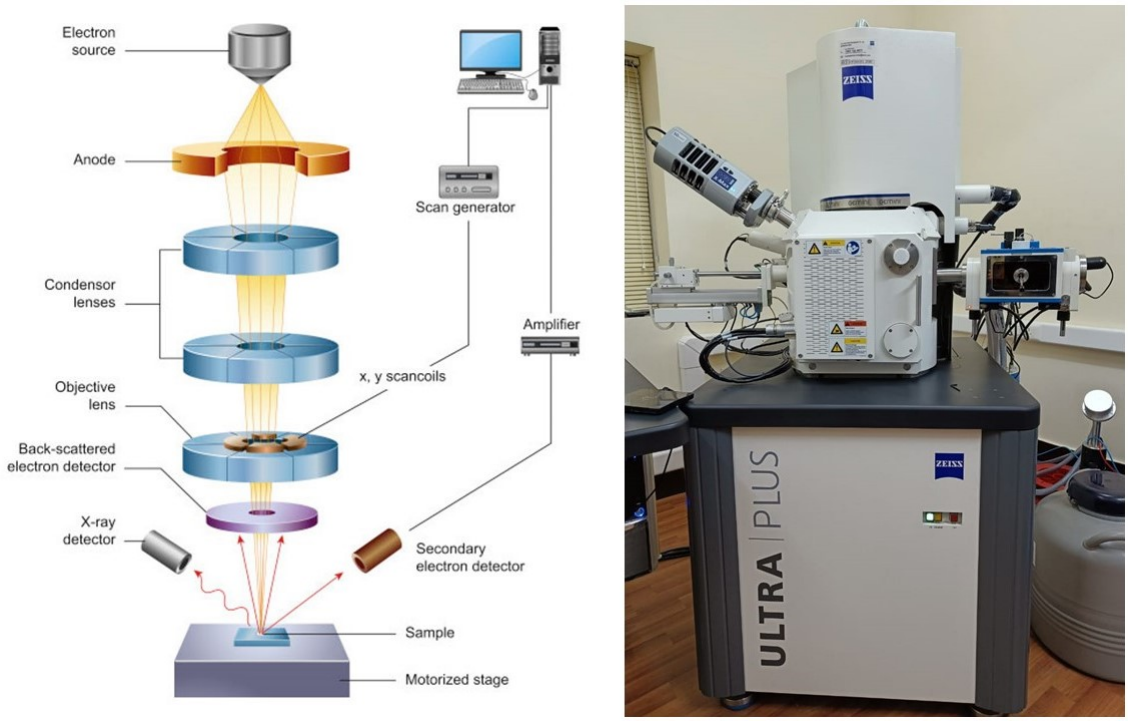

Figure 2.5: Schematic of Field Emission Scanning Electron Microscope (FESEM) (adapted from ref.[5]). Alongside the actual Carl-Zeiss FESEM used in this thesis work is shown.

it into the liquid nitrogen. This will help to retain the structure inside the solvent before imaging.

2.3 Particle Synthesis

2.3.1 Polystyrene microsphere

We synthesize polystyrene micro-spheres of different sizes using the dispersion polymerization technique [7, 8, 9].

In this synthesis procedure, we use styrene as the monomer, Polyvinylpyrrolidone (PVP K-30) as the stabilizer, AIBN as the initiator, and ethanol or water-ethanol mixture as the dispersion medium. The required amount of PVP and ethanol or ethanol-water mixture are added to the three-necked 250 ml round bottom flask. This flask is dipped/fitted into a silicon oil bath over a magnetic stirrer to make the temperature uniform at $70°C$ and mixed properly under stirring. The required amount of styrene and AIBN are mixed separately in a beaker using a glass rod. This solution of styrene and

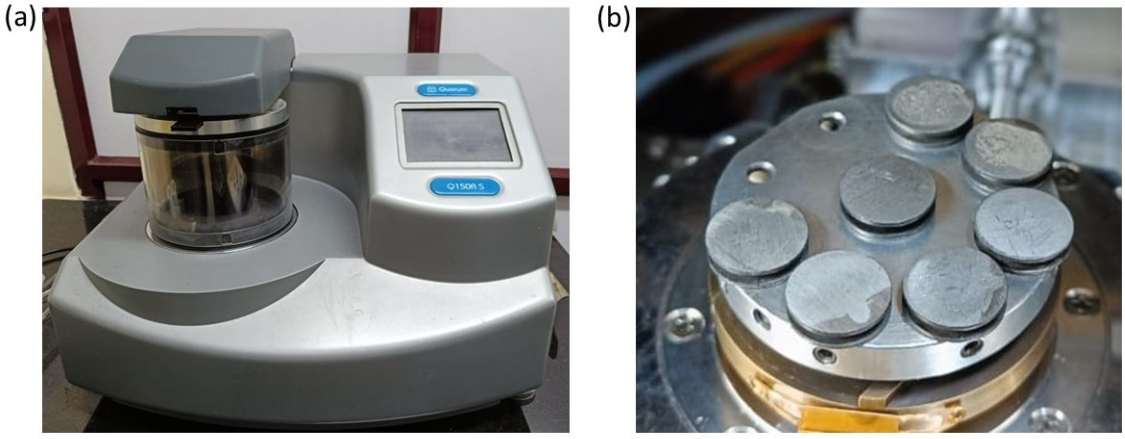

Figure 2.6: (a) Quorum Q150R S Sputter Coater unit (b) Sample holder for SEM imaging.

AIBN is added to the reaction solution in the round bottom flask when the temperature is stabilized at $65°C - 70°C$ depending on the requirement. The complete reaction is carried out for 24 hours in a nitrogen atmosphere supplied using nitrogen balloons (Figure 2.7).

We synthesized polystyrene particles of different sizes (Figure 2.8(a), (b), and (c)). The controlling parameters and reactant amounts are summarized in Table 2.1. The effect of controlling parameters over particle size is summarized in Table 2.2.

2.3.2 Silica microsphere

Using the Stober process we synthesized spherical silica particles of average size $\approx 800nm$ (Figure 2.8(d)) [10].

Materials: ammonia (25% aqueous solution), Milli-Q water, isopropanol and tetra-ethyl-ortho-silicate (TEOS).

In a 100ml volumetric flask, we take $10.2ml$ of Milli-Q water, then $3.8ml$ of ammonia solution(25%) was added to the same flask. Now isopropanol was added to the flask till the graduation mark. This mixture was shaken properly and then transferred into a double-necked round bottom flask. Using the magnetic stirrer the solution was mixed for 10 minutes at 300 rpm. Using a syringe $20.08ml$ of TEOS was measured out and drop wise added to the round bottom flask. The complete reaction was carried out for 5 hours at $18°C$. After 5 hours the mixture was centrifuged two times with ethanol and water each. Then two times with a mixture of water and ethanol. The collected particles were dried using a vacuum oven.

Size of the particle	**AIBN**	**PVP**	**Styrene**	**Ethanol**	**Water**	**Temperature**	**R.P.M**
$\sim 7 \pm 3\mu m$	0.2745 gm or 0.2495 ml(1 wt% styrene)	1.920 gm or 1.536 ml (6.6 wt% styrene)	27.18gm Or 30 ml	54 ml	0 ml	$70°C$	300
$\sim 2.8\mu m$	0.30 gm (2 wt% w.r.t. Styrene)	1.44 gm (8.922 wt% w.r.t. Styrene)	14.7gm Or 16.225 ml	78.56 gm Or 99.56 ml	0 ml	$70°C$	300
$\sim 700nm$	0.114 gm (1.4 wt% w.r.t. Styrene)	2.00 gm (20 wt% w.r.t. Styrene)	8.00gm Or 8.83 ml	80 ml	20 ml	$65°C$	200

Table 2.1: Controlling parameters and reactant amounts for the synthesis of polystyrene particles.

Parameters name	**Changes in parameter**	**Effect on particle size**
Styrene	decrease	decrease
PVP	increase	decrease
AIBN	decrease	decrease
Time	decrease	decrease
Water to ethanol ratio	increase	decrease
Temperature	decrease	decrease

Table 2.2: The effect of controlling parameters over particle size

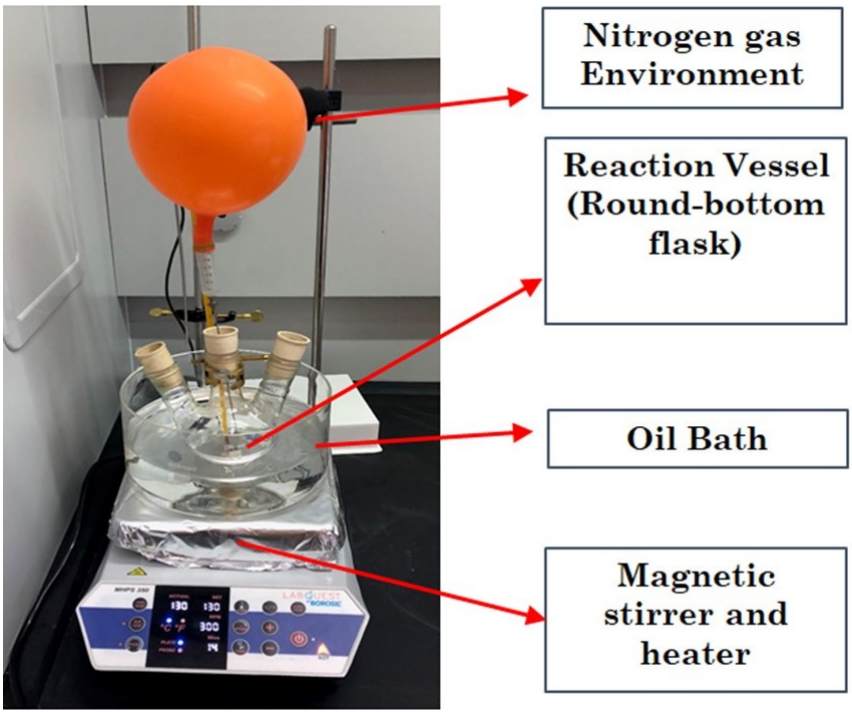

Figure 2.7: Setup for polystyrene microsphere synthesis

I also synthesized rod-like silica particles using one pot method [11].

2.4 Sample preparation

In this thesis, we use different types of dense particulate suspensions that show shear thickening or shear jamming properties. We use dense suspensions of polystyrene (PS) particles of different sizes dispersed in polyethylene glycol(PEG) 400 or PEG 200, corn-starch particles dispersed in glycerol or water, silica particles dispersed in glycerol, and different hydrophilic fumed silica particles dispersed in glycerol.

The samples of different volume fractions (ϕ) are prepared by gradually adding the required amount of dry particles into the solvent and thoroughly mixing at each step using a spatula. The CS suspensions are then immediately used for rheological measurements. In the case of PS particles, the suspensions are desiccated overnight to remove air bubbles trapped inside. To ensure uniform dispersion, the samples are ultrasonicated for 5 minutes (at room temperature) just before loading for rheological measurements.

In the case of fumed silica system, hydrophilic Aerosil fumed silica (FS) of six different grades (OX50, A90, A150, A200, A300, A380) from Evonik Industries are used for the

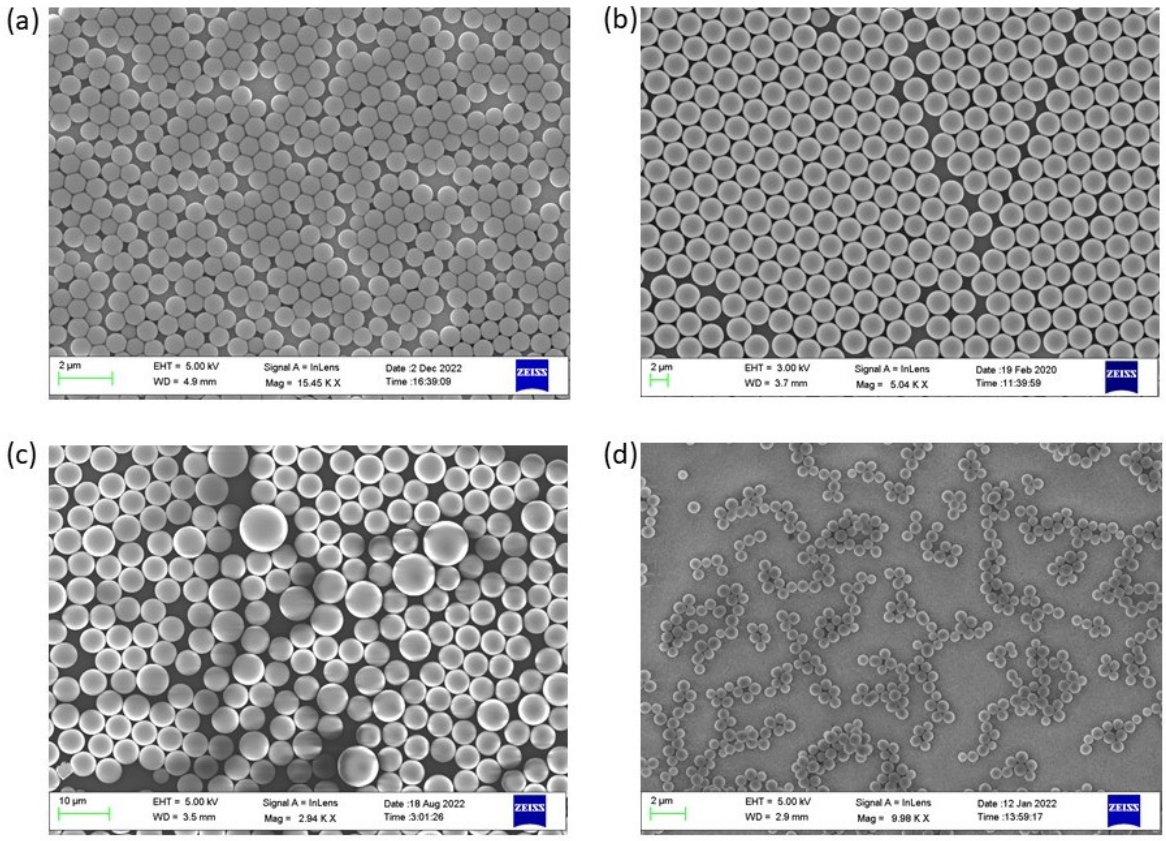

Figure 2.8: SEM image of polystyrene particles of size (a) $700 \pm 50nm$, (b) $2.8 \pm 0.08\mu m$ and (c) $\approx 7 \pm 3\mu m$. (d) SEM image of nano-silica particles ($\approx 800nm$).

preparation of dense particulate suspensions with glycerol as the solvent. The suspensions are prepared by gradually adding the required amount of fumed silica particles into the solvent and dispersing at each step thoroughly using a spatula. After dispersing the powder completely, the air-sealed sample is kept in the oven at 60° to remove air bubbles. For higher volume fraction samples, as complete mixing of dry powder is difficult, we prepared the sample in two steps. First, we prepare a lower volume fraction sample and remove the air bubbles completely. Then we add the additional amount of FS powder to get desired ϕ. Again this sample is kept in the oven to remove bubbles before the transparent sample is used for rheological measurements.

Bibliography

[1] T.G. Mezger. *The Rheology Handbook: For Users of Rotational and Oscillatory Rheometers*. Coatings compendia. Vincentz Network, 2006.

[2] C.W. Macosko. *Rheology: Principles, Measurements, and Applications*. Advances in interfacial engineering series. VCH, 1994.

[3] Jörg Läuger. A new rheometer platform for extended testing capabilities. *Annual transactions of the Nordic rheology society*, 21:1–5, 2013.

[4] R Senthil Prabhu, R Priyanka, M Vijay, and GR Kaviya Vikashini. Field emission scanning electron microscopy (fesem) with a very big future in pharmaceutical research. *Research Article—Pharmaceutical Sciences—OA Journal—MCI Approved—Index Copernicus*, 11:2321–3272, 2021.

[5] https://www.nanoscience.com/techniques/scanning-electron-microscopy/.

[6] Hans M Wyss, Markus Hütter, Martin Müller, Lorenz P Meier, and Ludwig J Gauckler. Quantification of microstructures in stable and gelated suspensions from cryosem. *Journal of colloid and interface science*, 248(2):340–346, 2002.

[7] Dong Wang, Bing Yu, Hai-Lin Cong, Yue-Zhong Wang, Qian Wu, and Ji-Lei Wang. Synthesis of monodisperse polystyrene microspheres by seeding polymerization. *Integrated Ferroelectrics*, 147(1):41–46, 2013.

[8] Anthony James Paine, Wayne Luymes, and James McNulty. Dispersion polymerization of styrene in polar solvents. 6. influence of reaction parameters on particle size and molecular weight in poly (n-vinylpyrrolidone)-stabilized reactions. *Macromolecules*, 23(12):3104–3109, 1990.

[9] A Tuncel, M Tuncel, and B Salih. Electron microscopic observation of uniform macroporous particles. i. effect of seed latex type and diluent. *Journal of applied polymer science*, 71(14):2271–2290, 1999.

[10] Xiao-Dong Wang, Zheng-Xiang Shen, Tian Sang, Xin-Bin Cheng, Ming-Fang Li, Ling-Yan Chen, and Zhan-Shan Wang. Preparation of spherical silica particles by stöber process with high concentration of tetra-ethyl-orthosilicate. *Journal of colloid and interface science*, 341(1):23–29, 2010.

[11] Anke Kuijk, Alfons Van Blaaderen, and Arnout Imhof. Synthesis of monodisperse, rodlike silica colloids with tunable aspect ratio. *Journal of the American Chemical Society*, 133(8):2346–2349, 2011.

CHAPTER

THREE

Origin of two distinct stress relaxation regimes in shear jammed dense suspensions

"Look deep into nature, and then you will understand everything better."

- Albert Einstein -

The results covered in this chapter are published in the article, Phys. Rev. Lett., 128:258002, Jun 2022 [1].

3.1 Introduction

Stress induced enhancement of viscosity in dense particulate suspensions, commonly known as shear-thickening [2, 3, 4, 5], has attracted significant recent interests both from the fundamental points of view and materials design [6, 7, 8, 9, 10, 11, 12]. For high enough particle volume fraction and applied stress, many of these systems show a remarkable transition to a shear jammed (SJ) state showing stress-activated solid-like yield stress [13, 14, 15]. Although, the phenomenon of shear-thickening is well-known since past few decades, the difference between SJ state and strong/discontinuous shear-thickened (DST) state has been demonstrated only recently and remains a topic of intense research [13, 16, 17, 18, 19]. SJ results from the stress induced constraints on sliding and rolling degrees of freedom of particles [17, 16, 20]. Such constraints can originate from frictional, hydrodynamic and other short-range inter-particle interactions [18, 16, 21]. For steady state flow of frictional systems, Wyart-Cates (W-C) Model provides microscopic insight into the stress (σ) induced increase in viscosity in terms of a single order parameter $f = f(\sigma)$: the fraction of frictional contacts in the system [7]. A recent continuum model [22] that treats the parameter 'f' as a spatially varying field with specific time-evolution can quantitatively describe a range of striking flow behaviors in these systems. Once the applied perturbation is removed, SJ state quickly relaxes back to the unperturbed fluid-like state. Such fast reversibility coupled with high stress bearing ability of SJ systems [5], remain at the heart of many potential applications.

The nature of relaxation in dense suspensions close to jamming is complex and is sparsely explored in the context of systems showing DST and SJ: Above a critical deformation rate, dense suspensions of PMMA nano-paricles show two distinct relaxation processes [23], in dense cornstarch suspensions the relaxation behavior deviates significantly from a generalized Newtonian model [24] and many aspects of the relaxation can be captured by a continuum theoretical model [25, 22]. In dense PSt-EA nano-particle suspensions, a multi-element viscoelastic model consistent with the expected force chain structure fits the relaxation behavior well [26]. Two-step relaxation have also been observed in glassy and static-jammed materials [27, 28]. However, extremely slow nature of relaxation and the existence of residual stresses in these systems highlight the widely different underlying microscopic dynamics as compared to the dense suspensions showing

DST and SJ.

Despite these detailed studies, the role of microscopic particle scale dynamics in controlling the bulk relaxation of SJ state is not understood. Importantly, due to its solid-like nature, a sustained steady state flow is not possible in SJ systems [19]. Thus, in earlier studies the mechanical state of the SJ sample just prior to relaxation remains poorly characterized. Recent experiments suggest that the mechanical properties of SJ states can be probed reliably under transient perturbations [29, 13, 14, 18]. Numerical simulations probing transient relaxation in over-damped, athermal dense suspensions of frictionless spheres found a power-law cut-off by an exponential relaxation close to the isotropic jamming point (ϕ_0) with the relaxation time diverging at $\phi = \phi_0$ [30, 31]. Although, the relevance of such findings for SJ systems remains unclear due to the difference in stress dependence of the constraints in frictionless and frictional systems [17].

In this chapter, We address these issues by studying the transient stress relaxation behavior of SJ states in dense suspensions of colloidal polystyrene particles (PS) dispersed in polyethylene glycol (PEG) using shear rheology in conjugation with high resolution boundary imaging. We observe a power-law cut-off by a stretched-exponential relaxation for moderate stress values, however, a sharp discontinuous relaxation after the power-law regime is observed for large stresses. We directly correlate plasticity and dilation in the system with the time scales associated with the bulk relaxation dynamics. We also uncover an interesting connection between the transient relaxation phenomena and the steady state SJ (SSSJ) phase diagram obtained using the W-C model.

3.2 Materials and methods

The shear thickening dense suspension is prepared by dispersing mono-disperse polystyrene (PS) particles (diameter: $2.65 \pm 0.13\ \mu m$) in a Newtonian solvent polyethylene glycol (PEG) over a wide range of volume fractions $40\% \leq \phi \leq 61\%$ as described in chapter 2. We use both PEG 400 and PEG 200 to vary the viscosity of the solvent. The viscosity can also be varied significantly by changing the temperature. We observe that above $\phi = 61\%$ the particles are difficult to disperse in the solvent due to almost solid-like nature of the suspension.

The polystyrene micro-spheres are synthesized using dispersion polymerization in ethanol with styrene (TCI, Japan) as monomer, polyvinylpyrrolidone (PVP K-30, Spectrochem, India) as stabiliser and AIBN (Spectrochem, India) as initiator [32] as described in detail in chapter 2.

All the rheological measurements are carried out on a stress control rheometer (MCR-702, Anton Paar, Austria) with 12.5 mm radius cone and plate geometry. The steady state measurements are performed in single drive and the transient measurements are done in twin drive under 50-50 counter movement mode. In order to remove the loading history and ensure that the sample condition remains unaltered after the experiment, we conduct large amplitude oscillatory shear (LAOS) measurement at a frequency 1 Hz, before and after the stress relaxation experiment. For LAOS measurement we first increase the strain amplitude (γ) logarithmically from a lower to a maximum value and then we perform a reverse run where the amplitude is again gradually decreased to the initial value. We observe the variation of storage (G') and loss (G'') moduli. We observe that the value of G' and G'' as a function of γ do not change significantly before and after the stress relaxation experiment. This also gives an idea of shear strain amplitude required to observe shear thickening in the sample. For stress relaxation experiment under a transient perturbation, the sample is subjected to a step shear strain of a certain magnitude for 25 s. We record the resulting stress response of the sample over the same period of time. We increase the amplitude of the applied shear strain systematically, from lower to higher value, to drive the system into higher peak-stress levels gradually.

Since the particles are optically opaque, the in-situ imaging of the sample boundary is possible only under reflection mode. We use a Lumenera Lt545R camera with a 5X and 20X long working distance objective (Mitutoyo). During rheological measurements, the sample boundary is illuminated using a LED light source (Dolan-Jenner Industries) and we image the diffused scattering in the flow gradient plane [33] with frame rates varying between 60 Hz - 70 Hz.

3.3 Results and discussion

As a transient perturbation, a step shear strain of a certain magnitude (γ) is applied to the sample for 25 s. We record the resulting stress response. Due to instrumental limitation, the applied strain reaches the set value after a time $t_0 \approx 0.06$ s as shown in Figure 3.1(a). Shear stress in the system quickly reaches a maximum (σ_p) and then starts to relax. We find that the nature of stress relaxation is determined by the magnitude of σ_p that depends on both ϕ and γ. We observe that for $57\% \leq \phi \leq 61\%$ (ϕ range corresponds to Steady State Shear Jamming (SSSJ), see Figure 3.2 and appendix-2), the stress relaxation is given by $\sigma(t) \sim t^{-\alpha}\, e^{-(t/\tau)^{\beta}}$ for values of σ_p up to $\sim$ 16 kPa.

Remarkably, for $\sigma_p > 16$ kPa, we find a discontinuous stress drop soon after the power-

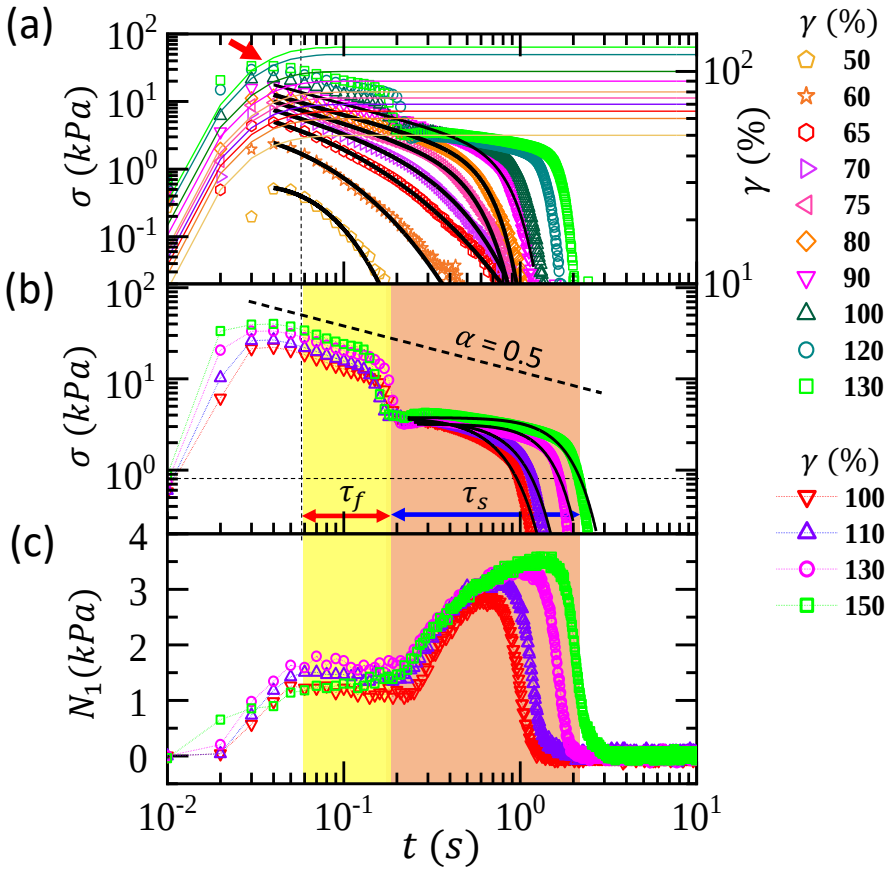

Figure 3.1: (a) Shear stress σ as a function of time t (symbols) under different applied step strains γ (thin lines). Solid lines are the fits to the power-law cut-off by a stretched exponential function (main text). The arrow indicates peak stress (σ_p) for $\gamma = 130\%$. (b) Plots of σ vs t for $\gamma \geq 100\%$ showing a self similarity. Power-law decay with slope 0.5 is also indicated. Solid-lines show typical stretched exponential fits after the discontinuous stress drop. The fast τ_f (yellow shade) and slow τ_s (brown shade) relaxation time scales are marked. (c) Evolution of first normal stress difference N_1 corresponding to the data shown in panel (b). In all cases $\phi = 58\%$ and solvent viscosity $\eta_l = 80$ $mPa.s$.

law decay regime by almost an order of magnitude (Figure 3.1(a) and 3.1(b)). After this, the stretched exponential function still captures the long-time relaxation fairly well. Similar trends are also observed for other ϕ values in SSSJ regime but, the magnitude of the discontinuous stress drop increases for larger ϕ values (Figure 3.3(a) and 3.3(b)).

In all cases, the magnitude of power law exponent (α) decreases with increasing σ_p and finally saturates at $\alpha \approx 0.5$ except for $\phi = 57\%$, where we get a higher saturation value (Figure 3.4(a)). Just below SJ ($\phi < 57\%$), the power-law regime disappears and a stretched exponential relaxation is observed for a wide range of σ_p (Figure 3.4(b)).

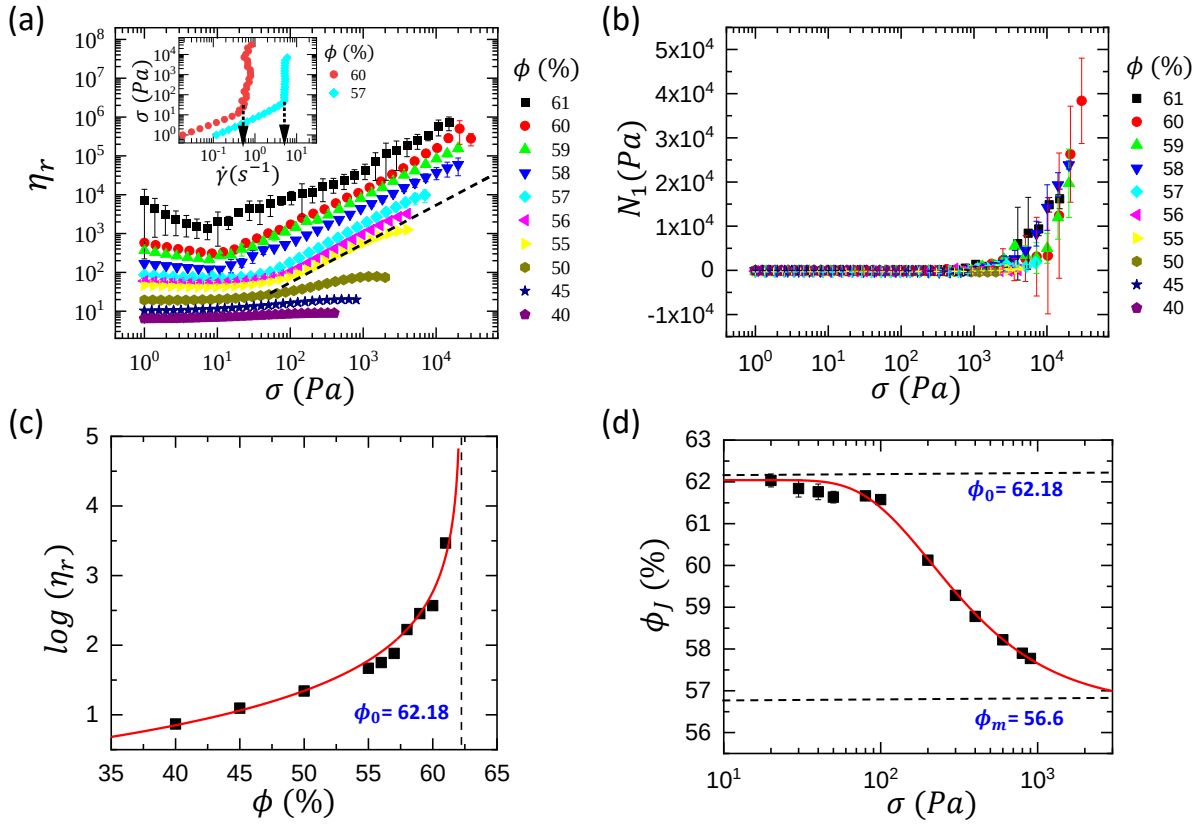

Figure 3.2: Results from the steady state measurements. (a) Variation of relative viscosity η_r with shear stress σ for volume fraction $40\% \leq \phi \leq 61\%$ as shown in the legend. The black dashed line represents a slope of 1. Error bars represent the standard deviation over three independent measurements. Inset shows shear stress σ as a function of shear rate $\dot{\gamma}$ for volume fraction 60% and 57% as shown in the legend. The dotted arrows indicate the critical shear rate $\dot{\gamma}_c$ for the corresponding volume fractions. (b) Variation of the first normal stress difference N_1 with shear stress σ during the steady state measurements shown in (a). (c) Variation of $log(\eta_r)$ with ϕ (symbols) for $\sigma = 20\ Pa$ as obtained from (a). The red solid line in (c) indicates the fit to the Krieger Dougherty (KD) relation (Eq. 3.1) with $\beta = 1.9$. Vertical dashed line corresponds to jamming volume fraction without frictional contact $\phi_0 = 62.18\%$ determined from the KD equation fitting. (d) Variation of jamming volume fraction ϕ_J with σ (symbols). The red solid line indicates the fit to the Wyart-Cates (WC) model (Eq. 3.2). Top and bottom horizontal dashed lines indicate the $\phi_0 = 62.18\%$ and $\phi_m = 56.6\%$, obtained from the WC model fitting. The WC model fitting to the flow curve is shown later in Chapter 6.

Interestingly, we observe similar relaxation dynamics for a variety of dense suspensions showing SJ (Figure 3.4(c)) indicating an universal behavior. For quantification, we define two time-scales for such discontinuous stress relaxation: a fast time scale τ_f (after t_0) at

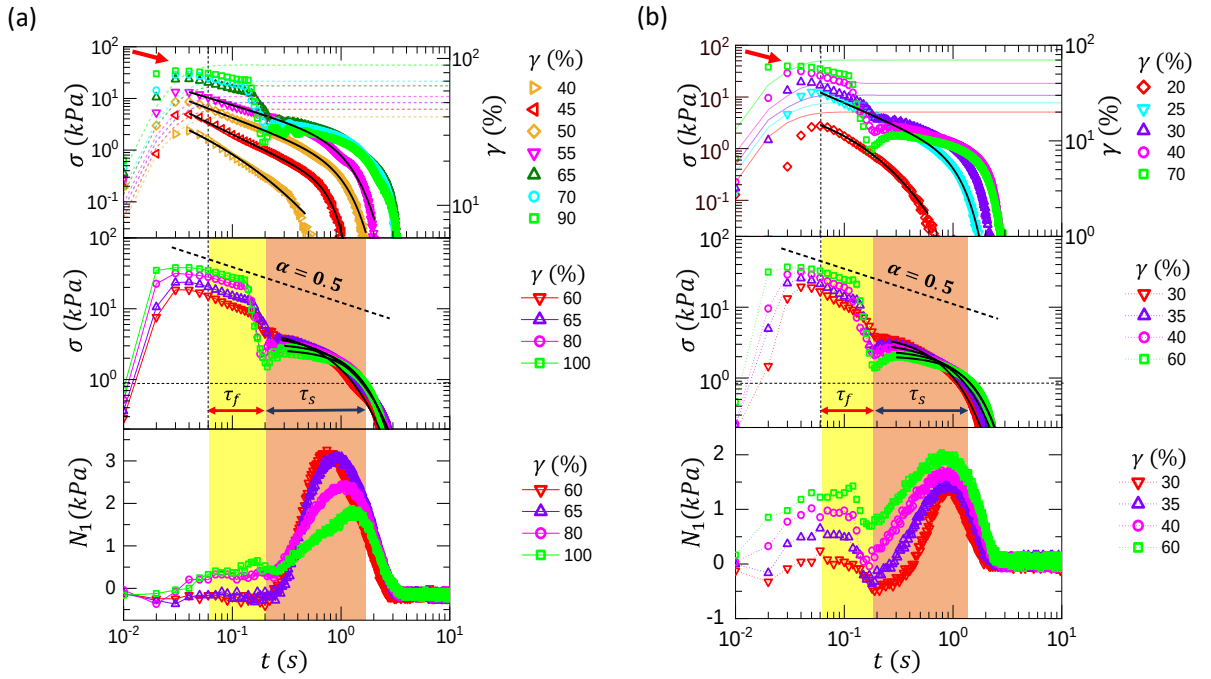

Figure 3.3: Variation of shear stress σ and first normal stress difference N_1 (similar to that shown in Figure 3.1) for volume fraction $\phi = 59\%$ (panel (a)) and $\phi = 60\%$ (panel (b)).

which the discontinuous stress drop takes place and a slower one τ_s indicating the time (after τ_f) for the stress to drop to $\sigma_d = 0.05\,\Gamma/a$ [34] (Γ: surface tension of solvent-air interface, a: particle diameter). Notably, most of the stress in the system relaxes within $t = \tau_f$. In Figure 3.1(c) we show the variation of first normal stress difference $N_1 = \frac{2\,F_N}{\pi\,r^2}$ (for cone-plate geometry where, F_N is the normal force on the plate/cone) corresponding to the stress relaxation data shown in Figure 3.1(b). In all cases we find that N_1 shows a clear positive peak at a longer time near $\sigma = \sigma_d$, with the instantaneous shear stress $\sigma(t) \approx N_1$ near the peak. On the other hand, the behavior of N_1 remains arbitrary (Figure 3.1(c) and also Figure 3.3(a) and 3.3(b)) for $t < \tau_f$ and $\sigma(t) >> N_1$ in this regime. Such interesting decoupling of the shear and the normal stress response is not observed for SSSJ (Figure 3.2(b)) [35]. For smaller σ_p values (smooth relaxation regime) we find that the magnitude of the peak in N_1 monotonically decreases with decreasing σ_p. Also, the peak gradually shifts towards the smaller time scales and completely disappears for sufficiently small values of σ_p (Figure 3.5).

To correlate the complex relaxation process with the particle scale dynamics, we use high-resolution in-situ optical imaging of the sample boundary in the flow-gradient plane

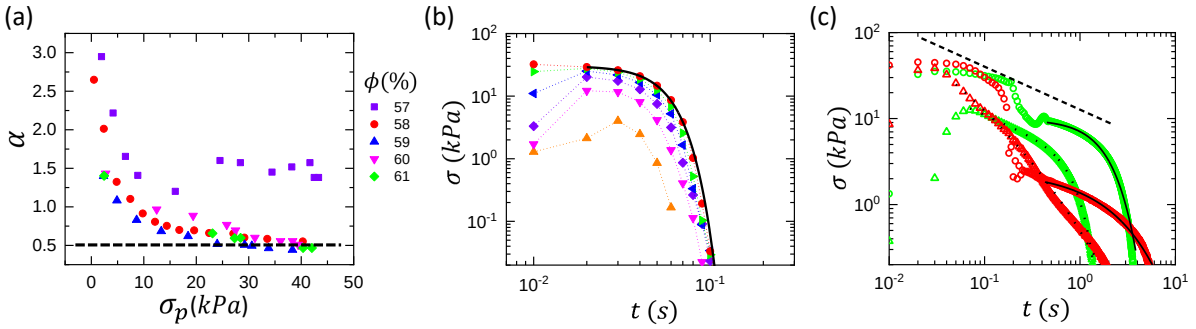

Figure 3.4: (a) Variation of power-law exponent α with peak stress σ_p for different ϕ indicated in the legend. We find that α decreases from higher value with increasing σ_p and saturates around 0.5 (except for $\phi = 57\%$ showing saturation around $\alpha = 1.5$), as indicated by the horizontal dashed line. (b) Shear stress σ as a function of time t (symbols with dotted line) for $\phi = 56\%$. Here the initial power-law behavior disappears and a stretched exponential function ($exp(-(\frac{t}{\tau})^{\beta})$) fits the data well (solid line). (c) σ as a function of t (symbols) for two well known shear jamming systems, the dense suspension of corn starch in water for $\phi = 50.1\%$ with swelling corrections (green) and silica spheres in water glycerol mixture for $\phi = 55\%$ (red). Both the systems show the discontinuity during stress relaxation for sufficiently high value of σ_p where the second part of relaxation can be fitted well with a stretched exponential function (solid line). On the other hand, for the continuous stress relaxation, a power-law cut-off by a stretched exponential function fits reasonably well (dotted line). The dashed line corresponds to $\alpha = 0.5$.

[33]. For sufficiently high σ_p, we see an enhanced brightness of the sample boundary across the entire shear-gap (Movie S1 [36]) due to dilation [34]. The boundary intensity returns back to the initial unperturbed value once the shear stress relaxes below σ_d. Surprisingly, for high σ_p values, where the stress relaxation becomes discontinuous (beyond a critical magnitude of γ), we find randomly distributed bright spots (width: 1 - 2 particle diameter) [Figure 3.6(b) and Figure 3.6(c) also, Movies S1 and S2 [36]] on the sample boundary. At high enough σ_p these bright spots can combine to create a macroscopic fracture in the sample (Figure 3.7). Using oscillatory rheology, we find that the appearance of these bright spots is correlated with the onset of weakening/plasticity of SJ state, as marked by the decrease in slope of G' vs. γ_0 (Figure 3.6(i) - 3.6(l) and Figure 3.8). This implies that these spots indicate localized plasticity/micro-fracture over the particle length scales and we term them as *plastic centers* (PCs). We find that the number of such PCs increases with γ before fracture appears (Figure 3.9).

During stress relaxation, we find that PCs disappear quickly before a gradual decrease of surface intensity takes place. To quantify the time dependence of intensity relaxation

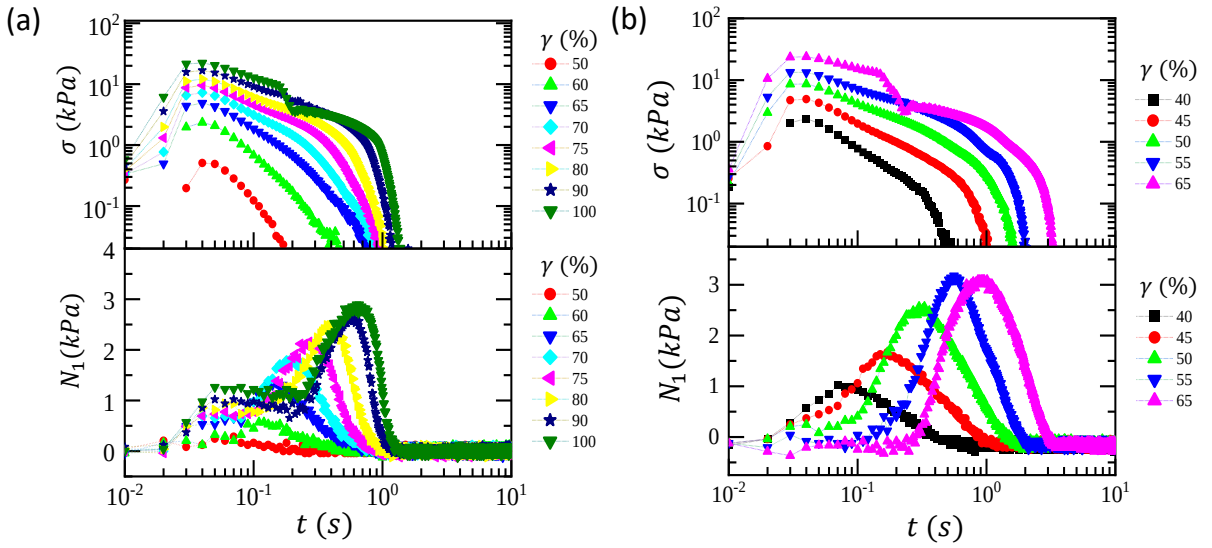

Figure 3.5: Variation of first normal stress difference N_1 with time t for applied strain values γ where continuous stress relaxation is observed. Here, volume fraction $\phi = 58\%$ (panel(a)) and $\phi = 59\%$ (panel(b)). For comparison, only one discontinuous relaxation data is shown for each volume fraction. We see that the magnitude and peak position of N_1 are controlled by the magnitude of the peak stress in the system.

we plot the variation of average intensity $I(t)$ as a function of time over a small region ($\sim 13.6\,\mu m^2$) around each PC (Figure 3.6(a)), as well as, similar regions that do not contain any PC (Figure 3.6(e)). For both of these regions, the intensity relaxation remains self-similar as indicated by the mean curves in Figure 3.6(a) and Figure 3.6(e). For PCs we observe that $I(t)$ shows a two step relaxation similar to $\sigma(t)$. Due to small dynamic range of intensity relaxation, we define the associated timescales from the cross-over points (Figure 3.6(a)). We denote the fast time scale as τ_p and the slower one as τ_d. For regions without PCs, we find that the short-time drop in intensity is missing, but the slower relaxation behavior is very similar to that obtained for PCs. Interestingly, we find that the values of τ_p and τ_d are distributed with peaks around $t \approx 0.2$ s and 2 s, respectively (inset of Figure 3.6(a)) showing a strong correlation with the stress relaxation timescales τ_f and τ_s. This implies that the rapid stress relaxation of the SJ state is related to the dynamics of PC, whereas, the slower relaxation is governed by the dilation dynamics. Nonetheless, dilation is also present during the PC relaxation due to high stress in the system. During the PC relaxation, there is stress injection in the system due to fluidization of local jammed regions. This is reflected in sudden rearrangement and slight enhancement of the surface intensity indicating a stronger dilation beyond $t = \tau_p$ (Figure 3.6(e) and also Movie S2 [36]). This results in the peak in N_1 (around

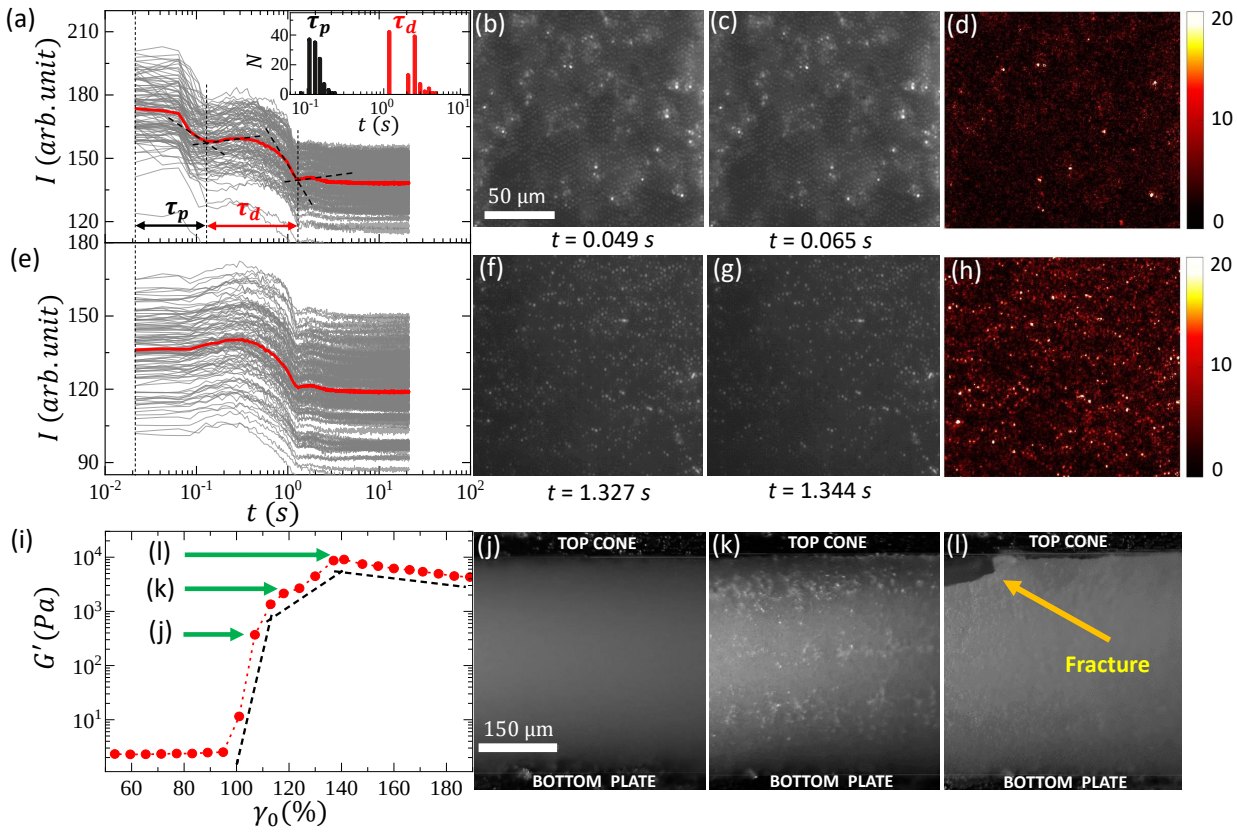

Figure 3.6: Intensity I as a function of time t (gray lines) for different regions with (panel (a)) and without (panel(e)) PCs with the average behaviors (thick red lines) are also indicated. Here, the starting time for each graph corresponds to an absolute time $t = t_0$ as mentioned in Figure 3.1. Relaxation time for PC (τ_p) and dilation (τ_d) are marked with vertical dash lines in (a). Inset: distribution of τ_p and τ_d ($N = 130$). (b) and (c) Consecutive images of the sample boundary, during the fast relaxation and the corresponding difference image is shown in (d). (f) and (g) Consecutive images of the sample boundary, during slow relaxation and the corresponding difference image shown in (h). (i) Elastic modulus (G') vs. strain amplitude (γ_0). Dashed lines represent the slope in different γ_0 regimes with the corresponding boundary images shown in panels (j), (k) and (l). $\phi = 61\%$ and $\eta_l = 80\ mPa.s$ in all cases.

$t = 1$ s in Figure 3.1(c)). Such dynamic local jammed regions have also been observed in recent simulations [37]. To get a deeper insight into this striking intensity relaxation dynamics, we calculate the intensity difference between two consecutive images $\Delta I = |I(x, y, t) - I(x, y, t + \Delta t)|$ ($\Delta t = 0.016$ s) during both PC (Figure 3.6(b) and 3.6(c)) and dilation (Figure 3.6(f) and 3.6(g)) relaxation. Appearance of a bright spot in ΔI at a particular spatial position indicates a local particle rearrangement at that position over a time Δt. We find that during PC relaxation ΔI shows only a few isolated bright

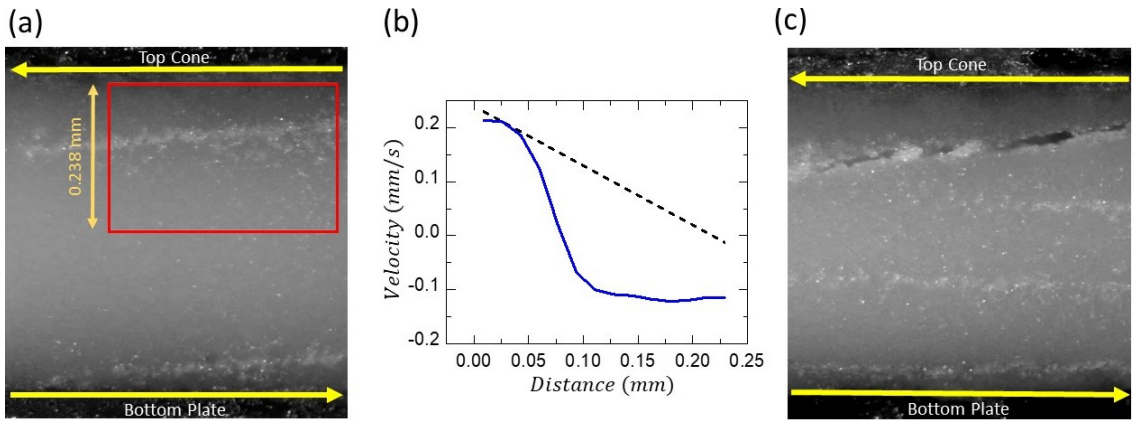

Figure 3.7: (a) Plastic center accumulation along a line (shear strain $\gamma = 70\%$). Such line of PC under high stress forms a macroscopic crack. Red box represents the region of interest (ROI) for the velocity profile calculation around the line of PC with the velocity profile shown in (b). In panel (b), blue solid line represents measured velocity profile across the ROI which significantly deviates from the linear velocity profile (black dashed line), indicating strong non-affine deformation across the line of plastic centers. (c) Image of macroscopic fracture in the sample under large step strain deformation (shear strain $\gamma = 120\%$).

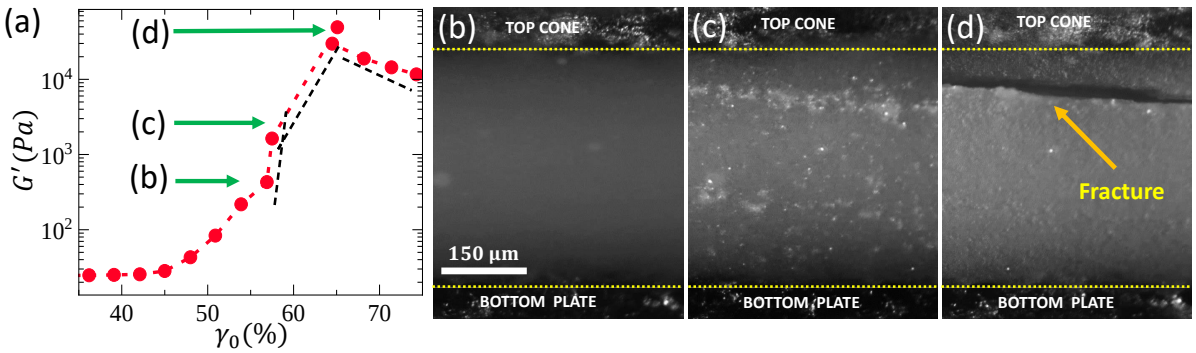

Figure 3.8: (a) Variation of elastic modulus (G') with strain amplitude (γ_0). The dashed lines represent the slope of the curves in different γ_0 regimes. The surface images on the right panels correspond to three different points marked as (b),(c) and (d) (also indicated by arrows) in (a). Image around point (b) shows no signature of plasticity whereas significant bright spots start appearing around point (c) with the decrease in slope of G' as a function of γ_0. These bright spots combined to form macroscopic fractures that result in a decrease of G' beyond point (d). The change in slope of G' around point (c) represents the weakening of the system with the appearance of microscopic plasticity in the form of bright spots which leads to macroscopic fracture in the system.

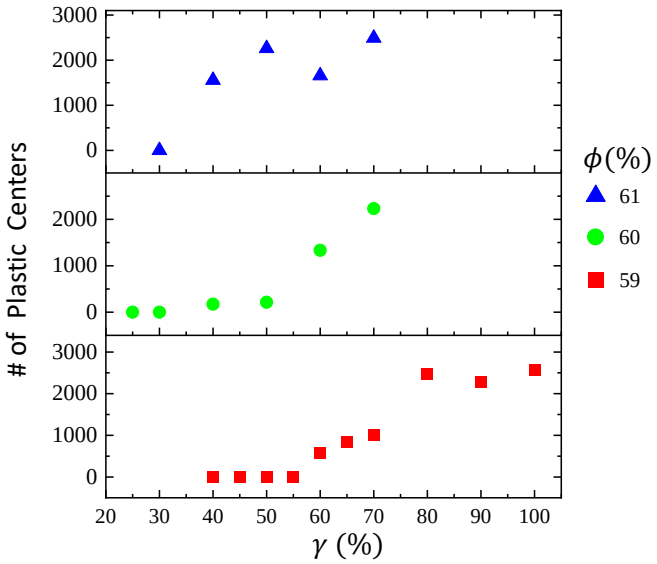

Figure 3.9: Number of plastic centers as a function of applied step strain γ for different volume fraction ϕ, as shown in the legend. For each ϕ value the number of plastic centers increases with increasing γ beyond a strain onset.

spots (Figure 3.6(d)), whereas, during dilation relaxation we obtain a large number of bright spots uniformly distributed throughout the field of view (Figure 3.6(h)). This indicates that PC relaxation is governed by abrupt localized rearrangements, whereas, dilation relaxation happens by more gradual rearrangements throughout the system. We conjecture that since the PCs are sensitive to only local constraints, PC relaxation is much faster compared to dilation relaxation involving global constraints. Such picture physically predicts the origin of the temporally distinct stress relaxation regimes. We do not observe any significant change in average particle distribution before and after the PC relaxation (Figure 3.10), further confirming the spatially localized nature of PC relaxation. In our system, the interparticle contact formation time scale $\eta_l \dot{\gamma}/\sigma* \sim 4 \times 10^{-4}$ s ($\sigma*$: onset stress for contact formation) is negligible compared to the relaxation time scales, implying that the relaxation is governed by the relaxation dynamics of contact networks [38, 25]. Importantly, such contact networks not only get stronger with increasing applied stress, but beyond a critical value significant stress induced reorganizations can happen through buckling and eventual breaking of the force chains [39, 22] close to jamming. For rigid particle systems such buckling can take place even at moderate stress values due to small area of contact (see Appendix-3). We also correlate the local plastic rearrangements with the discontinuous stress relaxation. We find an enhancement of the number of such rearrangements at the point of sharp stress drop (Figure 3.11). Such correspondence has

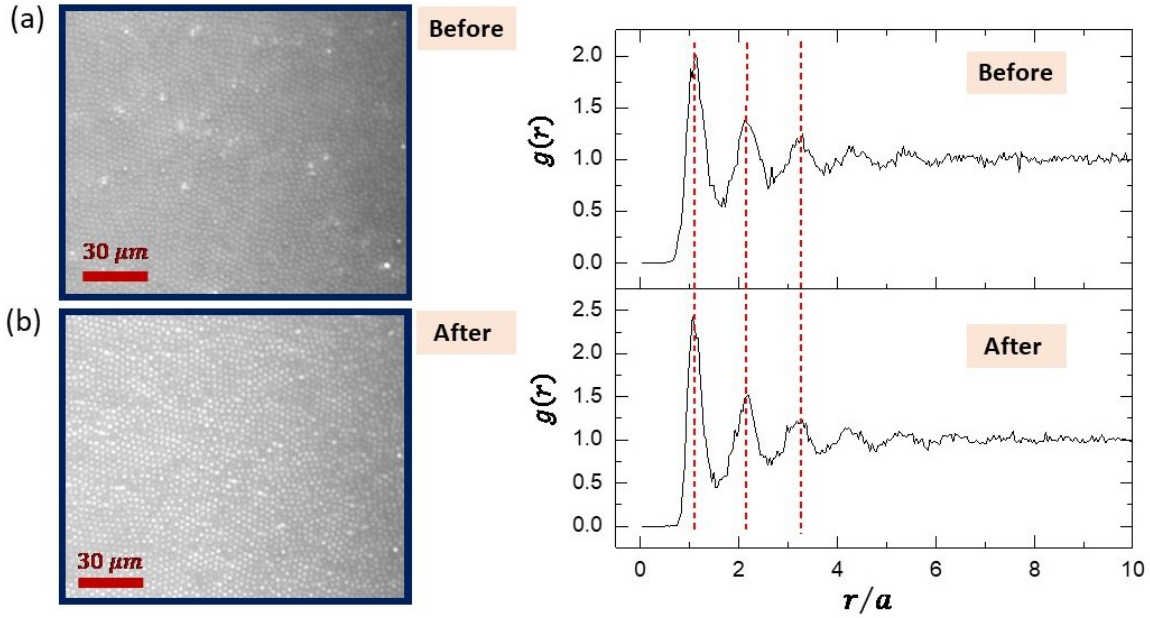

Figure 3.10: Boundary images before (panel (a)) and after (panel (b)) the PC relaxation. The corresponding radial distribution function $g(r)$ as a function of r/a where a is the diameter of the particle. Similar peak positions indicate that there is no significant difference in particle arrangements before and after the PC relaxation. In both the cases the $g(r)$ shows a short-range correlation that decays over a few particle diameters indicating the absence of any crystalline order in the system.

also been observed in the context of granular plasticity [40, 41]. In dry granular systems, X-ray tomography reveals that equivalent to nearest neighbour exchange (T1 events) in 2-D, particle-pair exchange neighbours resulting in defects of poly-tetrahedral order in 3-D [42]. However, we do not observe any T1 event from our 2-D imaging.

To test our conjecture regarding the fast and slow time-scales, we probe the effect of solvent viscosity (η_l) and particle volume fraction (ϕ) on the stress/intensity relaxation time scales. We see from Figure 3.12(a) that the average value of fast time-scales obtained from the stress relaxation (τ_f) and boundary imaging (τ_p) remain almost independent of ϕ. However, the slow time scales τ_s and τ_d show an increasing trend with the increase in ϕ before saturating for $\phi \geq 59\%$. Similar trend is also observed for the change in solvent viscosity (Figure 3.12(a), inset): τ_f remains independent of η_l but, τ_s increases with the increase in η_l. These results imply that fast relaxation time-scales are governed by the local plasticity of the contact networks through the particle scale parameters, such as, surface roughness, rigidity, adhesion. On the other hand, slow time scales involving large scale rearrangements in the system should increase due to increase in drag (due to

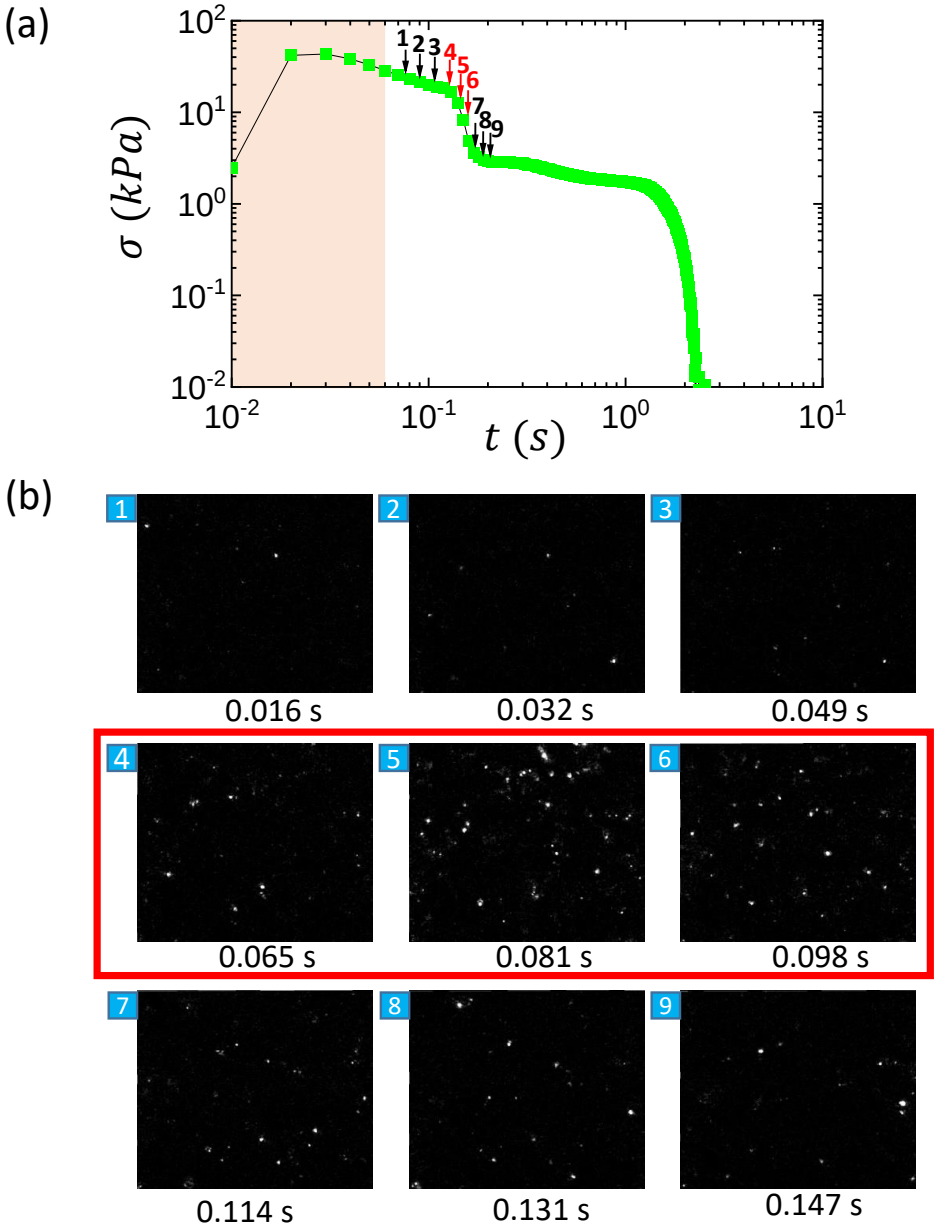

Figure 3.11: (a) Relaxation of shear stress σ with time t for a transient step strain experiment. (b) The stroboscopic difference images obtained from two consecutive images (time separation $\approx$ 16 ms) at different points during fast relaxation process (indicated by the different arrows in (a)). The increased number of isolated bright spots for image number 4, 5 & 6 (indicated by the red box) indicate an enhancement of plastic rearrangements near the sharp stress drop (indicated by the red arrows in (a)).

increase in η_l) or increase in the average coordination number (due to increase in ϕ). Such behavior of longer timescale is also observed in simulation [25]. We find that the time scale obtained from the inverse of onset shear rate for shear-thickening under steady shear ($\tau_i = 1/\dot{\gamma}_c$) shows a good agreement with the slow timescales (Figure 3.12(a)), similar to flow cessation experiments [24]. These observations further confirm our conjecture about the origin of fast and slow time scales.

Finally, we construct a state diagram summarizing the results of transient stress relaxation in the $\sigma - \phi$ parameter plane (Figure 3.12(b)). The onset of SSSJ is obtained from the steady state flow curves (Figure 3.2). As indicated in the diagram, sharp discontinuous stress relaxation (red region) over short time in the SJ regime is observed for high peak stress values $\sigma_p > 16$ kPa. PCs also appear in this regime showing a strong correlation with the discontinuous stress relaxation. The capillary stresses at the solvent-air interface provide the confining stress over a wide range during shear-induced dilation in dense suspensions [43, 34, 5]. Since PC indicates abrupt local curvature due to significant protrusion of isolated particles/small clusters, the local confining stress at the PC can be approximated as the maximum capillary stress $\sim \Gamma/a \approx 16$ kPa. Such capillary stress drives the protruding particle inside the bulk during the discontinuous stress relaxation over a time scale $\eta_t\, a/\Gamma \sim 0.1$ s ($\eta_t = \sigma_p/\dot{\gamma}_p$, see Appendix-4 and Figure 3.13). This time scale is close to the fast relaxation time scale observed in our system. Intriguingly, in-between the discontinuous stress relaxation regime and onset of SSSJ (green region), we obtain a smooth relaxation regime (Figure 3.12(b)) where $\sigma(t) \sim t^{-\alpha}\, e^{-(t/\tau)^{\beta}}$. Below SSSJ, the initial power-law relaxation regime disappears.

3.4 Conclusion

In conclusion, we identify two distinct transient stress relaxation regimes in SJ dense suspensions originating from the dynamics of localized plasticity and system spanning dilation. Recently, an intrinsic contact-relaxation time-scales have been extracted from the coupling of relaxation with the instrument inertia [38]. Also, considering plasticity in the system, recent theoretical models [25] capture the short-time stress relaxation behavior. Although, the relaxation time scales in our system are within the range predicted in [38], the robust initial power-law decay, presumably coming from stress induced force chain buckling/breaking can not be predicted from these models. We find that the fast and slow relaxation time scales are almost independent of step-strain magnitude (Figure 3.14) and the estimated diffusion time-scales are inadequate to quantitatively capture them

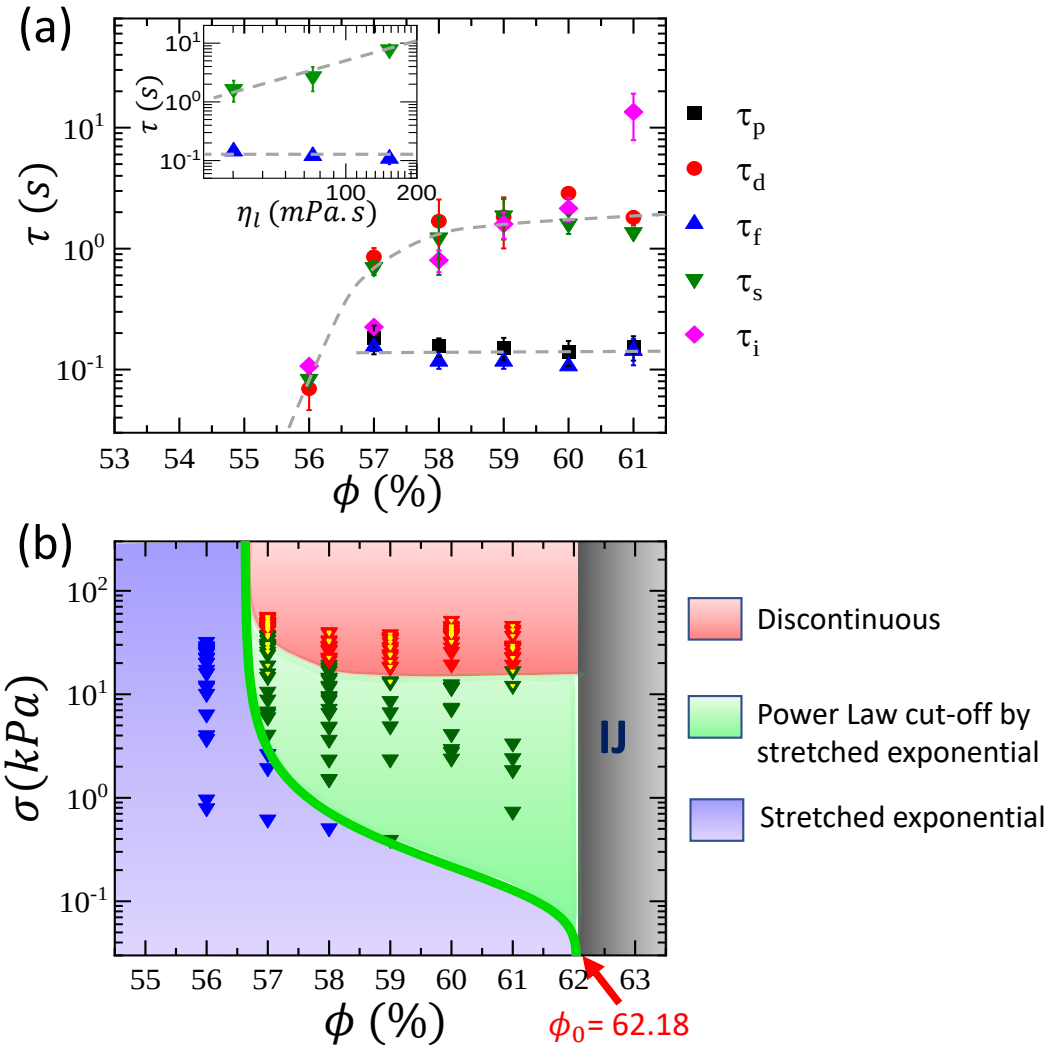

Figure 3.12: (a) Dependance of fast (τ_p and τ_f) and slow (τ_d and τ_s) time scales as a function of volume fraction ϕ. $\tau_i = 1/\dot{\gamma}_c$ obtained from the steady state measurements. Inset shows τ_f and τ_s as a function of η_l. Error bars indicate standard deviation over three independent measurements. Grey dashed lines are guides to the eye. (b) State diagram in $\sigma - \phi$ parameter plane. Thick green line indicates SSSJ onset. In the pink shaded region discontinuous stress relaxation (red triangles) and PCs (yellow dots) are observed, whereas, in green region (with dark-green triangles), a continuous relaxation (power-law cut-off by a stretched exponential) is found. Below SSSJ regime (purple region with blue triangles) initial power-law relaxation behavior disappears. Grey shaded region indicates isotropic jamming. In all cases symbols are the peak stress σ_p obtained from the transient relaxation experiments.

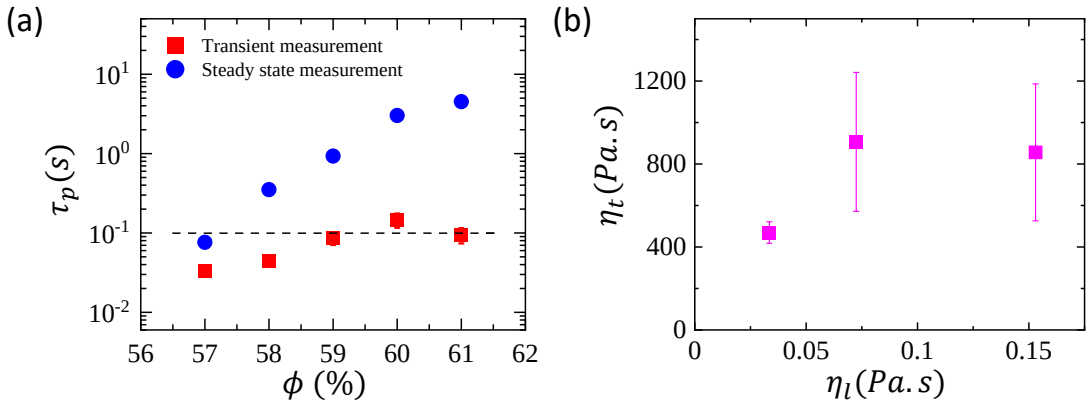

Figure 3.13: Variation of plastic center relaxation time τ_p, calculated using Eq. 3.10, with volume fraction ϕ. Red squares represent τ_p obtained using viscosity (η_t) from transient measurements. For comparison we also estimate τ_p using maximum viscosity (η_{max}) from steady state measurements (blue circles). Horizontal dashed line indicates the timescale of 0.1 s. (b) Transient viscosity (η_t) obtained during the step stain measurements as a function of solvent viscosity η_l. We see that η_t weakly depends on η_l.

(Appendix-5). Our preliminary data for larger polystyrene particles (mean diameter: 6.5 μm) also show similar relaxation dynamics. However, these directions including a possible extension into Brownian regime, require further exploration using more sophisticated experimental techniques [44]. We find an interesting correlation between the transient stress relaxation and the steady-state shear jamming. The continuous stress relaxation showing a power-law cut-off by stretched-exponential behavior is reminiscent of relaxation in frictionless systems close to jamming, implying that for well-constraint systems, the relaxation dynamics is not sensitive to the exact origin of the constraints. Such functional form indicates a wide range of underlying relaxation modes in the system [45]. We also observe similar relaxation behavior including the discontinuous stress relaxation for other SJ dense suspensions, indicating an universal behavior. Although, our study underscores the importance of local-plasticity in controlling the mechanical behavior of SJ systems, deciphering the microscopic nature and dynamics of such plasticity, together with a possible connection to the more general framework of soft glassy rheology [46, 41, 27, 28] potentially unifying the relaxation behavior in SJ and glassy systems, remains an important future direction.

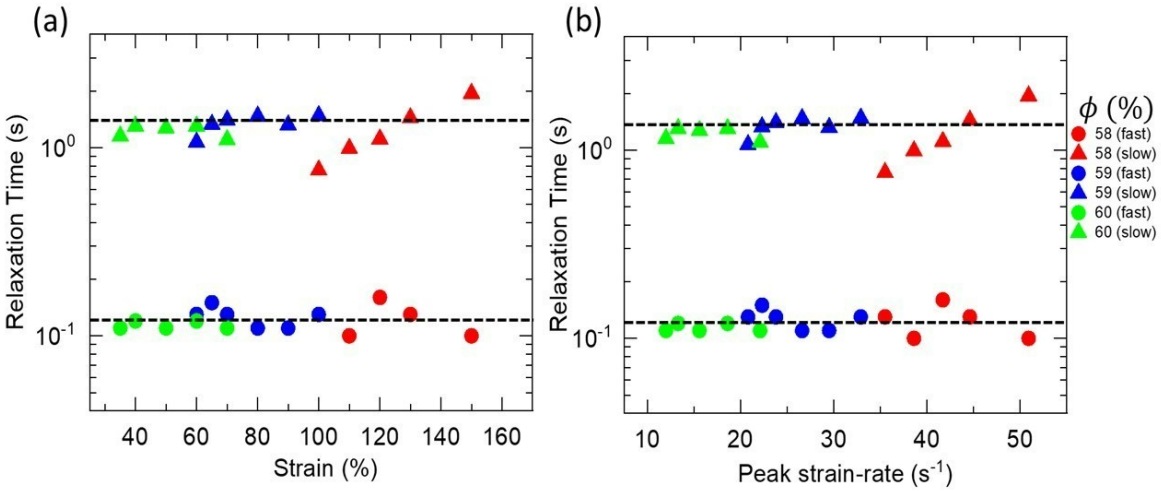

Figure 3.14: Variation of fast (circles) and slow(triangles) relaxation time scales with step strain magnitude (panel (a)) and the peak strain rate (panel (b)) for volume fractions as indicated. The horizontal dashed lines represent the fast and the slow relaxation time for $\phi = 59$ %. The relaxation time scales are almost independent of step strain magnitude, as well as, peak strain rate.

3.5 Appendix

3.5.1 Appendix-1: Movie description

Movie S1: This video depicts the formation of plastic center (PC) along with the enhancement of the sample surface intensity due to dilation under transient step strain perturbation and the corresponding intensity relaxation obtained during the stress relaxation process. Here, a 70% step strain is applied under counter-movement mode, where both the plates move equally in opposite directions. The images are captured using Lumenera Lt545R camera with a 5X long working distance objective (Mitutoyo) at a frame rate of 60 Hz, with resolution 1000×1200 pixels, in flow gradient plane. Here we notice that before the application of shear strain, the sample surface looks liquid-like, but just after the step strain application the overall intensity of the sample boundary surface increases due to dilation. Additionally, we find many tiny bright spots distributed throughout the surface. These tiny bright spots are called plastic centers (PCs) as described before. During the stress relaxation process, we notice that these PCs are relaxing within a very short time scale, whereas, the overall intensity of the sample surface decreases to the initial value with a comparatively longer time scale. Here, the sample volume fraction $\phi = 61\%$ and the movie is played at 10 frames per second [36].

Movie S2: This video shows the formation of the PC along with dilation under step-strain perturbation and the corresponding intensity relaxation during stress relaxation process using a higher magnification. Here, we use a 20X long working distance objective (Mitutoyo) coupled to the camera. The images are captured at a frequency 60 Hz with a resolution of 800×1000 pixels. Higher magnification allows us to observe the individual particles undergoing dilation/forming PCs. We can clearly see that particle protrusions are more in PC regions as compared to dilation regions. In this case also the movie is played at 10 frames per second [36].

3.5.2 Appendix-2: Shear Jamming Boundary from Wyart-Cates Model:

The viscosity (η) of dense suspension can be expressed by Krieger-Dougherty (KD) equation as

$$\eta = \eta_l \left(1 - \frac{\phi}{\phi_J}\right)^{-\beta} \tag{3.1}$$

Where ϕ_J is the jamming volume fraction, ϕ is the volume fraction of the sample, η_l is the solvent viscosity and $\beta \approx 2$ for spherical particles [47].

From Wyart and Cates model (WC model) the jamming volume fraction (ϕ_J) can be written as

$$\phi_J = f(\sigma)\phi_m + [1 - f(\sigma)]\phi_0 \tag{3.2}$$

Where $f(\sigma) = e^{-(\sigma^*/\sigma)}$ denotes the fraction of frictional contacts, σ^* is the onset stress for the frictional interaction, ϕ_0 and ϕ_m represent the jamming volume fraction without any frictional contacts ($f = 0$) and when all the contacts are frictional ($f = 1$) respectively. From KD equation and WC model we find that $\phi_0 = 62.18\%$ and $\phi_m = 56.6\%$ as shown in Figure 3.2(c) and Figure 3.2(d) respectively.

Now, using $\eta = \sigma/\dot{\gamma}$ in Eq. 3.1, we can write

$$\dot{\gamma} = \frac{\sigma}{\eta_l}\left(1 - \frac{\phi}{\phi_J}\right)^{\beta} \tag{3.3}$$

Considering the non-trivial solution ($\sigma \neq 0$) for $\dot{\gamma} = 0$ as the condition for shear

jammed state and using Eq. 3.2, we can get

$$\phi = f(\sigma)\phi_m + [1 - f(\sigma)]\phi_0 \tag{3.4}$$

so,

$$f(\sigma) = \frac{\phi_0 - \phi}{\phi_0 - \phi_m} \tag{3.5}$$

Using $f(\sigma) = e^{-(\sigma^*/\sigma)}$, we get

$$\boxed{\sigma = \frac{\sigma^*}{ln\left(\frac{\phi_0 - \phi_m}{\phi_0 - \phi}\right)}} \tag{3.6}$$

So, using Eq. 3.6 we can find the required stress (σ) for different volume fraction (ϕ) to enter into the shear jammed state.

Similarly, we can obtained the DST boundary using the condition $\frac{dlog(\dot{\gamma})}{dlog(\sigma)} = 0$, which is shown in Chapter 4.

3.5.3 Appendix-3: Estimation of area of contact between the particles:

For a system of particles with particle stiffness G_p the critical buckling load τ_c is given by [22]

$$\tau_c \sim G_p . \frac{A_c^2}{d^4} \tag{3.7}$$

Where A_c is the area of contact and d is the particle diameter.

Now assuming the critical stress for chain buckling to be equal to the onset for discontinuous stress relaxation in our case, we have $\tau_c \sim 16000Pa$ and diameter $d = 2.65\mu m$. For polystyrene particles considering Young's modulus $\sim 3\,GPa$ [48] we get $A_c \sim 16.2 \times 10^{-15} m^2$. Again,

$$\frac{A_c^2}{d^4} = \frac{\tau_c}{G_p.} \tag{3.8}$$

$$\boxed{\frac{A_c}{d^2} = 2.3 \times 10^{-3}}$$

Thus, we find that the area of contact is negligible compared to the surface area of the particles, as expected for rigid particles.

3.5.4 Appendix-4: Estimation of plastic center relaxation time:

From the imaging, we can clearly notice a significant protrusion of the particles at the PC regions in comparison to the surrounding. This indicates that the local stress (σ_L) at the PC approaches the maximum confining stress due to the solvent-air surface tension: Γ/a (a: particle diameter , Γ: surface tension) [34].

When the particle is going back into the bulk it gives rise to an average local shear rate ($\langle\dot{\gamma_L}\rangle$). Thus, the local stress around the particle (assuming overdamped dynamics) is given by,

$$\sigma_L = \eta_t \langle\dot{\gamma_L}\rangle \tag{3.9}$$

Since PCs appear around the peak-stress (σ_p), we consider the transient viscosity (η_t) estimated from the ratio of peak stress (σ_p) developed in the system and the maximum shear rate ($\dot{\gamma_p}$) associated with the applied step strain.

During stress relaxation, the local stress around the particle should comparable to confining stress. Assuming the dynamics to be overdamped we can write:

$$\begin{aligned} \sigma_L = \eta_t \langle\dot{\gamma_L}\rangle &\sim \frac{\Gamma}{a} \\ \frac{1}{\langle\dot{\gamma_L}\rangle} &\sim \frac{\eta_t}{\left(\frac{\Gamma}{a}\right)} \\ \boxed{t \sim \frac{\eta_t a}{\Gamma}} & \end{aligned} \tag{3.10}$$

For our system, $\Gamma \approx 44\ mN/m$, $a = 2.65\ \mu m$. The time scales estimated from Eq. 3.10 is shown in Figure 3.13(a) for different ϕ values. Also, as shown in Figure 3.13(b), η_t depends very weakly on solvent viscosity.

For comparison we also estimate τ_p using maximum viscosity (η_{max}) obtained from steady

state measurements (Figure 3.13(a)).
When we replace η_t in Eq. 3.10 with the solvent viscosity η_l, we get $\tau_p \sim 5 \times 10^{-6}$ s which is far below the experimental observation.
We want to point out that the fast relaxation time scales observed in our case also have some contributions from stress induced reorganization in the system close to jamming (presumably through buckling/breaking of force chains). However, in the estimate mentioned above, we ignore such contributions which are currently unknown in our case.

3.5.5 Appendix-5: Diffusion time scales for the system

We show the variation of the fast and slow relaxation time scales for a range of particle volume fractions and applied step-strain magnitudes in Figure 3.14(a). We find that both the time scales remain almost independent of applied step strain magnitude.

Since our system is weakly Brownian (mean particle diameter $2r = 2.65$ μm), the intrinsic diffusion coefficient (D) at room temperature is very small: $D = \frac{k_B T}{6\pi\eta r} \sim 10^{-15} m^2/s$. Here we have assumed the value of η to be the solvent ~ 0.1 Pa.s. If we assume the η to be the transient viscosity of the suspensions (Figure 3.13), $D \sim 10^{-18} m^2/s$. Thus, intrinsic diffusion time-scale (in 3-D) $t_D \sim \frac{r^2}{6D}$ is orders of magnitude greater than the slower time scale of the system. For soft glassy systems, it is observed that the particle diffusion coefficient under shear has a dependence on associated strain rate and particle diameter (d) as $D \sim d^2\dot{\gamma}$ [49]. Other studies have also found similar relation $D \sim \dot{\gamma}^{0.8}$ [50] for higher shear rate and $D \sim \dot{\gamma}^{0.78}$ at the jamming transition [51]. However, for our case, as the stress relaxation takes place at constant strain, the strain rate is zero during stress relaxation process.

Using a similar formulation as that mentioned in [52], we have also checked the particle diffusivity in our system by replacing the thermal energy with the shear energy. Replacing the thermal energy term $k_B T$ with the shear energy $\frac{4\pi r^3 \eta\dot{\gamma}}{3}$ with the assumption that the characteristic volume is equal to that of a particle, we can write the diffusivity as, $D = \frac{\frac{4\pi r^3 \eta\dot{\gamma}}{3}}{6\pi\eta r} = \frac{2r^2\dot{\gamma}}{9}$.

Now, the diffusion time scale (in 3-D) will be $t_D = r^2/6D = \frac{3}{4\dot{\gamma}}$

From this expression, it is clear that the diffusion time scale is only depends on strain rate. The suspension viscosity and particle diameter play no role.

Although, in our case the strain rate remains zero during the relaxation process, we have considered the peak strain rate ($\dot{\gamma}_p$) associated with the applied step-strain. However, as we see from Figure 3.14(b), both the fast and slow relaxation time scales are almost

independent of the peak strain rate. Also, the values of the diffusion time-scales obtained for the range of peak strain rate values probed in our experiments ($\sim$ 10 to 50 s^{-1}, see Figure 3.14(b)) come out to be in the range 0.015 to 0.075 s which is significantly smaller than the time-scales observed in our experiments. This indicates that the colloidal time scales are not quantitatively capturing the observed relaxation time scales for the shear jammed state.

Bibliography

[1] Sachidananda Barik and Sayantan Majumdar. Origin of two distinct stress relaxation regimes in shear jammed dense suspensions. *Phys. Rev. Lett.*, 128:258002, Jun 2022.

[2] HA Barnes. Shear-thickening ("dilatancy") in suspensions of nonaggregating solid particles dispersed in newtonian liquids. *Journal of Rheology*, 33(2):329–366, 1989.

[3] RL Hoffman. Discontinuous and dilatant viscosity behavior in concentrated suspensions. i. observation of a flow instability. *Transactions of the Society of Rheology*, 16(1):155–173, 1972.

[4] Norman J Wagner and John F Brady. Shear thickening in colloidal dispersions. *Physics Today*, 62(10):27–32, 2009.

[5] Eric Brown and Heinrich M Jaeger. Shear thickening in concentrated suspensions: phenomenology, mechanisms and relations to jamming. *Reports on Progress in Physics*, 77(4):046602, 2014.

[6] Eric Brown, Nicole A Forman, Carlos S Orellana, Hanjun Zhang, Benjamin W Maynor, Douglas E Betts, Joseph M DeSimone, and Heinrich M Jaeger. Generality of shear thickening in dense suspensions. *Nature materials*, 9(3):220–224, 2010.

[7] Matthieu Wyart and ME Cates. Discontinuous shear thickening without inertia in dense non-brownian suspensions. *Physical Review Letters*, 112(9):098302, 2014.

[8] Ryohei Seto, Romain Mari, Jeffrey F Morris, and Morton M Denn. Discontinuous shear thickening of frictional hard-sphere suspensions. *Physical Review Letters*, 111(21):218301, 2013.

[9] Romain Mari, Ryohei Seto, Jeffrey F Morris, and Morton M Denn. Shear thickening, frictionless and frictional rheologies in non-brownian suspensions. *Journal of Rheology*, 58(6):1693–1724, 2014.

[10] BM Guy, Michiel Hermes, and Wilson CK Poon. Towards a unified description of the rheology of hard-particle suspensions. *Physical Review Letters*, 115(8):088304, 2015.

[11] Young S Lee, Eric D Wetzel, and Norman J Wagner. The ballistic impact characteristics of kevlar® woven fabrics impregnated with a colloidal shear thickening fluid. *Journal of materials science*, 38(13):2825–2833, 2003.

[12] Abhijit Majumdar, Bhupendra Singh Butola, and Ankita Srivastava. Optimal designing of soft body armour materials using shear thickening fluid. *Materials & Design*, 46:191–198, 2013.

[13] Ivo R Peters, Sayantan Majumdar, and Heinrich M Jaeger. Direct observation of dynamic shear jamming in dense suspensions. *Nature*, 532(7598):214–217, 2016.

[14] Sayantan Majumdar, Ivo R Peters, Endao Han, and Heinrich M Jaeger. Dynamic shear jamming in dense granular suspensions under extension. *Physical Review E*, 95(1):012603, 2017.

[15] Endao Han, Ivo R Peters, and Heinrich M Jaeger. High-speed ultrasound imaging in dense suspensions reveals impact-activated solidification due to dynamic shear jamming. *Nature communications*, 7(1):1–8, 2016.

[16] Abhinendra Singh, Sidhant Pednekar, Jaehun Chun, Morton M Denn, and Jeffrey F Morris. From yielding to shear jamming in a cohesive frictional suspension. *Physical Review Letters*, 122(9):098004, 2019.

[17] BM Guy, JA Richards, DJM Hodgson, E Blanco, and WCK Poon. Constraint-based approach to granular dispersion rheology. *Physical Review Letters*, 121(12):128001, 2018.

[18] Nicole M James, Endao Han, Ricardo Arturo Lopez de la Cruz, Justin Jureller, and Heinrich M Jaeger. Interparticle hydrogen bonding can elicit shear jamming in dense suspensions. *Nature materials*, 17(11):965–970, 2018.

[19] Subhransu Dhar, Sebanti Chattopadhyay, and Sayantan Majumdar. Signature of jamming under steady shear in dense particulate suspensions. *Journal of Physics: Condensed Matter*, 32(12):124002, 2019.

[20] Abhinendra Singh, Christopher Ness, Ryohei Seto, Juan J de Pablo, and Heinrich M Jaeger. Shear thickening and jamming of dense suspensions: The "roll" of friction. *Physical Review Letters*, 124(24):248005, 2020.

[21] Safa Jamali and John F Brady. Alternative frictional model for discontinuous shear thickening of dense suspensions: Hydrodynamics. *Physical Review Letters*, 123(13):138002, 2019.

[22] Aaron S Baumgarten and Ken Kamrin. A general constitutive model for dense, fine-particle suspensions validated in many geometries. *Proceedings of the National Academy of Sciences*, 116(42):20828–20836, 2019.

[23] P d'Haene, Joannes Mewis, and GG Fuller. Scattering dichroism measurements of flow-induced structure of a shear thickening suspension. *Journal of colloid and interface science*, 156(2):350–358, 1993.

[24] Rijan Maharjan and Eric Brown. Giant deviation of a relaxation time from generalized newtonian theory in discontinuous shear thickening suspensions. *Physical Review Fluids*, 2(12):123301, 2017.

[25] Aaron S Baumgarten and Ken Kamrin. Modeling stress relaxation in dense, fine-particle suspensions. *Journal of Rheology*, 64(2):367–377, 2020.

[26] Saisai Cao, Qianyun He, Haoming Pang, Kaihui Chen, Wanquan Jiang, and Xinglong Gong. Stress relaxation in the transition from shear thinning to shear jamming in shear thickening fluid. *Smart Materials and Structures*, 27(8):085013, 2018.

[27] Lavanya Mohan, Michel Cloitre, and Roger T Bonnecaze. Build-up and two-step relaxation of internal stress in jammed suspensions. *Journal of Rheology*, 59(1):63–84, 2015.

[28] Yihao Chen, Simon A Rogers, Suresh Narayanan, James L Harden, and Robert L Leheny. Microscopic dynamics of stress relaxation in a nanocolloidal soft glass. *Physical Review Materials*, 4(3):035602, 2020.

[29] Scott R Waitukaitis and Heinrich M Jaeger. Impact-activated solidification of dense suspensions via dynamic jamming fronts. *Nature*, 487(7406):205–209, 2012.

[30] Takahiro Hatano. Growing length and time scales in a suspension of athermal particles. *Physical Review E*, 79(5):050301, 2009.

[31] Atsushi Ikeda, Takeshi Kawasaki, Ludovic Berthier, Kuniyasu Saitoh, and Takahiro Hatano. Universal relaxation dynamics of sphere packings below jamming. *Physical Review Letters*, 124(5):058001, 2020.

[32] Dong Wang, Bing Yu, Hai-Lin Cong, Yue-Zhong Wang, Qian Wu, and Ji-Lei Wang. Synthesis of monodisperse polystyrene microspheres by seeding polymerization. *Integrated Ferroelectrics*, 147(1):41–46, 2013.

[33] Swarnadeep Bakshi, Vaisakh V Mohanan, Ritwick Sarkar, and Sayantan Majumdar. Strain localization and yielding dynamics in disordered collagen networks. *Soft Matter*, 2021.

[34] Eric Brown and Heinrich M Jaeger. The role of dilation and confining stresses in shear thickening of dense suspensions. *Journal of Rheology*, 56(4):875–923, 2012.

[35] John R Royer, Daniel L Blair, and Steven D Hudson. Rheological signature of frictional interactions in shear thickening suspensions. *Physical Review Letters*, 116(18):188301, 2016.

[36] http://hdl.handle.net/2289/8300.

[37] Ryohei Seto, Abhinendra Singh, Bulbul Chakraborty, Morton M Denn, and Jeffrey F Morris. Shear jamming and fragility in dense suspensions. *Granular Matter*, 21(3):1–8, 2019.

[38] James A Richards, John R Royer, Benno Liebchen, Ben M Guy, and Wilson CK Poon. Competing timescales lead to oscillations in shear-thickening suspensions. *Physical Review Letters*, 123(3):038004, 2019.

[39] ME Cates, JP Wittmer, J-P Bouchaud, and Ph Claudin. Jamming, force chains, and fragile matter. *Physical Review Letters*, 81(9):1841, 1998.

[40] Axelle Amon, Ary Bruand, Jérôme Crassous, Eric Clément, et al. Hot spots in an athermal system. *Physical Review Letters*, 108(13):135502, 2012.

[41] Antoine Le Bouil, Axelle Amon, Sean McNamara, and Jérôme Crassous. Emergence of cooperativity in plasticity of soft glassy materials. *Physical Review Letters*, 112(24):246001, 2014.

[42] Yixin Cao, Jindong Li, Binquan Kou, Chengjie Xia, Zhifeng Li, Rongchang Chen, Honglan Xie, Tiqiao Xiao, Walter Kob, Liang Hong, et al. Structural and topological nature of plasticity in sheared granular materials. *Nature Communications*, 9(1):1–7, 2018.

[43] Lev A Slobozhanin, J Iwan D Alexander, Steven H Collicott, and S Roberto Gonzalez. Capillary pressure of a liquid in a layer of close-packed uniform spheres. *Physics of Fluids*, 18(8):082104, 2006.

[44] Shravan Pradeep, Mohammad Nabizadeh, Alan R Jacob, Safa Jamali, and Lilian C Hsiao. Jamming distance dictates colloidal shear thickening. *Physical Review Letters*, 127(15):158002, 2021.

[45] Daniel Hexner, Andrea J Liu, and Sidney R Nagel. Role of local response in manipulating the elastic properties of disordered solids by bond removal. *Soft matter*, 14(2):312–318, 2018.

[46] Peter Sollich, François Lequeux, Pascal Hébraud, and Michael E Cates. Rheology of soft glassy materials. *Physical Review Letters*, 78(10):2020, 1997.

[47] Abhinendra Singh, Romain Mari, Morton M Denn, and Jeffrey F Morris. A constitutive model for simple shear of dense frictional suspensions. *Journal of Rheology*, 62(2):457–468, 2018.

[48] *https://omnexus.specialchem.com/polymer-properties/properties/young-modulus*. 2022.

[49] Brian Utter and Robert P Behringer. Self-diffusion in dense granular shear flows. *Physical Review E*, 69(3):031308, 2004.

[50] R Besseling, Eric R Weeks, AB Schofield, and WCK Poon. Three-dimensional imaging of colloidal glasses under steady shear. *Physical Review Letters*, 99(2):028301, 2007.

[51] Peter Olsson. Diffusion and velocity autocorrelation at the jamming transition. *Physical Review E*, 81(4):040301, 2010.

[52] Christoph Eisenmann, Chanjoong Kim, Johan Mattsson, and David A Weitz. Shear melting of a colloidal glass. *Physical review letters*, 104(3):035502, 2010.

CHAPTER

FOUR

Signature of structural memory in shear jammed dense suspension

"Memory is deceptive
because it is colored by today's events."
- Albert Einstein -

4.1 Introduction

A broad range of systems are classified as soft jammed systems, encompassing glasses, foams, dense granular materials, colloids, and more [1, 2, 3, 4]. Many of these systems are inherently jammed and exhibit a yield stress. In addition, slow relaxation dynamics and the existence of residual stress are also the major characteristics of these systems. Such static jammed and glassy materials can store the information of their past deformation and under suitable read-out protocol, this information can be retrieved. The training-induced structural evolution is found to be the key to such memory formation in these systems. However, in the case of dense particulate suspension showing discontinuous shear thickening and shear jamming, the stress relaxation is very fast. As discussed before these systems are liquid-like at rest and only get jammed under rapid perturbation due to stress-induced system spanning frictional contacts. Once the perturbation is removed the system goes back to its initial liquid-like state within just a few seconds. This highlights the fundamental difference in interparticle interactions in these systems as compared to the static jammed materials mentioned above.

In Chapter 3, we show that under transient step strain perturbation, the stress in a shear jammed system attains a peak value and relaxes completely within just a couple of seconds. Also, we find that such fast stress relaxation in shear-jammed suspensions is correlated to the relaxation of the localized plasticity and system-spanning dilation [5]. Although it is expected that the stress relaxation is related to the relaxation of the system spanning contact network [6, 7], it is not clear whether the liquid-like state obtained after the removal of the perturbation is structurally similar to the initial liquid-like state before the perturbation. This is a non-trivial point as the linear viscoelastic response in these states is almost identical.

In the shear thickening systems, a recent study observed that under oscillatory measurement, some high-stress regions start to appear above a critical shear rate, which persists under subsequent cycles despite the fact that the system is going through a low shear rate in each cycle [8]. Combining both shear reversal and cessation protocol with oscillatory measurements the presence of residual microstructure was also predicted [9]. Using shear thicking suspension of piezoelectric nanoparticles, the existence of residual contact stress was observed for the state where the system is not contact force dominated [10]. In shear-jammed dense suspensions, the speed of jamming front propagation is found to be sensitive to the previous direction of shear at a very slow rate [11]. Using acoustic perturbation, a very recent work demonstrates the encoding of structural memory

in shear jammed state of dense suspension formed under constant stress conditions [12]: They demonstrate that if the system is trained with the acoustic perturbation of higher power then the force chain structure in the shear-jammed state rearranges among itself such that it does not get affected by the acoustic perturbation of lower power. However, from these handfuls of studies, the effect of a structural memory in controlling the bulk mechanical properties of shear-jammed state correlating with the microscopic force chain structures remains unclear.

In this chapter, we explore the self-organization of a dense suspension showing DST and SJ under a series of unidirectional step strain perturbations. Remarkably, we observe an enhancement of the system response even if the waiting time between the successive pulses is much larger than the bulk stress relaxation time scale. This indicates the formation of a structural memory that relaxes over a much longer time scale compared to the bulk stress relaxation time scale of the system. Interestingly, we observe that if the perturbations are applied in the alternative direction, we do not observe any such enhancement. Using in-situ optical imaging, shear reversal measurements, and with the help of numerical simulation we shed light on the microscopic mechanism giving rise to such memory effect and highlight the role of shear-induced rigid clusters in controlling such memory formation.

4.2 Materials and methods

The dense particulate suspension is prepared by dispersing mono-disperse polystyrene (PS) particles (diameter: $2.8 \pm 0.15\ \mu m$) in a Newtonian solvent polyethylene glycol (PEG 400) over a wide range of volume fractions as described in chapter 2.

All the rheological measurements are carried out on a stress control Rheometer (MCR-702, Anton Paar, Austria) in twin drive under 50-50 counter movement mode with 12.5 mm radius cone and plate geometry. After loading the sample we conduct a large amplitude oscillatory shear (LAOS) measurement at a frequency 1 Hz, where we first increase the strain amplitude (γ_0) logarithmically from a lower to a maximum value and then we perform a reverse run where the amplitude is again gradually decreased to the initial value. We observe the variation of storage (G') and loss (G'') moduli and mark the onset strain value for shear thickening where the G' and G'' show an abrupt increase. To study the effect of stress relaxation over structural relaxation, the sample is subjected to multiple step shear strain perturbations. The magnitude of the step strain (γ) at each step and the time interval between two consecutive steps remains constant. We keep the

magnitude of the step strain around the onset strain for shear thickening obtained from the LAOS measurement. The resulting stress response of the sample is recorded at each step.

4.3 Results and discussion

In Chapter 3 we observed that, in a system exhibiting DST and SJ, applying a step strain perturbation of a certain magnitude (γ) causes stress within the system to rapidly reach a peak value (σ_p) and then fully relax within a few seconds [5]. Here, instead of applying a single step perturbation, we apply multiple steps in a particular direction. The magnitude of the step strain is chosen around that strain value where the G' and G'' show an abrupt jump during the LAOS measurement (Figure 4.1(a)). As mentioned earlier, the

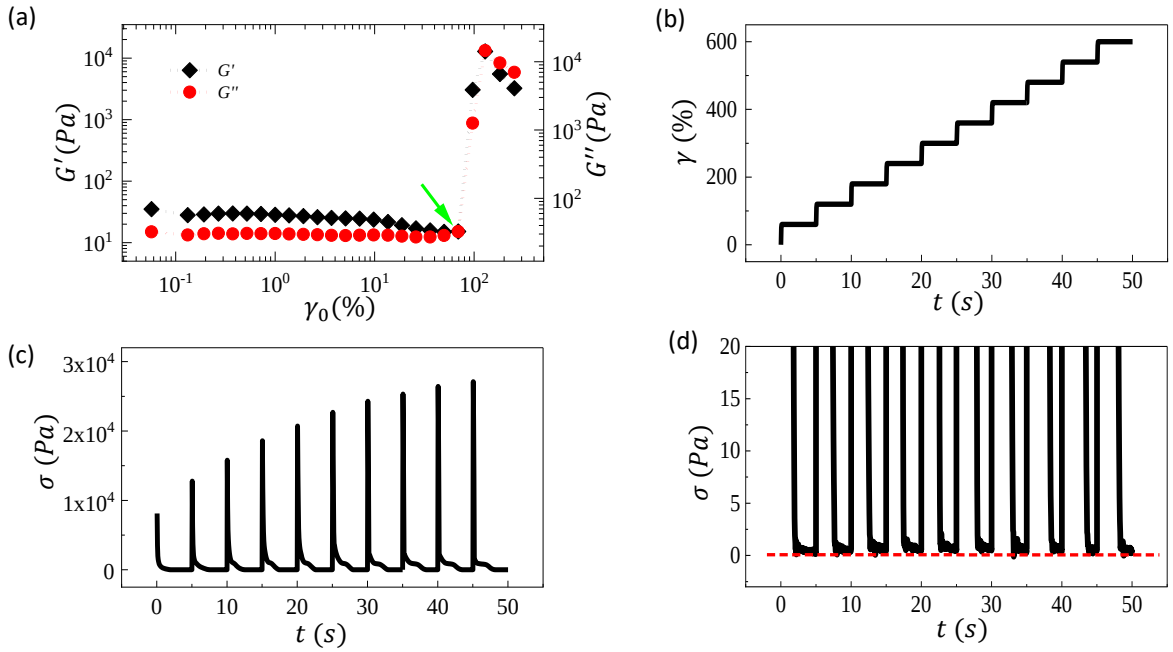

Figure 4.1: (a) Variation of storage modulus (G') and loss modulus (G'') with strain amplitude (γ_0). The onset strain for shear thickening is indicated by the green arrow. (b) The input protocol for unidirectional repetitive step strains of step magnitude 60% and $5s$ waiting time between two consecutive steps. (c) Stress σ as a function of time t, corresponds to the input shown in (b). (d) The magnified plot of the same data is shown in (c), where the horizontal dashed line indicates stress σ=0. The volume fraction $\phi = 61\%$.

strain magnitude of each step and the time interval between two consecutive steps remain constant throughout the experiment. It is to be noted that, we choose the time interval

between two consecutive steps to be sufficiently larger than the stress relaxation time scale. Figure. 4.1(b) represents a typical input protocol for a train of unidirectional step strain pulses of magnitude 60% with 5 seconds waiting time (t_w) between the consecutive steps. The corresponding stress response is shown in Figure 4.1(c). From Figure 4.1(c) it is observed that the step strain perturbation drives the stress in the system to attain a peak (σ_p) instantaneously and then relaxes quickly. Interestingly, after the complete relaxation of the stress, if the system is again perturbed with the same magnitude of step strain in the same direction, the stress in the system attains a higher peak value than that in the previous step. Such increase in σ_p with step number (N) continues for a certain number of steps until the σ_p reaches a saturation. It is to be noted that, before any step strain perturbation, the stress in the system always relaxes to a negligible value (Figure 4.1(d)). This indicates that even after the relaxation of ∼4 orders of magnitude stress, the system seems to remember the previous state of the sample. For a shear-thickening dense suspension, as the system becomes liquid-like after the stress relaxation, such a picture of memory is highly non-intuitive.

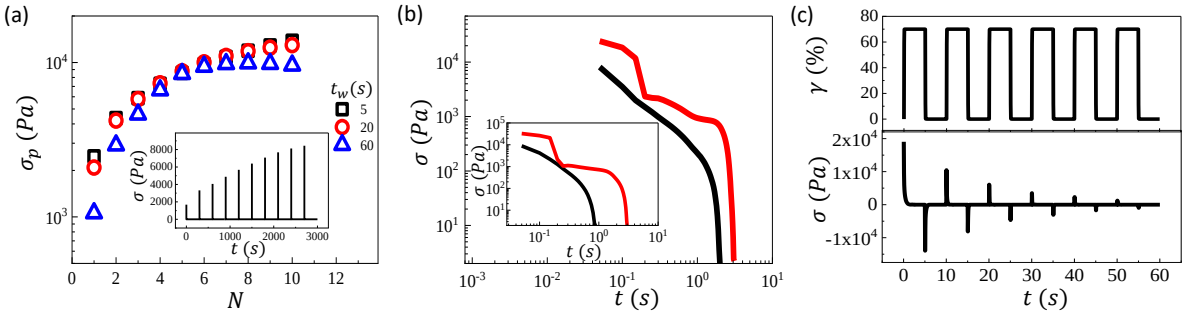

Figure 4.2: (a) The variation of peak stress σ_p with step number N for a particular volume fraction ($\phi = 60\%$) with three different waiting times t_w between consecutive steps, as shown in the legend. Inset: Stress response for $\phi = 61\%$ with 5 minutes waiting time between consecutive steps at step magnitude 100%. (b) The stress relaxation behavior during the first step (black line) and seventh step (red line) for the data shown in 4.1(c) with $5s$ waiting time between two consecutive steps. Inset: The stress relaxation behavior during the first step (black line) and seventh step (red line) for a data set with $t_w = 60s$. (c) The top panel shows the input protocol for repetitive step strains alternatively changing the shear direction. Here, the step magnitude is 60% and the waiting time between two consecutive steps is $5s$. The corresponding stress response is shown in the bottom panel.

We further explore such memory phenomena for longer waiting times between consecutive steps. Figure 4.2(a) represents the variation of σ_p for three different waiting times (t_w) (5s, 20s, 60s) at a particular volume fraction $\phi = 60\%$. This indicates that even

if the waiting time between the consecutive intervals increases to more than an order of magnitude higher than the stress relaxation time scale (which is 2-3 seconds), where no residual stress is observed, the system response gradually becomes stronger under subsequent unidirectional step strain perturbations. Such signature of memory is also observed for $t_w = 5$ *minutes* (Inset of Figure 4.2(a)) which is more than two orders of magnitude higher than the stress relaxation time scale. Furthermore, such change in system response is also reflected in the nature of stress relaxation. Figure 4.2(b) represents the stress relaxation behavior during the first step and the seventh step of the input perturbation, as shown in Figure 4.1(c). During the initial steps, when the σ_p value is comparatively small, we observe a smooth relaxation of stress (black line), whereas, at higher σ_p, the nature of stress relaxation exhibits a two-step nature with an initial sharp discontinuity (red line). Such transition from continuous to discontinuous relaxation behavior is also evident for longer t_w (inset of Figure 4.2(b)). We already discussed this drastic change in relaxation nature in Chapter 3, where two distinct relaxation natures were observed in different stress regimes of shear jammed state.

Now, we explore the shear direction dependence of such memory effect. Instead of applying a unidirectional series of step strain pulses we change the direction of the shear alternatively as shown in the top panel of Figure 4.2(c). The corresponding stress response is shown in the bottom panel of Figure 4.2(c). From Figure 4.2(c) we observe that if the direction of the step strain changes alternatively, we do not observe any increase in σ_p under repetitive perturbation. In fact, σ_p gradually decreases with increasing step number.

Next, we study the effect of particle volume fraction on the observed memory effect. Interestingly, we observe that such increase in σ_p under unidirectional repetitive step strain perturbation is observed only for $\phi \geq 57\%$, but for $\phi = 56\%$, the σ_p does not show any systematic increase and remains around a constant value (Figure 4.3(a)). This suggests that such memory effect of shear thickening dense particulate system is closely related to the particle concentration in the system. Turns out, for our system, the range of ϕ over which such memory effect is observed is above the minimum shear jamming volume fraction ϕ_m. As we go below the ϕ_m, we don't observe such memory effect. Figure 4.3(b) represents the state diagram for the dense suspension used in our case, where the shear jamming and DST boundary are obtained using the Wyart-Cates model (see Appendix 2 in Chapter 3). From this, we observe that for any particular $\phi \geq 57\%$ the repetitive perturbation drives the peak stress in the system to higher values, but for $\phi = 56\%$, the peak stress does not vary much. This observation highlights a strong correlation between shear jamming (SJ) and memory formation in dense particulate suspension.

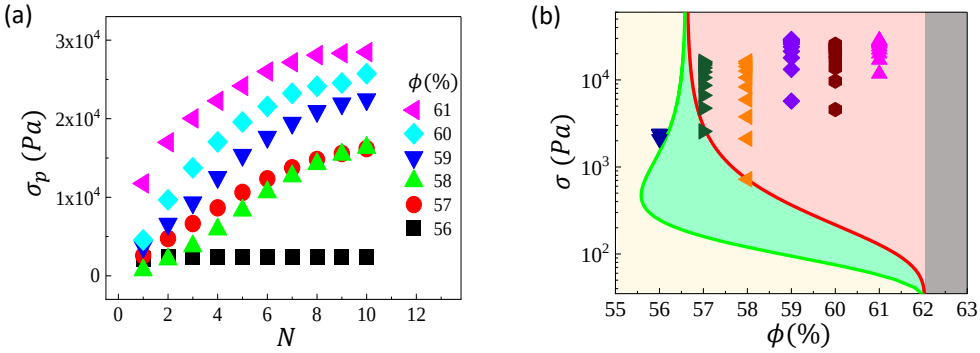

Figure 4.3: (a) Peak stress σ_p variation under repetitive unidirectional step strain perturbation for different volume fraction ϕ, as shown in the legend, with $20s$ waiting time between two consecutive steps. (b) State diagram in $\sigma - \phi$ parameter plane. The thick red line indicates steady state SJ boundary (pink shaded region) and the thick green line indicates steady state DST boundary (green shaded region) obtained from Wyart and Cates model (see appendix 2 in Chapter 3). For any particular ϕ value, the symbols represent the peak stress evolution under repetitive step strain perturbation as shown by different colors.

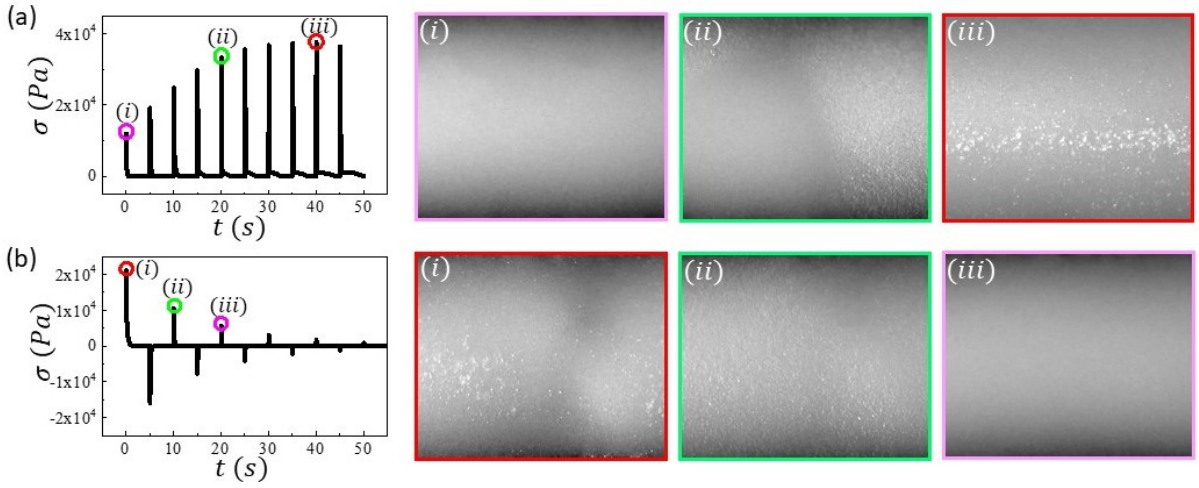

Figure 4.4: (a) Stress variation under unidirectional step strain perturbation of step magnitude 70% at $\phi = 61\%$. The sample boundary images corresponding to the peak stress for three different steps, as marked by magenta (i), green (ii), and red (iii) circles, are shown on the right. (b) Stress variation under step strain perturbation in the alternative reverse direction with step magnitude 80% at $\phi = 61\%$. The sample boundary images corresponding to the peak stress for three different steps, as marked by red (i), green (ii), and magenta (iii) circles, are shown on the right.

We further confirm such transition in mechanical properties using the in-situ optical boundary imaging technique. We carefully observe the sample boundary images correspond to the peak stress values. In Figure 4.4, panel (a) represents a typical stress evolution under unidirectional step strain perturbation, and the sample boundary images, shown on the right (top panel), correspond to the peak stress for three different steps as marked in the plot. For the first step, where the σ_p is comparatively small, the sample boundary looks very smooth as it remains almost liquid-like and no change in surface intensity is observed (image(i)). Under subsequent perturbation, when the σ_p in the system attains a significantly higher peak, we observe the change in sample surface intensity due to the mechanism called dilation where the particles protrude out from the liquid-air interface (image (ii)). On further perturbation, many bright spots start appearing in addition to the dilation (image(iii)). As described in Chapter 3, it is known that such bright spots in this system are the localized plasticity formed due to high stress in the system and reflect the solid-like property of the system. Thus the appearance of these microscopic plasticities indicates the transition of system response from liquid-like to brittle solid-like under unidirectional repetitive perturbations. Similarly, in Figure 4.4, panel (b) represents a typical stress evolution under alternative reverse direction perturbation, and the sample boundary images, shown on the right (bottom panel), correspond to the peak stress for three different steps as marked in the plot. This indicates that although the system gives a solid-like response at the first step, indicated by the appearance of microscopic plasticity (image(i)), the alternative reverse direction perturbation can change the system response where only dilation is observed without plasticity (image(ii)) and eventually, the system gives a liquid-like response, as shown in the image (iii). Thus the change in the nature of the sample boundary surface in association with the corresponding rheological signature indicates that the transformation of the sample response due to encoded memory is intricately linked to the reorganization in the bulk sample.

Using a stress-controlled measurement protocol we further investigate such structural memory aspects of the SJ system. As shown in Figure 4.5(a), a constant shear stress is applied to the system for $1sec$, during which the shear strain is measured. The system is then allowed to relax for 30 seconds. Following this, the system undergoes multiple step-strain perturbations of a specific strain magnitude, which serves as a training protocol. After this training, the system is again subjected to the same constant shear stress for the same duration as prior to the training. It is observed that, under identical conditions, the shear strain developed in the system is higher for the untrained sample, compared to a trained sample (Figure 4.5(b)). This indicates that although the system remains at

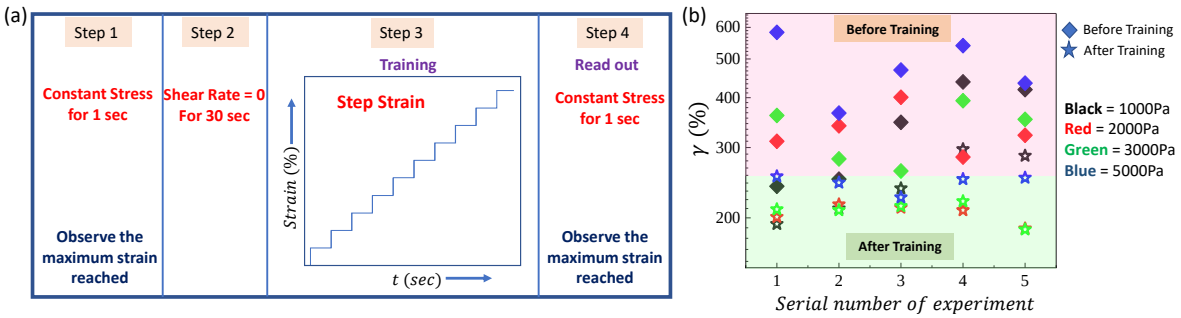

Figure 4.5: (a) Experimental protocol to study the directional memory in the dense particulate suspension using stress-controlled measurement. Here the strain evolution in the system is observed at constant stress for $1s$ before and after the repetitive step strain perturbation. (b) The maximum strain reached before and after the repetitive step strain perturbation is shown for 5 independent measurements at 4 different stress values, represented by different colors as shown in the legend. For a particular applied stress value the maximum strain reached before and after the step strain perturbation is presented by square and star respectively (represented by the same color).

zero stress conditions before and after the imposed training, the unidirectional repetitive step strain perturbation optimize the particle rearrangement such that it can resist more stress without much deformation.

To understand the microscopic mechanism giving rise to such an interesting memory effect we explore the response of the system in the reverse shear direction after the different number of training steps in the forward direction. Figure 4.6(a) represents the experimental protocol to study the reverse direction response. As shown in the figure, we apply a certain number of step strain perturbations in the forward direction (N_f), and then a significant number of steps are applied in the reverse direction (N_r) to get a good estimation of the saturation of the σ_p. Here we vary the N_f from 0 to 40 and for each N_f, we apply 100 steps in reverse direction ($N_r = 100$). In Figure 4.6(b) we have shown the σ_p evolution during the reverse run for two cases. (1) Without any forward steps ($N_f = 0$), (2) After 20 forward steps ($N_f = 20$). From Figure 4.6(b) we can observe that for $N_f = 0$ the σ_p attains saturation in comparatively more number of steps than the $N_f = 20$ case. Here the negative sign of the σ_p indicates the fact that the step strain is in the reverse direction and the saturation point is marked where the magnitude of the σ_p starts decreasing from its previous value. The corresponding step number is considered the saturation step number (N_s) (Figure 4.6(b)). These reversal experiments highlight the fact that, if the system is trained with more steps in one direction, then it requires comparatively less number of steps to attain saturation in σ_p in the opposite direction (Figure 4.6(c)). Our

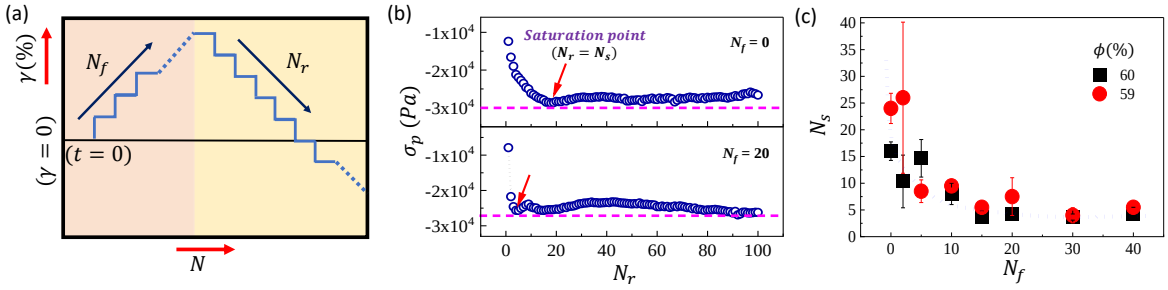

Figure 4.6: (a) Carton of an experimental protocol showing a certain number of step strain (N_f) applied in the forward direction and then a significant number of step strains (N_r) are applied in the reverse direction. Both time t and γ are 0 at the beginning and the magnitude of the step strain always remains constant. (b) Variation of peak stress σ_p with N_r for N_f=0 (top panel) and N_r=20 (bottom panel). The saturation of σ_p is indicated by the horizontal dashed lines and the saturation step number (N_s) is marked by red arrows. (c) Variation of saturation step number in reverse direction N_s with number of training steps in the forward direction N_f for the volume fraction ϕ as indicated in the legend.

repetitive step-strain experiments and the shear-reversal experiments suggest that due to the forward training of the sample, there are residual contacts or structure formation that remain even after the stress relaxes to zero. Such structures enable the formation of system-spanning contacts during the shear reversal, more easily.

To test our conjecture about the formation of such residual contacts or structures, we use numerical simulation (in collaboration with Dr. Vinutha H. A. from Georgetown University, USA). We consider an SJ dense particulate system in 2-D, having a packing fraction of 0.81 which is well above the minimum shear jamming packing fraction in 2-D. The system is driven into the SJ state by applying a strain of 0.121, and then repetitive step strain perturbations of step size 0.00186 are applied to observe the structural evolution. It is to be noted that we do not consider hydrodynamics in our simulation and only observe the shear-induced evolution of the particle configuration in the shear-jammed state. Here, the rigid clusters are defined based on Maxwell's criterion where the number of constraints should equal the degrees of freedom of the structure. This condition is known as the isostatic condition. When the number of constraints becomes more than the net degrees of freedom then the system is considered as over-constrained which can be sustained under stress. Figure 4.7(a) shows two different structures where the 3-particle structure represents an isostatic configuration and the 4-particle structure represents an over-constraint configuration. From this simulation, we observe that the fraction of particles associated with the rigid cluster formation (f_{RC}) and the average size

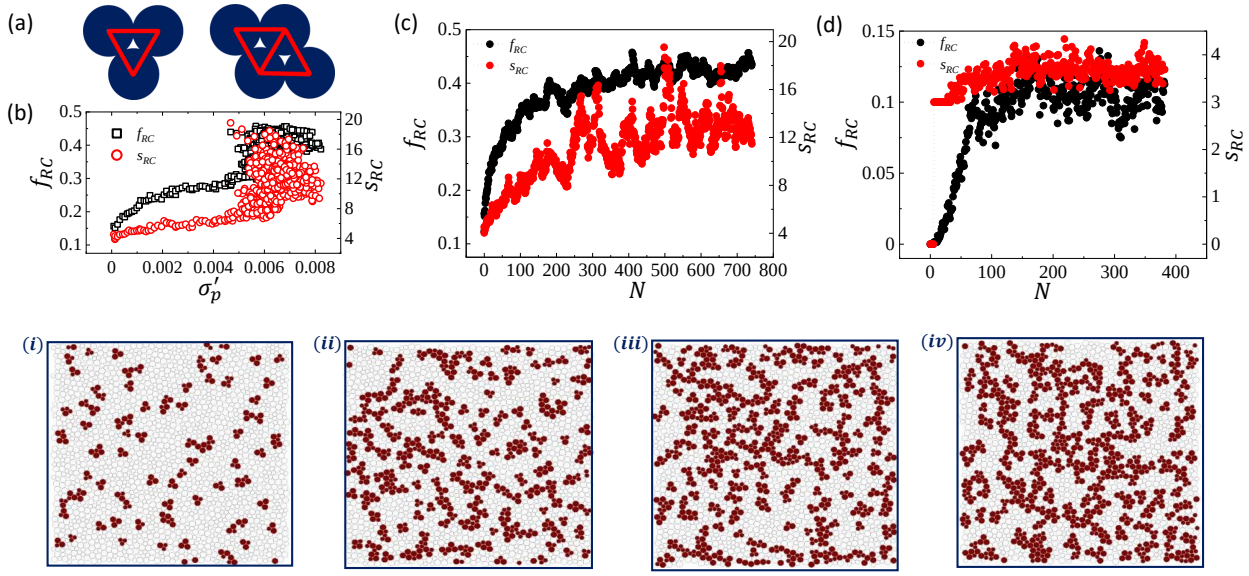

Figure 4.7: (a) Cartoon of isostatic and over-constrained structures represented by three and four-particle structure respectively. Fraction of particles associated with the formation of the rigid clusters (f_{RC})(Black symbols) and the average size of rigid clusters (s_{RC}) (Red symbols) as a function of (b) shear stress $\sigma_p^{'}$, (c) step number N for a 2D shear jammed system with packing fraction 0.81. (d) f_{RC} and s_{RC} with step number N for a system with packing fraction 0.79 which can not show shear jamming. In bottom panel snapshots (i), (ii), (iii), and (iv) represent the rigid clusters (marked in red) corresponding to step numbers 1, 60, 184, and 496 respectively, for the shear jammed system shown in (c).

of the rigid clusters (s_{RC}) increases significantly with the increase of stress in the system (Figure 4.7(b)). Again, as shown by Figure 4.7(c), both f_{RC} and s_{RC} shows a systematic increase with step number N. In the bottom panel, images (i), (ii), (iii), and (iv) represent the rigid cluster snapshots at step number 1, 60, 184, and 496, respectively, where these snapshots also reflect the growth of the average size and fraction of the rigid cluster. From Figure 4.7(c), we observe that although the minimum rigid cluster size (number of particles required for the rigid cluster formation) is 3, the repetitive shear perturbation can cause significant growth in s_{RC} which can span the whole system. Interestingly where the f_{RC} for the higher packing fraction (above the minimum SJ packing fraction) can grow around 45% of the total particles, and for the lower packing fraction, below the minimum SJ packing fraction, there is no significant growth in f_{RC}. In this case, f_{RC} remains around 10%, and the average size of the cluster s_{RC} does not grow much beyond the minimum value 3 (Figure 4.7(d)).

A recent study demonstrates a rigidity percolation transition governed by Ising universality—with critical exponents $\beta = 1/8$ and $\gamma = 7/4$—in dense 2D suspensions subjected to shear stress well above the DST threshold [13]. The authors interpret the sharp increase in the fraction of rigid clusters and the divergence in the associated susceptibility as signatures of a critical point preceding shear jamming. However, we did not observe any evidence of structural memory for the volume fraction that shows DST but not shear jamming. It is possible that the formation and persistence of rigid clusters require sustained, high-magnitude shear stress, which transient perturbations may not provide.

Furthermore, to get a deeper insight into the microscopic mechanism, we follow the shear reversal protocol similar to our experiment as shown in Figure 4.6(a). Here we apply a certain number of steps in the forward direction (N_f) and then change the direction of the shear and apply a significantly large number of step strain perturbations in the reverse direction (N_r). Figure 4.8(a) shows the variation of f_{RC} with N_r during reversal from different forward steps (N_f) in training, as mentioned in the legend. Here we observe that the application of step strain in the reverse direction initially decreases the f_{RC} and then increases it back to the higher saturating value. Similarly, Figures 4.8(b) and 4.8(c) indicate the variation of s_{RC} and Z respectively during reversal, which also shows a similar trend. These results indicate that the extent of decrease in f_{RC}, s_{RC} and Z strongly depends on the number of applied forward steps before reversal. Now we consider two different configurations before applying the shear perturbation in the reverse direction: (1) at the initial training step ($N_f = 1$), when there is a very less number of rigid clusters present, and (2) after a large number of training steps ($N_f = 185$), when a large number

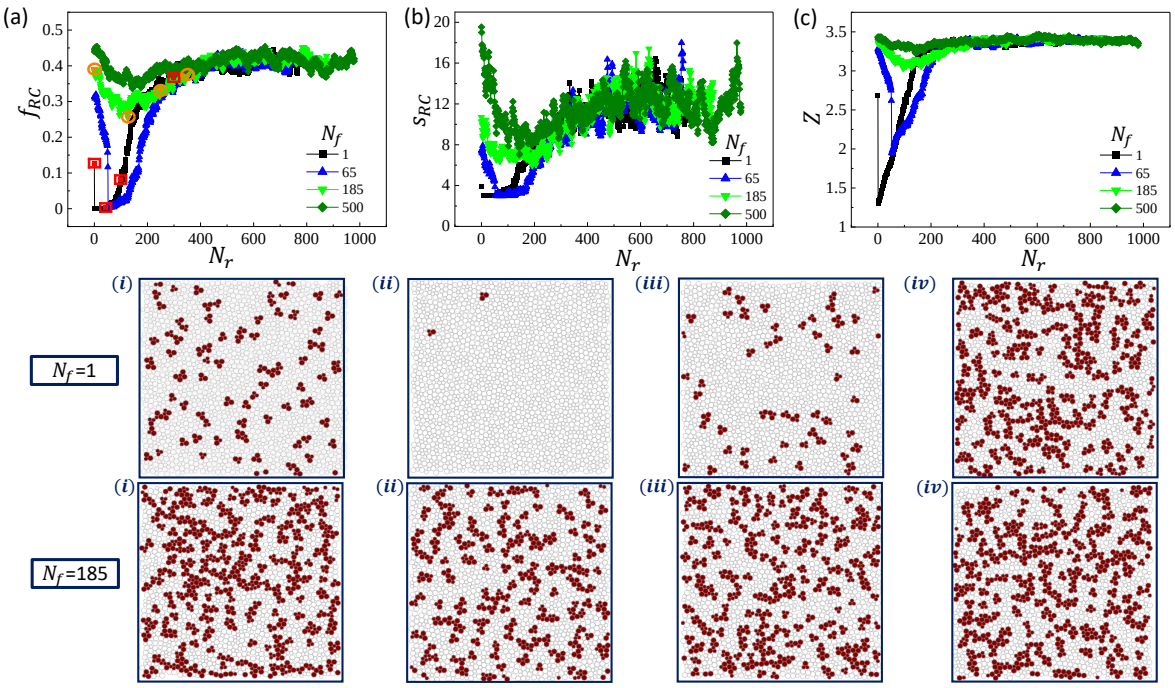

Figure 4.8: (a) The fraction of particles forming rigid clusters f_{RC}, (b) the average size of the rigid cluster s_{RC}, (c) the average coordination number (Z) as a function of number of steps in reverse direction N_r after reversal from different numbers of forward steps (N_f) as mentioned in the legends. The bottom panel shows the rigid cluster snapshots during the reverse perturbation for the case N_f=1 and N_f=185. For N_f=1, the images (i), (ii), (iii), and (iv) correspond to N_r = 0, 45, 100, and 300 respectively as marked by red squares in (a) and for N_f=185, the images (i), (ii), (iii), and (iv) correspond to N_r = 0, 130, 250, and 350 respectively as marked by orange circles in (a).

of rigid clusters are formed. In the bottom panel, we have shown the snapshots of rigid clusters for a minimally trained system ($N_f = 1$) and a well-trained system ($N_f = 185$) at different N_r. We observe that when there are less numbers of rigid clusters present, the continuous shear in the opposite direction initially destroys most of the existing clusters and then starts forming new rigid clusters from the minimum possible size to the clusters with a large number of particles (images corresponds to $N_f = 1$). Interestingly, when we start with a configuration having a large fraction of rigid clusters, the continuous shear in the opposite direction can not destroy the fraction of rigid clusters significantly (images corresponds to $N_f = 185$). In this case, although the rigid clusters rearrange among themselves, the average size, and the fraction of rigid clusters do not decrease much (Figure 4.8(a),(b)). This is also reflected in the variation of the corresponding coordination number Z where the decrease in Z significantly depends upon the training in the forward direction. This indicates that, as also predicted from our experimental observation, the characteristic of the shear-jammed state is sensitive to the initial perturbation it has gone through implying a structural memory effect.

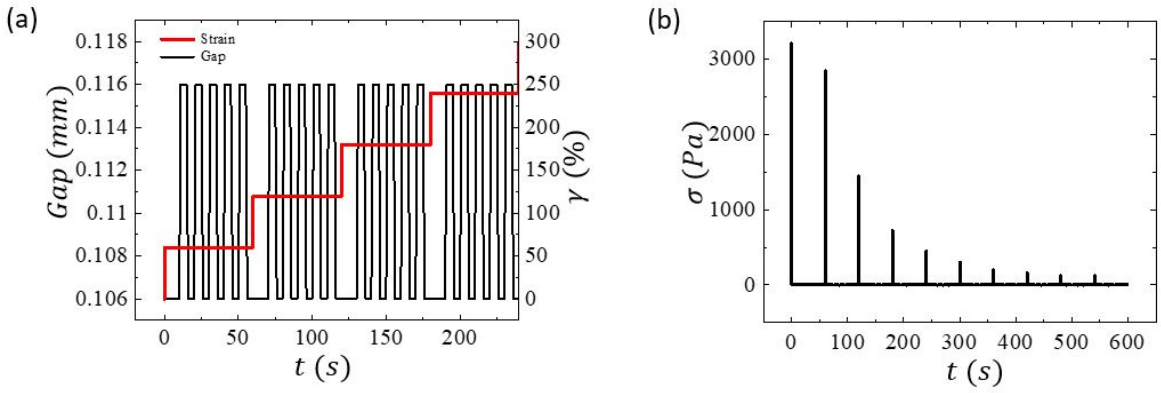

Figure 4.9: (a) Protocol to erase the structural memory formed during step strain perturbation. The red solid line represents the applied step strain of magnitude 60% and the black solid line represents the gap between the plates which oscillates between 0.106 mm to 0.116 mm keeping the shear strain fixed at a constant value. The time interval between two consecutive step strains is 60 s. For clarity, we only show up to 4 step-strain perturbations. (b) Stress response corresponds to the step strain input shown in (a).

We further explore the possible options to destroy the structural memory formed due to unidirectional step-strain perturbation. We observe that the application of the small amplitude ($< 5\%$) oscillatory perturbation of different frequencies in the shear direction can not destroy such structural memory. So, we investigate the effect of orthogonal

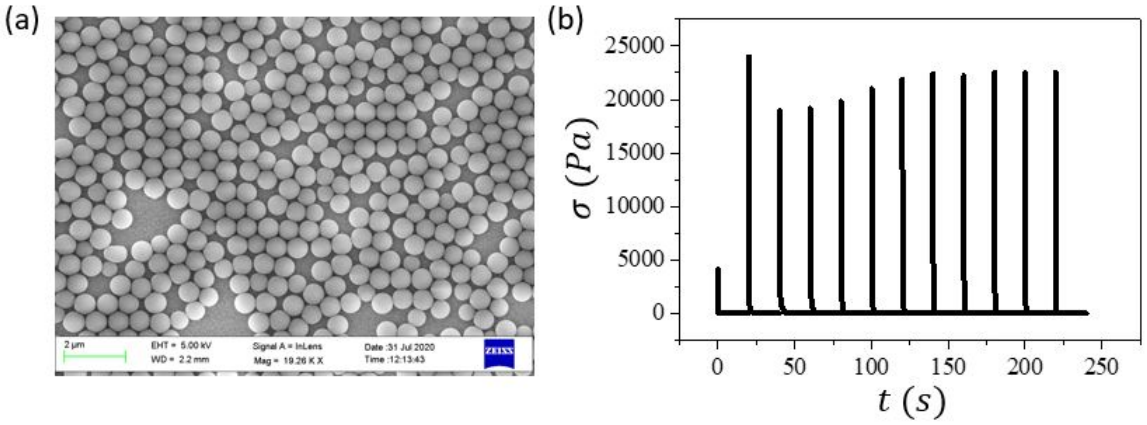

Figure 4.10: (a) SEM image of nano-polystyrene particles used for rheological experiment. (b) Stress response under unidirectional repetitive step strain perturbation of step magnitude 50% for dense suspension of nano polystyrene particles ($d \approx 700\ nm$) with volume fraction 59%.

perturbation over such structural memory. As shown in Figure 4.9(a), after each step of shear perturbation, we increase the gap between the plates by $10\mu m$ and then bring it back to the original measuring position. It corresponds to a very small extensional strain of $\epsilon = \frac{10\mu m}{MinGap}$. We repeat this process 5 times under a constant shear strain condition and then apply the next step of shear perturbation. Figure 4.9(b) represents the stress response corresponding to the input protocol shown in Figure 4.9(a). From Figure 4.9(b), we find that although we apply a series of step shear-strain perturbations in the same direction, the peak stress in the system does not increase. From this observation, we understand that the small extensional shear experienced by the system due to the repetitive change of gap can disturb the structure of particle arrangement formed by the step shear strain, which in turn does not allow the systematic increase in peak stress. Again, we find that such memory effect is not very conclusive for smaller-size particles (Figure 4.10). Although the volume fraction of the system is high enough, still this might be due to the significant effect of Brownian motion in the system.

4.4 Conclusion

In conclusion we study a novel memory effect in the SJ dense suspensions. We observe that although the fast relaxation of shear stress changes the mechanical property of the system significantly, the structural arrangement of the particles still remembers the previous

perturbation. Under the unidirectional repetitive step strain perturbation there is an enhancement of mechanical response even after the complete stress relaxation by orders of magnitude stress after each step. Interestingly, under the step strain perturbation in the alternative direction, the mechanical response becomes gradually weaker. Using in-situ boundary imaging, we confirm such evolution in the system response from liquid-like to brittle solid-like state under repetitive perturbation. We further find that this structural memory is significant only for the volume fractions above the minimum volume fraction required for the shear jamming which establishes a direct connection between structural memory and shear jamming phenomena. Such memory effect is not observed for volume fraction below shear jamming. Using a shear reversal experiment and numerical simulation we explore the possible microscopic mechanism for such structural memory. We find that the formation of shear-induced rigid clusters plays a crucial role in controlling such memory effect. Furthermore, we show that the orthogonal perturbation can effectively destroy the structural memory in the system. Although we observe that such memory effect is not significant for smaller size particles, the effect of Brownian motion in highly dense environments and generalization of such phenomena needs to be explored further in the future. Also, incorporating hydrodynamics in our simulation will be important to capture the fast stress relaxation in the system, and the associated memory formation remains to be an interesting future direction.

Bibliography

[1] A.J. Liu and S.R. Nagel. *Jamming and Rheology: Constrained Dynamics on Microscopic and Macroscopic Scales*. CRC Press, London, 2001.

[2] Andrea J Liu and Sidney R Nagel. Jamming is not just cool any more. *Nature*, 396(6706):21–22, 1998.

[3] ME Cates, JP Wittmer, J-P Bouchaud, and Ph Claudin. Jamming, force chains, and fragile matter. *Physical review letters*, 81(9):1841, 1998.

[4] Veronique Trappe, V Prasad, Luca Cipelletti, PN Segre, and David A Weitz. Jamming phase diagram for attractive particles. *Nature*, 411(6839):772–775, 2001.

[5] Sachidananda Barik and Sayantan Majumdar. Origin of two distinct stress relaxation regimes in shear jammed dense suspensions. *Phys. Rev. Lett.*, 128:258002, Jun 2022.

[6] Rijan Maharjan and Eric Brown. Giant deviation of a relaxation time from generalized newtonian theory in discontinuous shear thickening suspensions. *Physical Review Fluids*, 2(12):123301, 2017.

[7] Saisai Cao, Qianyun He, Haoming Pang, Kaihui Chen, Wanquan Jiang, and Xinglong Gong. Stress relaxation in the transition from shear thinning to shear jamming in shear thickening fluid. *Smart Materials and Structures*, 27(8):085013, 2018.

[8] Vikram Rathee, Daniel L Blair, and Jeffrey S Urbach. Dynamics and memory of boundary stresses in discontinuous shear thickening suspensions during oscillatory shear. *Soft Matter*, 17(5):1337–1345, 2021.

[9] Edward YX Ong, Meera Ramaswamy, Ran Niu, Neil YC Lin, Abhishek Shetty, Roseanna N Zia, Gareth H McKinley, and Itai Cohen. Stress decomposition in laos of dense colloidal suspensions. *Journal of Rheology*, 64(2):343–351, 2020.

[10] Hojin Kim, Aaron P Esser-Kahn, Stuart J Rowan, and Heinrich M Jaeger. Stress-activated friction in sheared suspensions probed with piezoelectric nanoparticles. *Proceedings of the National Academy of Sciences*, 120(49):e2310088120, 2023.

[11] Endao Han, Matthieu Wyart, Ivo R. Peters, and Heinrich M. Jaeger. Shear fronts in shear-thickening suspensions. *Phys. Rev. Fluids*, 3:073301, Jul 2018.

[12] Edward Y. X. Ong, Anna R. Barth, Navneet Singh, Meera Ramaswamy, Abhishek Shetty, Bulbul Chakraborty, James P. Sethna, and Itai Cohen. Jamming memory into acoustically trained dense suspensions under shear. *Phys. Rev. X*, 14:021027, May 2024.

[13] Aritra Santra, Michel Orsi, Bulbul Chakraborty, and Jeffrey F Morris. Rigid clusters in shear-thickening suspensions: a nonequilibrium critical transition. *Physical review research*, 7(1):013275, 2025.

CHAPTER

FIVE

Shear thickening of dilute suspensions of fractal silica aggregates

"In the history of science, we often find that the study of some natural phenomenon has been the starting point in the development of a new branch of knowledge."

- C. V. Raman -

The results covered in this chapter are published in the article, Journal of Non-Newtonian Fluid Mechanics, vol. 328, June 2024 [1].

5.1 Introduction

In the past few decades, as discussed before, the phenomena of shear thickening and shear jamming have attracted considerable attention due to their enriching fundamental physics and promising engineering applications [2, 3, 4, 5, 6, 7]. As a considerably high volume fraction is a primary requirement for the observation of strong ST, from an application perspective, this prerequisite poses a significant challenge regarding the cost-effectiveness and stability of the suspension. Fumed silica (FS) particles - irreversible fractal aggregates of nano-silica particles [8], turn out to be a reliable alternative to address these concerns [9]. Recent literature has explored various aspects of ST in FS suspension, where strong ST has been reported for significantly low volume fractions. The effect of particle size distribution [10, 11], surface chemistry [12, 13], and solvent properties [14, 11] have been explored in these systems. Additionally, the signature of hydro-cluster formation during ST [15] and the nature of jamming front propagation have also been investigated [16]. Interestingly, a recent work observed that for hydrophilic FS suspension, the minimum stress required for ST (onset stress) increases with increasing the particle volume fraction (ϕ) [13], unlike the non-fractal ST systems where the onset stress (σ_{onset}) remains independent of ϕ [17, 18, 19, 20]. Additionally, the increase in the onset stress was associated with increased roughness of the FS particles, where the roughness was defined on the basis of primary constituent particle diameter (d_p) forming the fractal aggregates [13]. However, systematic roughness variation in non-fractal systems shows an opposite trend, namely a decrease in onset stress with increasing particle roughness [21]. All these observations suggest that roughness may not be the only governing parameter in explaining the complex ST behavior in FS systems.

In this chapter, we systematically study the shear thickening properties of fumed silica suspensions using six different grades of hydrophilic FS particles having different structural properties. We observe an exponential increase in the onset stress with increasing ϕ where the exponent depends on the specific type of the FS. Interestingly, for a few types of the FS systems, we see a reversible weakening of the ST response at higher stress values. Such weakening is also sensitive to the volume fraction. We map out a detailed ST phase diagram in the $\sigma - \phi$ plane for two types of FS systems. Using rheology and in-situ boundary imaging experiments, we bring out the role of the structural parameters, such

as fractality and internal branching of the FS aggregates in controlling the ST properties in these systems.

5.2 Materials and Methods

Hydrophilic Aerosil fumed silica (FS) of six different grades (OX50, A90, A150, A200, A300, A380) from Evonik Industries are used for the preparation of dense particulate suspensions with glycerol as the solvent (The sample preparation procedure is described in Chapter 2). These FS particles are formed using a flame aerosol synthesis process where small primary particles are fused together to form hard fractal aggregates which further agglomerate to form soft deformable objects [22, 23, 8]. The name of each FS type is based on their corresponding specific surface area (surface to mass ratio), varying from $50m^2/g$ to $380m^2/g$ depending on the primary constituent particle size (d_p) [8].

All the rheological measurements are performed using a stress-controlled rheometer (MCR-702, Anton Paar, Austria) with cone and plate geometry of a radius of 12.5 mm and cone angle of 2°. A pre-shear at constant stress (above onset stress for ST) is applied for a certain amount of time ($\approx 60 minutes$) to remove any loading history.

For in-situ boundary imaging during flow curve measurements, a high-speed imaging setup is coupled with the rheometer operating in a 50-50 counter movement mode. As the FS suspension in glycerol is optically transparent, the suspension is seeded with polystyrene microspheres of diameter ~ 3 μm for obtaining a clear speckle pattern. The amount of the polystyrene sphere added is $\sim 1\%$ of the solvent weight. We have verified that such a small amount of tracer particles does not alter the rheological properties of the FS system. During the rheological measurements, the sample boundary is illuminated by an LED light source (Dolan-Jenner Industries), and the diffused scattering is imaged in the flow gradient plane using a high-speed monochrome CMOS camera (Phantom Miro C210) with a 10X, long working distance objective (Mitutoyo). All the images are captured at a frame rate of 100 Hz with resolution 1280×1024 pixels. From the sample boundary image, we map out the flow profile through the Particle Image Velocimetry (PIV) technique using a custom-written PIV code developed using MATLAB software.

5.3 Results and Discussion

We study the shear thickening (ST) behavior for six different types of fumed silica (FS) samples. For each type of sample, we obtain the flow curves (viscosity (η) vs. applied

stress(σ)) for a wide range of volume fractions (ϕ): starting from the minimum value of ϕ required for the ST, up to the maximum ϕ value beyond which the sample mixing becomes extremely difficult. Figures 5.1(a) and 5.1(b) represent the flow curves for OX50 and

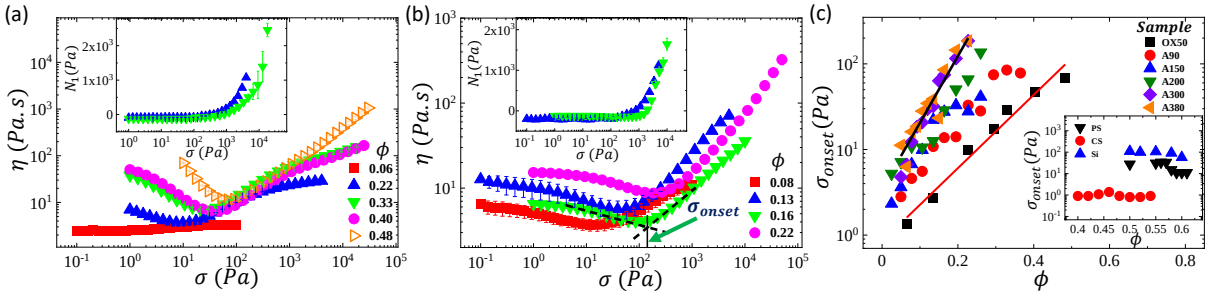

Figure 5.1: Viscosity η as a function of shear stress σ for fumed silica sample OX50 (a) and A380 (b) for various volume fraction ϕ as shown in the legend. Variation of first normal stress difference N_1 with σ is shown for $\phi = 0.22$ and 0.33 in the inset of (a) and $\phi = 0.13$ and 0.16 in the inset of (b). The onset stress σ_{onset} of shear thickening is marked for $\phi = 0.16$ in (b). (c) Variation of σ_{onset} with ϕ for different fumed silica sample as shown in the legend. The slope indicated by red and black solid lines represent the difference in rate of exponential increase in σ_{onset} with ϕ for OX50 and A380 sample respectively. Inset represent the σ_{onset} variation with ϕ for three standard shear thickening systems; polystyrene sphere (PS), cornstarch (CS), silica sphere (Si) as shown in legend.

A380 respectively. Flow curves for all other samples are shown in Figure 5.2. We observe that the minimum value of ϕ required for ST (ϕ_{min}) is ≈ 0.05. This value is significantly lower compared to the standard non-fractal ST systems [24, 17, 18]. In all cases, we obtain strong ST over a wide range of ϕ values, as shown in Figures 5.1(a), 5.1(b), and Figure 5.2. The maximum value of ϕ ($\phi = \phi_{max}$), which we can mix uniformly, varies for different types of FS used. The ϕ_{max} decreases significantly as we go from OX50 to the A380 sample (Figure 5.3(a)). We find that, unlike standard ST systems, the range of ϕ showing ST (ϕ_{range}) is significantly broad for the FS system and the range decreases significantly as we go from OX50 to the A380 sample (Figure 5.3(b)). Furthermore, in the ST regime, the 1st normal stress difference N_1 is positive, as expected for discontinuous shear thickening, for all the FS samples (inset of Figures 5.1(a), 5.1(b) and 5.2). This indicates that the frictional contacts between the FS particles are responsible for the ST [24]. A notable feature of the ST in the FS systems is the ϕ-dependence of σ_{onset} which is determined from our data using a simple intersection of extrapolated shear thinning and shear thickening branches in $\eta - \sigma$ plots (see Figure 5.4(a)). Figure 5.1(c) shows that the onset stress σ_{onset} for ST increases exponentially with increasing ϕ, with the exponent

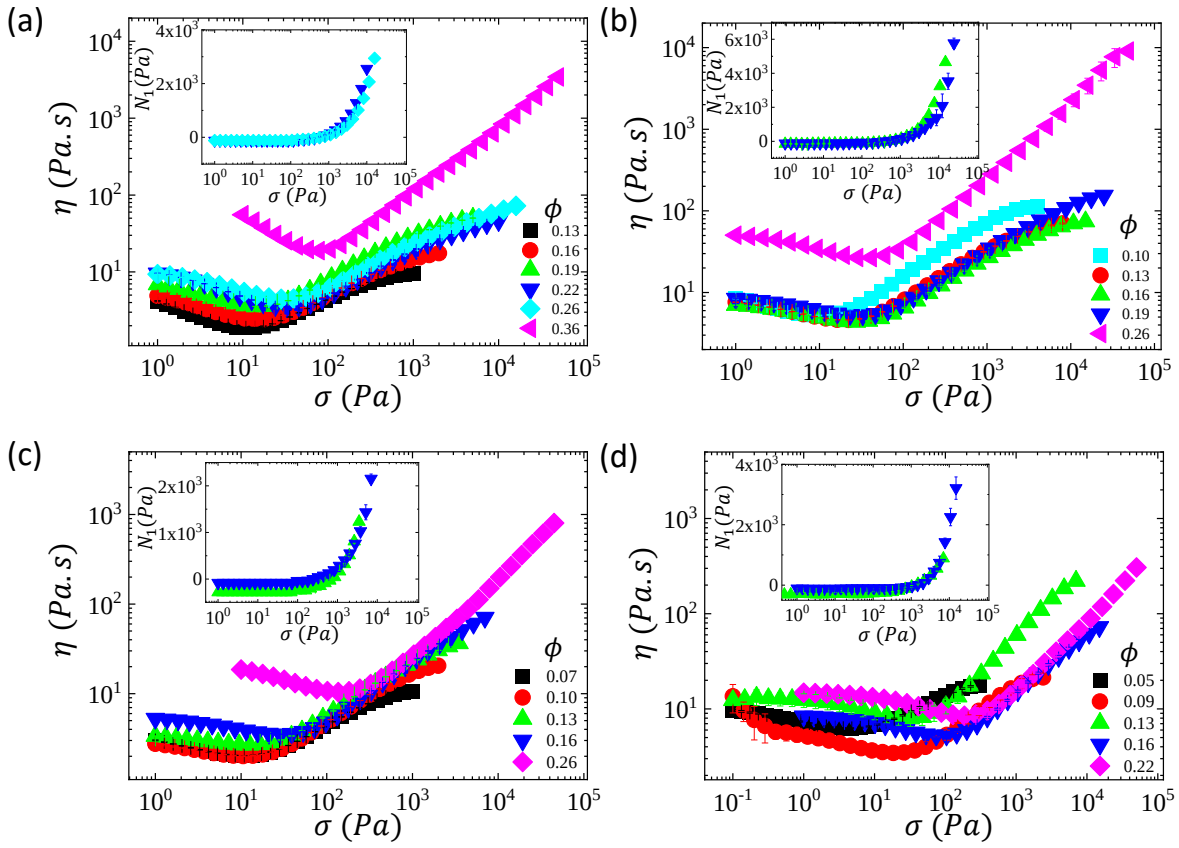

Figure 5.2: Viscosity η as a function of shear stress σ for fumed silica sample (a) A90, (b) A150, (c) A200 and (d) A300 for various volume fraction ϕ as shown in the legend. Inset of each panel show the corresponding variation of first normal stress difference N_1 with σ for only two ϕ as shown in legend.

depending on the type of FS used. This is in stark contrast to standard, non-fractal ST systems, such as dense suspension of polystyrene, silica, and cornstarch particles where the onset stress σ_{onset} remains almost constant with the volume fraction ϕ (inset of Figure 5.1(C)). This highlights that the existing theoretical framework, such as the empirical Krieger–Dougherty (KD) and Wyart-Cates (W-C) models will not be sufficient in capturing the ST behavior in the FS system [3, 18, 13].

In a recent study [13], the roughness of the FS system is related to the primary constituent particle size d_p (smaller d_p corresponds to larger roughness and vice versa). Following this line of thinking and using the value of d_p (Table 5.1) from the study by Mulderig et al.[8], for a constant ϕ, the σ_{onset} decreases with decreasing roughness (i.e increasing d_p) of the particles as shown in Figure 5.5(a).

Notably, this trend of σ_{onset} as a function of roughness is counter intuitive and oppo-

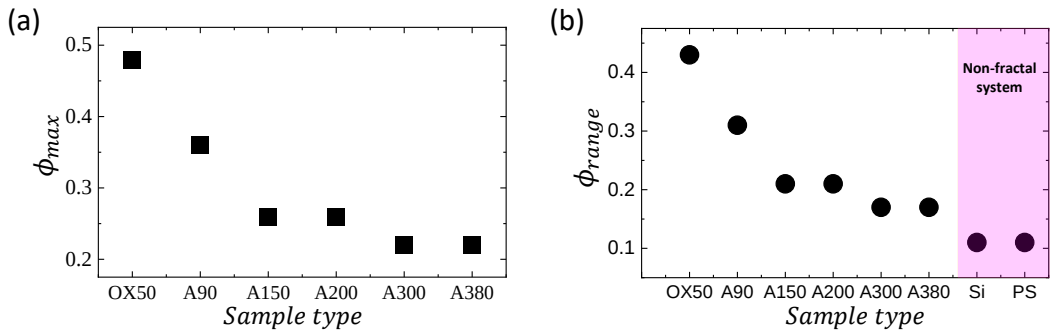

Figure 5.3: (a) Maximum possible volume fraction that we can mix (ϕ_{max}) for different types of fumed silica. (b) Volume fraction range showing shear thickening ($\phi_{range} = \phi_{max} - \phi_{min}$) for different types of fumed silica and two non-fractal standard shear thickening systems; silica sphere (Si) and polystyrene sphere (PS) suspension.

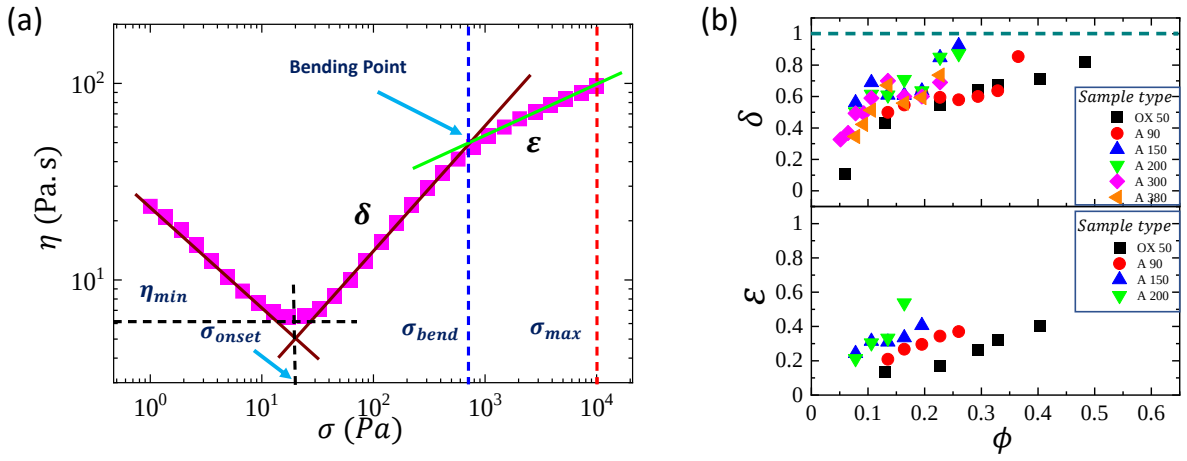

Figure 5.4: (a) Bending in flow curve during ST process. δ represents the initial slope for the shear thickening regime. In the shear thickening regime the slope δ decreases to ε at a crossover stress σ_{bend} indicated by the vertical blue dashed line. The vertical red dashed line indicates the σ_{max}, the maximum stress limit for ST before yielding. (b) Variation of slope δ and ε with ϕ for different types of fumed silica sample as shown in the legend. Increasing slope δ with ϕ indicates the transition from mild shear thickening to strong shear thickening with increasing ϕ. For a particular ϕ the slope δ decreases to ε after the bending point. This decrease in slope vanishes for ϕ close to ϕ_{max}. The decrease in slope is more prominent for high fractal systems like OX50 and A90 with a wide ϕ range. Sample A300 and A380 do not show any decrease in slope.

site to the trend seen in a recent study on a non-fractal silica particle system where a systematic increase in the particle roughness decreases the σ_{onset} [21]. Interestingly the

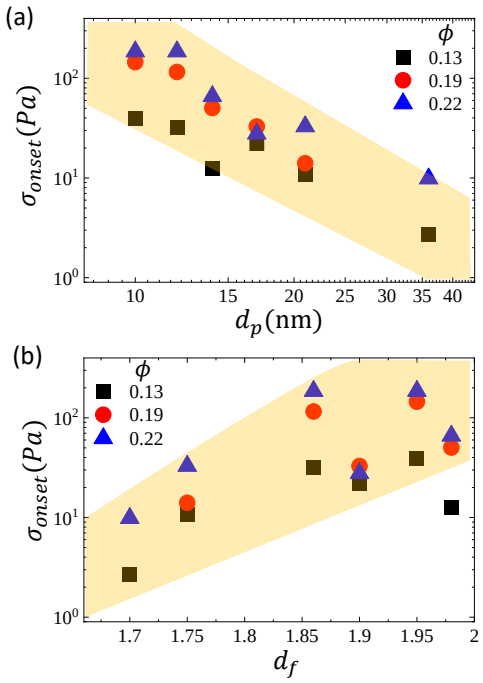

Figure 5.5: (a) σ_{onset} variation with primary constituent particle diameter (d_p) of different fumed silica sample for three different ϕ as shown in the legend. (b) Variation of σ_{onset} with mass fractal dimension (d_f) of different fumed silica samples for three different ϕ as shown in the legend. The shaded regions in (a) and (b) are the guides to the eye.

σ_{onset} increases with the increase in the 3-d mass fractal dimension (d_f) of the system, as shown in Figure 5.5(b). This suggests that the fractality and the complex internal structures of the fumed silica can play a crucial role in controlling the ST properties.

Furthermore, we observe stress-softening response during shear-thickening for certain types of FS systems. In general, for any standard ST sample, the typical flow curve can be divided into three parts as a function of increasing applied stress: (1) an initial shear-thinning regime (2) a shear-thickening regime beyond the σ_{onset} and (3) decrease in viscosity at stress values much higher than σ_{onset} due to plasticity/stress-induced fracture (sometimes referred [25] as the second shear-thinning regime). Region 3, in such cases, is irreversible in nature and involves large dissipation. The power-law slope of Region 2 indicates the degree of ST [19, 17]. In our case, we observe that the power-law slope in the ST regime is not constant for all values of $\sigma > \sigma_{onset}$ but decreases to a smaller value beyond a certain applied stress (defined as the bending point stress σ_{bend}) much below yielding (Figure 5.6(a)). It is important to note that such a decrease in the ST slope is reversible in nature as shown in Figure 5.7(a) which rules out plasticity/stress-induced

Sample	OX50	A90	A150	A200	A300	A380
Primary particle diameter ($d_p(nm)$)	36	21	17	14	12	10
Mass fractal dimension (d_f)	1.70	1.75	1.90	1.98	1.86	1.95
Number of internal branching (n_i)	11	15	56	93	373	3125

Table 5.1: Important parameters controlling the ST behavior as obtained from [8].

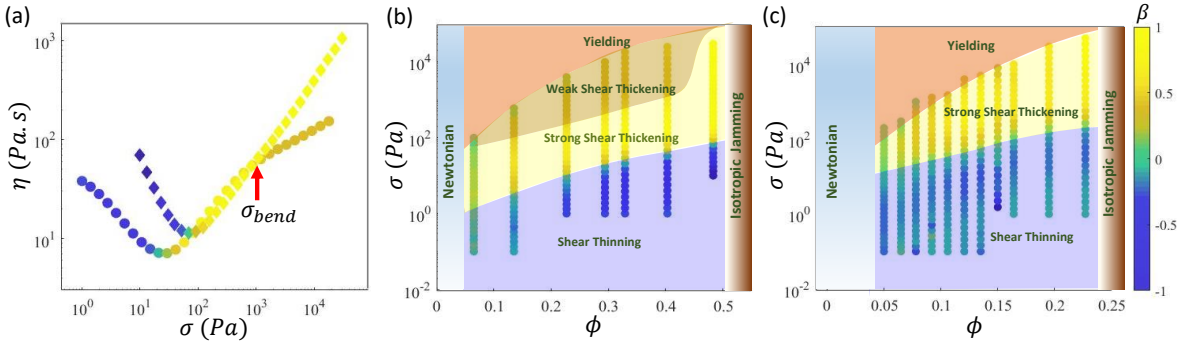

Figure 5.6: (a) Flow curves of OX50 sample at $\phi = 0.33$ (circle) and $\phi = 0.48$ (diamond) is shown. For $\phi = 0.33$ (circle) the change in slope during the shear thickening process is highlighted. The bending point is indicated by the red arrow and the corresponding stress is σ_{bend}. The colors of the symbol represent the local slope $\beta = d\ln(\eta)/d\ln(\sigma)$ as shown by the color bar. (b) and (c) represent the phase diagram for OX50 and A380 samples in σ vs ϕ plane. Differently, shaded regions represent different properties of the system as mentioned, depending on the corresponding β value indicated by the color bar.

fracture. We find that this change in slope in the ST regime decreases with increasing ϕ and is absent close to ϕ_{max} (Figure 5.7(b)). We label the initial ST regime with a higher slope (just beyond σ_{onset}) as the strong shear-thickening regime and the second ST regime obtained at higher applied stresses with a lower slope as the weak shear-thickening regime. Figure 5.6(b) shows the phase diagram of the OX50 sample in the $\sigma-\phi$ plane. Here we can see that after the initial shear-thinning region at smaller stress, a strong shear-thickening regime starts, and in between the strong shear-thickening and the yielding regime, there is a weak shear-thickening region. We also see from Figure 5.6(b) that the width of the weak shear-thickening region depends on ϕ. The boundary between the shear thinning and strong ST regime represents σ_{onset} and the boundary between strong ST and weak ST regime is marked by σ_{bend}. As we systematically increase the specific surface area of the sample used (starting from OX50 towards the A380 sample), such a difference between the ST slopes gradually decreases and vanishes completely for A300 and A380 samples (Figure 5.4). Figure 5.6(c) represents a similar phase diagram for the A380 sample, where

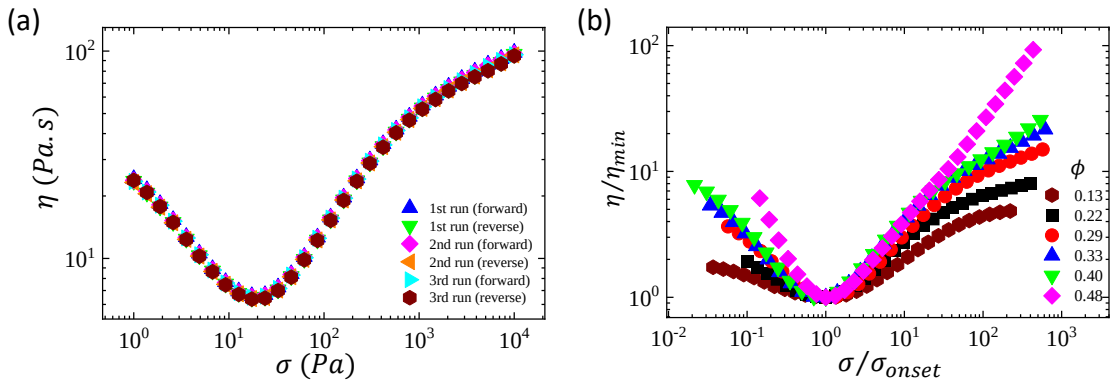

Figure 5.7: (a) Viscosity η as a function of shear stress σ for OX50 fumed silica sample at $\phi = 0.29$. Both forward and reverse runs for three consecutive readings are shown. (b) Variation of normalized viscosity (viscosity normalized by minimum viscosity) with normalized shear stress (shear stress normalized by onset stress) for OX50 at different ϕ as shown in legend. This exhibits the evolution of bending in shear thickening flow curves with increasing volume fraction.

the weak ST regime does not exist. The color of the symbols represents the local slope $(d\ln(\eta)/d\ln(\sigma))$ as indicated by the parameter β.

In order to understand the novel rheological behaviors of fumed silica suspensions, we now focus on the structural differences between the different types of FS systems used. A comprehensive study of the structural properties of all these six hydrophilic FS samples has been reported [8] using ultra-small angle X-ray scattering and numerical simulations. A few of the relevant parameters are given in Table 5.1. As mentioned earlier, since the ST is frictional contact dominated, we mainly focus on the internal branching of the FS clusters which is expected to affect the nature of contact formation between them. It is reported that although all these FS samples are fractal in nature, the internal branching differs significantly across the sample types. As we go from OX50 to A380, in addition to the decrease in d_p, the number of internal branching (n_i) increases significantly, thereby making the structure more compact. The structure of the OX50 sample is more open due to less number of internal branching, whereas, the A380 sample structure is more closed due to a large number of internal branching. We have verified such structural differences using SEM for two extreme cases (OX50 and A380) as shown in Figure 5.8(a). These images also highlight the significant difference in primary particle diameter (d_p) and fractality depending on the sample type. For clarity, we also depict these structures using cartoons in Figure 5.8(b). For a dense FS suspension with clusters having an

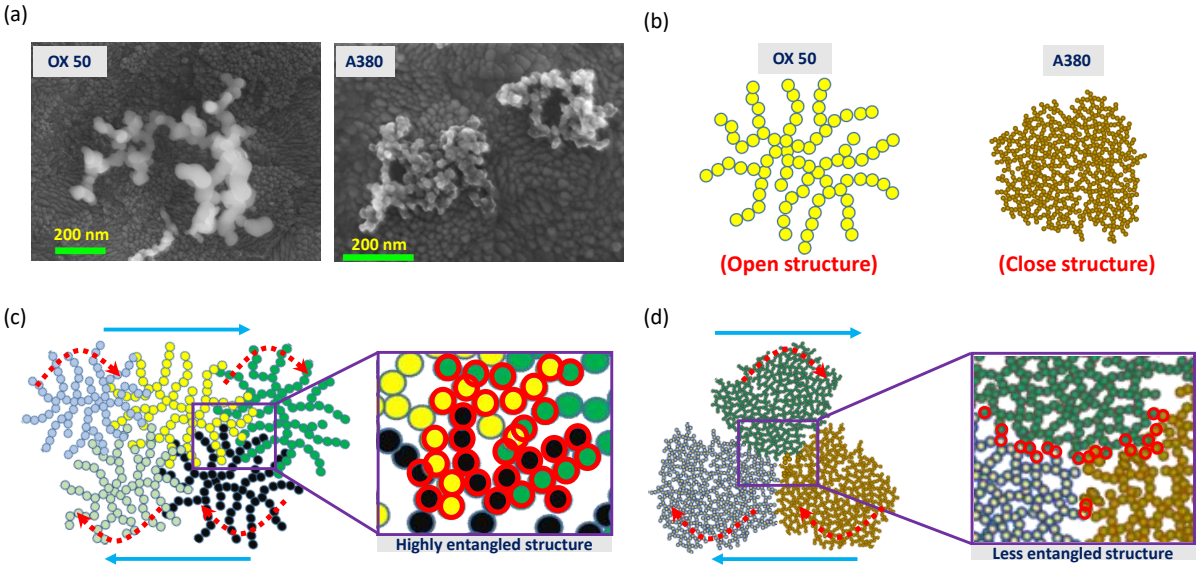

Figure 5.8: (a) SEM image of OX50 and A380 aggregates reflect the wide difference in their primary constituent particle diameter d_p, mass fractal dimension d_f and internal branching structure of the samples. (b) Cartoon representations of OX50 and A380 aggregates reflect the open and closed structure respectively. (c) Cartoon representation of high constraints on the aggregates motion under shear for open structured sample (OX50) due to more entanglement. The zoomed-in part represents the highly entangled structure and a larger number of interparticle contact points between aggregates (red circles). (d) Cartoon representation of fewer constraints on aggregate motion under shear for close structured sample (A380) due to less entanglement. The zoomed-in part represents the less entangled structure and a smaller number of interparticle contact points between aggregates (red circles).

open structure (e.g. OX50), the entanglement among the branches of different clusters can be easily initiated under shear flow (Figure 5.8(c)). Such entanglement can provide enough constraints to the particle motion and hence for such a system a smaller σ_{onset} is expected. On the other hand, as the aggregates become more closed with increasing n_i, the probability of entanglement between the branches decreases (Figure 5.8(d)). Thus, such a closed system requires higher stress to induce sufficient constraints to observe ST resulting in higher σ_{onset}. Additionally, as suggested in the zoomed parts of Figures 5.8(c) and 5.8(d), the contact area among the particles of different aggregates is significantly greater for open structure due to better entanglement and bigger primary particle size, whereas, the system with high internal branching exhibits less contact area due to lower degree of entanglement and smaller d_p (particles from different clusters which are in contact are marked by the red circles). This difference in contact area can result in a significant

difference in σ_{onset} for different types of FS samples. Also, such enhanced entanglement between the branches of different clusters allows significant interpenetration. Thus, FS samples having more open structures can be packed more efficiently resulting in higher ϕ_{max} values as compared to more compact samples. This rationalizes the systematic decrease in ϕ_{max} and range of ϕ showing ST, as we gradually go from OX50 to A380. Although the open structure allows entanglement among the aggregates easily, within a cluster the branches are weaker individually due to lack of connectivity. This can compromise the stress-bearing ability of the system during ST for ϕ values well below ϕ_{max}. In such cases, significant applied stress can also cause disentanglement of branches due to bending. At high enough applied stress beyond σ_{bend}, such stress-induced disentanglement can lower the propensity of stress-induced contact formation, thus decreasing the ST slope, as mentioned in Figures 5.6(a) and 5.6(b). Interestingly, as ϕ approaches ϕ_{max}, due to the high density of the clusters, each branch can find support from the branches of other clusters. This can suppress the stress-induced bending and disentanglement of the clusters resulting in a single ST slope like conventional ST systems (Figures 5.6(a) and 5.6(b)). As we approach more closed structures (e.g. in A300 and A380), they can completely suppress any stress-induced bending due to high internal connectivity. Thus, for these systems, the ST slope does not show a change for any value of ϕ (Figure 5.6(c)).

As mentioned earlier, nano-silica particles are fused together at high temperatures to form these irreversible aggregates. Breaking such aggregates requires very high force and can be considered stable clusters in our experiments. However, due to the fractal nature of these aggregates, they can further assemble together (due to high effective roughness) to form bigger, soft agglomerates which have also a fractal structure [8]. As these soft agglomerates are stabilized by physical constraints, they can easily break and reform under flow. The flow properties of the system are controlled by the breakage and reformation dynamics of these agglomerates, whereas, the breakage of fractal aggregates can be ignored due to their high stability as mentioned above. Such structural properties can also rationalize the variation of the onset stress with ϕ. With increasing ϕ, more such agglomerates are formed which break into small and more stable fractal aggregates as the shear stress increases causing the initial shear-thinning regime below σ_{onset}. Strong ST requires the formation of system-spanning frictional contacts between the rigid aggregates capable of dynamically withstanding high stresses. This implies that all the localized preformed agglomerates (which are usually weak) need to be broken to establish a homogeneous velocity gradient across the system. With increasing ϕ the number of such agglomerates increases, requiring more stress to break them before forming stress-induced

system-spanning frictional contacts between the rigid aggregates. This can cause σ_{onset} to increase with ϕ.

In order to verify our picture, we use in-situ boundary imaging during flow curve measurements. We map out the spatio-temporal nature of the flow field using the particle image velocimetry (PIV) technique. A typical PIV window is shown in Figure 5.9(a) where the yellow arrows represent the velocity vectors. The averaged velocity along the flow direction for a given y-position (measured from the top plate) is represented by v_x and the zero velocity plane ($v_x = 0$) is marked by a blue dashed line near the middle of the gap between the plates. We show the time evolution of the velocity profile ($v_x(y)$) at a constant applied stress in Figure 5.9(b) and 5.9(c) for $\sigma = 2Pa$ and $\sigma = 28Pa$, respectively over a time interval of 1 s. We find that v_x shows significant temporal fluctuations as shown in the insets of Figures 5.9(b) and 5.9(c) corresponding to a particular y-position as indicated by the vertical dashed lines in the figures. We quantify these temporal fluctuations in v_x in terms of the ratio of standard deviation and mean of v_x: δv_x = std (v_x)/mean (v_x). Figure 5.9(d) shows the variation of δv_x with increasing applied σ for different ϕ values. The temporal fluctuations are significantly higher for smaller applied stress values and reach a minimum close to σ_{onset}. Similarly, we quantify the temporal fluctuation in the position of the zero-velocity plane at constant σ as, δy = std $(y_{v_x=0})$/mean $(y_{v_x=0})$ where $y_{v_x=0}$ signifies the y-position of the zero velocity plane. Again we find that the δy is large for smaller σ values and gradually decreases with increasing σ. Figure 5.9(e) shows that δy reaches a minimum near σ_{onset}. Interestingly, we observe that for higher ϕ values, the spatio-temporal fluctuations, quantified by δv_x and δy significantly increase and it requires much higher applied stress to reach the minimum as compared to that corresponding to lower ϕ values (Figure 5.9(d) and 5.9(e)). This observation is in line with the variation of σ_{onset} with ϕ (Figure 5.1(c)). Such spatio-temporal fluctuations in the velocity profile are likely to come from the sample inhomogeneity arising from the preformed local stable structures. As σ approaches σ_{onset}, the inter-layer shearing becomes more homogeneous thereby reducing these fluctuations. This homogeneous shearing between layers is essential for better frictional contacts among aggregates and thus for strong ST [26]. We note that the δv_x might increase well beyond σ_{onset} due to plasticity [26]. In comparison, for a non-fractal system of suspensions of polystyrene particles, such a dependence of spatiotemporal fluctuations (δv_x and δy) on σ is absent (see orange squares in figure 5.9(d) and 5.9(e)). This result supports our conjecture that the localized stable agglomerates formed due to the branch-entanglement of fractal clusters play a crucial role in controlling the σ_{onset} variation.

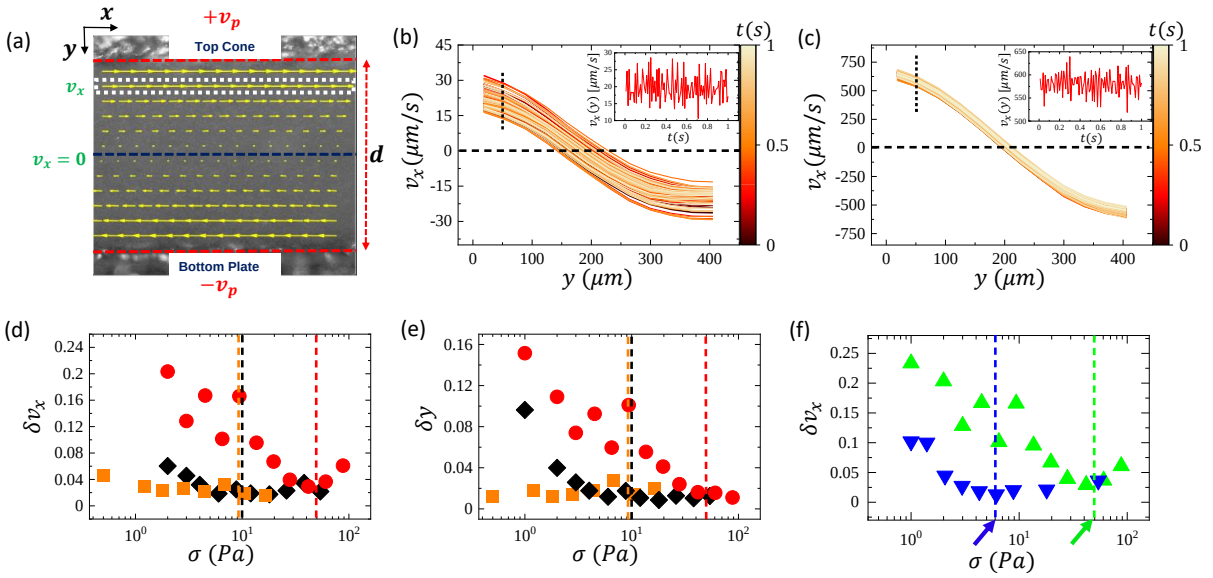

Figure 5.9: (a) Typical PIV window over the sample boundary image with the velocity vectors represented by the yellow arrows. The suspension is seeded with $3\mu m$ polystyrene particles for obtaining the flow profile. The gap at the boundary between two plates is represented by 'd'. $\pm v_p$ represents the top cone and bottom plate velocity respectively. v_x represents the velocity at a particular plane averaged along the flow direction at a given time. The zero velocity plane (at $v_x = 0$) is represented by the blue horizontal dash line. The white dotted box near the top plate represents the plane at which the temporal fluctuation in v_x is calculated. (b) and (c) represent the velocity profiles at constant stress $\sigma = 2Pa$ and $\sigma = 28Pa$ respectively for different instances of time as indicated by the color bar for the A380 sample at $\phi = 0.13$. Inset represents the temporal variation in velocity v_x at a distance y from the top plate, as marked by the vertical dashed line. (d) Temporal fluctuation in the velocity (δv_x) as a function of σ, at a particular plane, for $\phi = 0.08$ (black diamond) and $\phi = 0.13$ (red circle) in the A380 sample. (e) Fluctuation in the position of zero velocity plane (δy) as a function of σ for $\phi = 0.08$ (black diamond) and $\phi = 0.13$ (red circle) in the A380 sample. For comparison δv_x and δy variation is also shown for polystyrene sphere suspension (orange square) at $\phi = 0.58$ in (d) and (e) respectively. (f) Variation of δv_x with σ at constant $\phi = 0.13$ for A90 (blue down triangle) and A380 (green up triangle) sample. The vertical dashed lines of different colors (in panels (d), (e), (f)) represent the rheologically measured σ_{onset} for the corresponding sample as marked by the arrows in panel (f).

Furthermore, we observe, for a constant ϕ, the minima in the spatiotemporal fluctuations occur at larger stress with increasing internal branching of the system (Figure 5.9(f)). This again supports σ_{onset} variation for samples of different internal branching. As discussed before, in addition to the difference in effective contact area due to the difference in entanglement and d_p, the distance of ϕ from the ϕ_{max} might also have a significant

contribution. For a constant ϕ value, as the system with more internal branching is closer to ϕ_{max} than the system with less internal branching, the preformed rigid clusters require more stress to be destroyed and initiate the frictional contacts.

5.4 Conclusion

To summarize, we study shear thickening (ST) behavior in fumed silica suspensions for various particle types and volume fractions. These systems can show strong shear thickening even for significantly low particle volume fractions compared to conventional non-fractal ST systems. Additionally, we find other differences in the ST behavior in FS systems that either remain unexplored or, are very limited explored. Some of these are: (i) FS systems show ST over a much wider range of ϕ values, (ii) exponential variation of σ_{onset} with ϕ where the rate of increase systematically depends on types of FS sample used, (iii) decrease in shear thickening exponent which is reversible. These differences highlight that the phenomenon of ST in the FS systems is not captured by the existing models describing ST in non-fractal particulate systems and requires the incorporation of additional complex structural information of fractal clusters.

Our systematic study presents a physical picture of the ST in terms of branch entanglement and openness of the structure. This highlights the role of these geometrical parameters in controlling the shear-thickening behavior despite the similarity of the surface properties of primary nano silica particles forming the fractal aggregates. Future studies should be carried out using in-situ x-ray scattering for more insights into the shear-induced entanglement between the fractal aggregates having a wide range of fractal dimensions. The different types of fumed silica used in this study are characterized by the presence of silanol (Si-OH) groups on the particle surface that aid the formation of hydrogen bonding. However, quantifying the interparticle interaction and its correlation with the observed onset stress of shear-thickening requires more sophisticated experimental techniques like Atomic Force Microscopy (AFM) which remains an interesting future direction to explore.

We hope that our study will motivate further experimental and theoretical studies on the ST phenomena in suspensions of fractal objects.

Bibliography

[1] Sachidananda Barik, Pradip K. Bera, A.K. Sood, and Sayantan Majumdar. Shear thickening of dilute suspensions of fractal silica aggregates. *Journal of Non-Newtonian Fluid Mechanics*, 328:105246, 2024.

[2] Eric Brown, Nicole A Forman, Carlos S Orellana, Hanjun Zhang, Benjamin W Maynor, Douglas E Betts, Joseph M DeSimone, and Heinrich M Jaeger. Generality of shear thickening in dense suspensions. *Nature materials*, 9(3):220–224, 2010.

[3] Matthieu Wyart and ME Cates. Discontinuous shear thickening without inertia in dense non-brownian suspensions. *Physical Review Letters*, 112(9):098302, 2014.

[4] Romain Mari, Ryohei Seto, Jeffrey F Morris, and Morton M Denn. Shear thickening, frictionless and frictional rheologies in non-brownian suspensions. *Journal of Rheology*, 58(6):1693–1724, 2014.

[5] Young S Lee, Eric D Wetzel, and Norman J Wagner. The ballistic impact characteristics of kevlar® woven fabrics impregnated with a colloidal shear thickening fluid. *Journal of materials science*, 38(13):2825–2833, 2003.

[6] Abhijit Majumdar, Bhupendra Singh Butola, and Ankita Srivastava. Optimal designing of soft body armour materials using shear thickening fluid. *Materials & Design*, 46:191–198, 2013.

[7] F Pinto and M Meo. Design and manufacturing of a novel shear thickening fluid composite (stfc) with enhanced out-of-plane properties and damage suppression. *Applied Composite Materials*, 24:643–660, 2017.

[8] Andrew Mulderig, Gregory Beaucage, Karsten Vogtt, Hanqiu Jiang, and Vikram Kuppa. Quantification of branching in fumed silica. *Journal of Aerosol Science*, 109:28–37, 2017.

[9] Qiu-mei Wu, Jian-ming Ruan, Bai-yun Huang, Zhong-cheng Zhou, and Jian-peng Zou. Rheological behavior of fumed silica suspension in polyethylene glycol. *Journal of Central South University of Technology*, 13:1–5, 2006.

[10] S.M Olhero and J.M.F Ferreira. Influence of particle size distribution on rheology and particle packing of silica-based suspensions. *Powder Technology*, 139(1):69–75, 2004.

[11] T Ajeeth Prabhu and Anugrah Singh. Effect of carrier fluid and particle size distribution on the rheology of shear thickening suspensions. *Rheologica Acta*, 60:107–118, 2021.

[12] Parvin Alaee, Milad Kamkar, and Mohammad Arjmand. Fumed silica-based suspensions for shear thickening applications: a full-scale rheological study. *Langmuir*, 38(16):5006–5019, 2022.

[13] Philippe Bourrianne, Vincent Niggel, Gatien Polly, Thibaut Divoux, and Gareth H. McKinley. Tuning the shear thickening of suspensions through surface roughness and physico-chemical interactions. *Phys. Rev. Res.*, 4:033062, Jul 2022.

[14] Mike van der Naald, Liang Zhao, Grayson L Jackson, and Heinrich M Jaeger. The role of solvent molecular weight in shear thickening and shear jamming. *Soft Matter*, 17(11):3144–3152, 2021.

[15] Tekkati Ajeeth Prabhu and Anugrah Singh. Rheology and microstructure of discontinuous shear thickening suspensions. *Journal of Rheology*, 66(4):731–747, 2022.

[16] Anatoli Kurkin, Vitali Lipik, Xin Zhang, and Alfred Tok. In situ observation of shear-induced jamming front propagation during low-velocity impact in polypropylene glycol/fumed silica shear thickening fluids. *Polymers*, 14(14):2768, 2022.

[17] Eric Brown and Heinrich M Jaeger. The role of dilation and confining stresses in shear thickening of dense suspensions. *Journal of Rheology*, 56(4):875–923, 2012.

[18] Subhransu Dhar, Sebanti Chattopadhyay, and Sayantan Majumdar. Signature of jamming under steady shear in dense particulate suspensions. *Journal of Physics: Condensed Matter*, 32(12):124002, 2019.

[19] Eric Brown and Heinrich M Jaeger. Shear thickening in concentrated suspensions: phenomenology, mechanisms and relations to jamming. *Reports on Progress in Physics*, 77(4):046602, 2014.

[20] Jeffrey F. Morris. Shear thickening of concentrated suspensions: Recent developments and relation to other phenomena. *Annual Review of Fluid Mechanics*, 52(1):121–144, 2020.

[21] Chiao-Peng Hsu, Shivaprakash N Ramakrishna, Michele Zanini, Nicholas D Spencer, and Lucio Isa. Roughness-dependent tribology effects on discontinuous shear thickening. *Proceedings of the National Academy of Sciences*, 115(20):5117–5122, 2018.

[22] Dale W Schaefer and Alan J Hurd. Growth and structure of combustion aerosols: fumed silica. *Aerosol Science and Technology*, 12(4):876–890, 1990.

[23] Sotiris E Pratsinis. Flame aerosol synthesis of ceramic powders. *Progress in Energy and Combustion Science*, 24(3):197–219, 1998.

[24] John R Royer, Daniel L Blair, and Steven D Hudson. Rheological signature of frictional interactions in shear thickening suspensions. *Physical Review Letters*, 116(18):188301, 2016.

[25] R. V. More and A. M. Ardekani. Unifying disparate rate-dependent rheological regimes in non-brownian suspensions. *Phys. Rev. E*, 103:062610, Jun 2021.

[26] Sachidananda Barik, Akhil Mohanan, and Sayantan Majumdar. Role of plasticity in the universal scaling of shear thickening dense suspensions, 2023.

CHAPTER

SIX

Role of plasticity in the universal scaling of shear thickening dense suspensions

"Man is unique not because he does science, and he is unique not because he does art, but because science and art equally are expressions of his marvelous plasticity of mind."

- Jacob Bronowski -

The results covered in this chapter are published in the article, Rheol Acta 63, 291–300 (2024) [1].

6.1 Introduction

As discussed before, a classic example of non-Newtonian flow behavior is the phenomenon of shear thickening (ST) [2, 3] and many of these systems show a stress-induced transformation to a solid-like shear jammed (SJ) state when ϕ approaches the random close packing ϕ_{rcp} limit. As SJ involves a sudden increase in shear modulus as the material transforms to a solid-like state from a liquid-like state, a natural question arises: Is SJ transition a non-equilibrium phase transition? For granular systems, the increase in dynamic correlation reflected in growing length and time scales near the jamming transition also suggests a connection to phase transition and critical phenomenon [4]. In the system of soft frictionless spheres, the finite size scaling collapse of elastic moduli and number of contacts further strengthen such idea [5, 6].

Recent numerical and theoretical studies indicate that with increasing shear stress, the hydrodynamic lubrication layer between the particles breaks down beyond a stress onset giving rise to frictional contacts. Such stress-induced proliferation of frictional contacts captures almost all the essential features of DST and SJ phenomena [7, 8]. The increase in suspension viscosity η with the particle volume fraction ϕ is well described by the phenomenological Krieger-Dougherty (KD) relation given by $\eta \sim \left(1 - \frac{\phi}{\phi_J}\right)^{-\beta}$, where ϕ_J is the jamming volume fraction and $\beta \approx 2$ for spherical particles. This indicates that as ϕ closely approaches ϕ_J, the viscosity enhances rapidly and finally diverges at $\phi = \phi_J$. For shear-thickening dense suspensions, ϕ_J depends on σ. For these systems, using the concept of stress-induced proliferation of frictional contacts, Wyart-Cates model proposes a functional form for stress-dependent jamming volume fraction $\phi_J = f(\sigma)\phi_m + [1 - f(\sigma)]\phi_0$, where $f(\sigma) = e^{-(\sigma^*/\sigma)}$ denotes the fraction of frictional contacts, σ^* is the onset stress for the frictional contact formation. $f(\sigma)$ varies between 0 and 1 depending on the applied shear stress. Here, ϕ_0 represents the jamming volume fraction without frictional contacts known as the isotropic jamming point (corresponding to $f = 0$). When all the contacts are frictional we get the frictional jamming point ϕ_m (corresponding to $f = 1$).

For different ST and SJ systems, a very recent work [9] proposes a universal scaling of viscosity over wide range of stress and volume fraction values. This study highlights the importance of two fixed points, namely, isotropic jamming point (ϕ_0) and frictional jamming point (ϕ_m) in controlling such scaling behavior. Incorporating the concept of stress

induced frictional interaction as proposed in the Wyart-Cates (WC) model [7, 8, 10], they expressed the viscosity η of a shear thickening system as,

$$\eta(\phi_0 - \phi)^2 \sim \left(\frac{1}{\phi_0 - \phi_m} - \frac{f(\sigma)}{\phi_0 - \phi} \right)^{-2} \tag{6.1}$$

Such functional form indicates that irrespective of the value of ϕ, $\eta(\phi_0 - \phi)^2$ as function of $x_{WC} = \frac{f(\sigma)}{\phi_0 - \phi}$ should diverge at a single point $x_c = \frac{1}{\phi_0 - \phi_m}$ for $\phi < \phi_0$. However, it is observed that $\eta(\phi_0 - \phi)^2 \sim F\left(\frac{f(\sigma)}{\phi_0 - \phi}\right)$ shows a clear variation in diverging point for different ϕ values [9]. Incorporating some careful modifications in Eq. 6.1, they overcome such discrepancies and derive a universal scaling relation.

This scaling framework originally proposed by J. Cardy [11] is tested numerically for a ST system of bidisperse particles where a good agreement has been obtained [12]. Further, the scaling variable can also be modified to incorporate the effect of orthogonal shear perturbations [13]. A similar scaling relation has also been used for fractal suspensions showing a direct transition to SJ from a flowing state under increasing stress [14]. Such universal scaling theory seems to be a promising approach in combining all the theoretical, numerical and experimental works. The change in power-law slope in the observed scaling curve [9] is attributed to the crossover between two fixed jamming points, ϕ_0 and ϕ_m. This suggest that the frictionless and frictional region belongs to two different universality classes and the change in slope reflects a transition from frictionless to frictional regime. Although such a picture of the stress-induced transition from a frictionless to a frictional regime is interesting, a direct experimental manifestation of such transition on the flow behavior, concerning the universal scaling behavior of ST system, is yet to be explored.

In this chapter, we study the steady state flow behavior of two well characterized dense suspensions using shear rheology and in-situ high resolution boundary imaging. Using particle imaging velocimetry (PIV) technique, we map out spatio-temporal flow and deformation of the system across the crossover of the universal scaling curve. We observe that the crossover in the scaling curve is associated with friction-dominated phenomena, such as granular dilation and shear band plasticity which in turn play a major role in changing the slope of the scaling curve.

6.2 Materials and methods

The experiments are carried out for two standard shear thickening (ST) dense suspensions,(i) Cornstarch (CS) particles (Sigma-Aldrich) with mean diameter $d = 15 \pm 5\ \mu m$ dispersed in glycerol and (ii) Polystyrene (PS) particles dispersed in polyethylene glycol(PEG) 400. We synthesize PS particles of two different size distributions ($d = 8 \pm 4\ \mu m$ and $d = 2.65 \pm 0.13\ \mu m$) using the dispersion polymerization technique [15, 16]. As described in Chapter 2, the samples of different volume fractions (ϕ) are prepared by gradually adding the required amount of dry particles into the solvent and thoroughly mixed at each step using a spatula. The volume fraction range used for CS system is $0.40 \leq \phi \leq 0.54$ and that for PS system is $0.50 \leq \phi \leq 0.61$.

All the rheological measurements are performed on a stress control Rheometer (MCR-702, Anton Paar, Austria) in twin drive 50-50 counter movement mode. For the CS particle suspension the measurements are carried out using parallel plate geometry of plate diameter 25 mm with 1 mm gap between the plates and for PS particle suspensions cone and plate geometry with the cone angle of 2°and cone/plate of 25 mm diameter is used. In order to remove the loading history, if any, we conduct an oscillatory amplitude sweep measurement at a frequency of 1 Hz just after loading the sample. For this, we first increase the strain amplitude (γ) logarithmically from a lower to a maximum value and then the amplitude is again gradually decreased to the initial value. For steady-state flow curve measurements, we increase the applied shear stress (σ) from a smaller to maximum value logarithmically with waiting time per data point varying between 20 s to 1 s between minimum and maximum stress, respectively, and then perform a reverse run.

Using a high-speed in-situ imaging set up we obtain the sample boundary images during the flow curve measurement. Since the samples are optically opaque, the in-situ imaging of the boundary is possible only under reflection mode [17]. The sample boundary is illuminated using a LED light source (Dolan-Jenner Industries) and image the flow gradient plane using a high-speed monochrome CMOS camera (Phantom Miro C210) with $5X$ and $10X$ long working distance objective (Mitutoyo). All the images are captured at a frame rate of 100 Hz with resolution 1280×1024 and 1280×720 pixels for parallel plate and cone-plate geometries, respectively.

From the sample boundary images, we map out the flow profiles using particle imaging velocimetry (PIV) technique. The PIV analysis is performed using custom-written PIV codes developed in MATLAB software.

6.3 Results and discussions

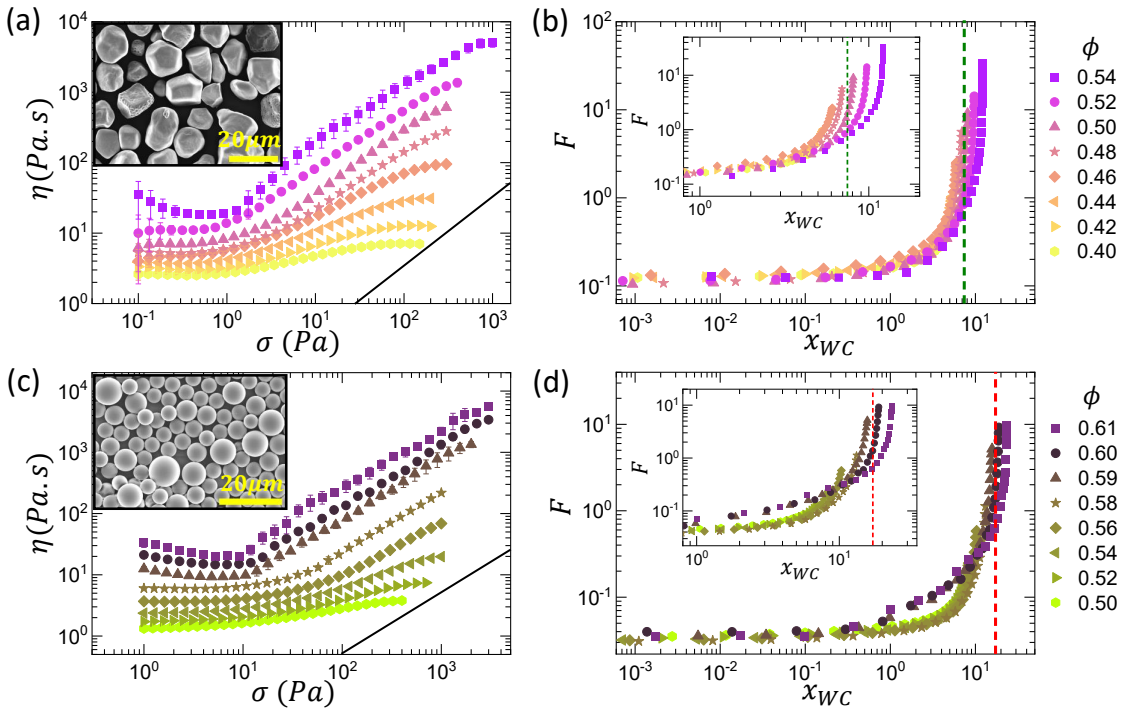

Figure 6.1: (a) and (c) Variation of viscosity η with shear stress σ shows the ST properties of cornstarch particles dispersed in glycerol and polystyrene particles dispersed in PEG 400 respectively for different volume fraction ϕ as shown in the legends. Slope 1 is indicated by the solid black line. The corresponding particle image is represented in the inset. (b) and (d) Variation of WC scaling function F with WC variable x_{WC} for different ϕ. Inset (magnified plot): $F(x_{WC})$ does not diverge at a single point for different ϕ. Dashed lines represent the expected point of divergence $x_c = 7.8$ and 17.8 for cornstarch and polystyrene systems respectively.

The flow curves are obtained for dense suspensions of cornstarch and polystyrene at different volume fractions (ϕ) as shown in Figure 6.1(a) and 6.1(c) respectively. We observe an increase in viscosity (η) with increasing shear stress (σ) beyond an onset stress indicating shear thickening. The degree of shear thickening enhances with increasing ϕ. The black solid lines in Figure 6.1(a) and 6.1(c) having a power-law slope of 1 indicate that CS and PS systems show DST for $\phi \geq 0.48$ and $\phi \geq 0.58$, respectively. The respective onset stress values for CS and PS systems are close to 1 Pa and 10 Pa. Following a recent work [15], using the Krieger-Dougherty (KD) equation and WC model we determine ϕ_0, ϕ_m, and σ^* from the flow curves for both of these systems, as shown in Figure 6.2, to estimate the WC scaling variable and scaling function mentioned in [9] (Appendix-2). Here,

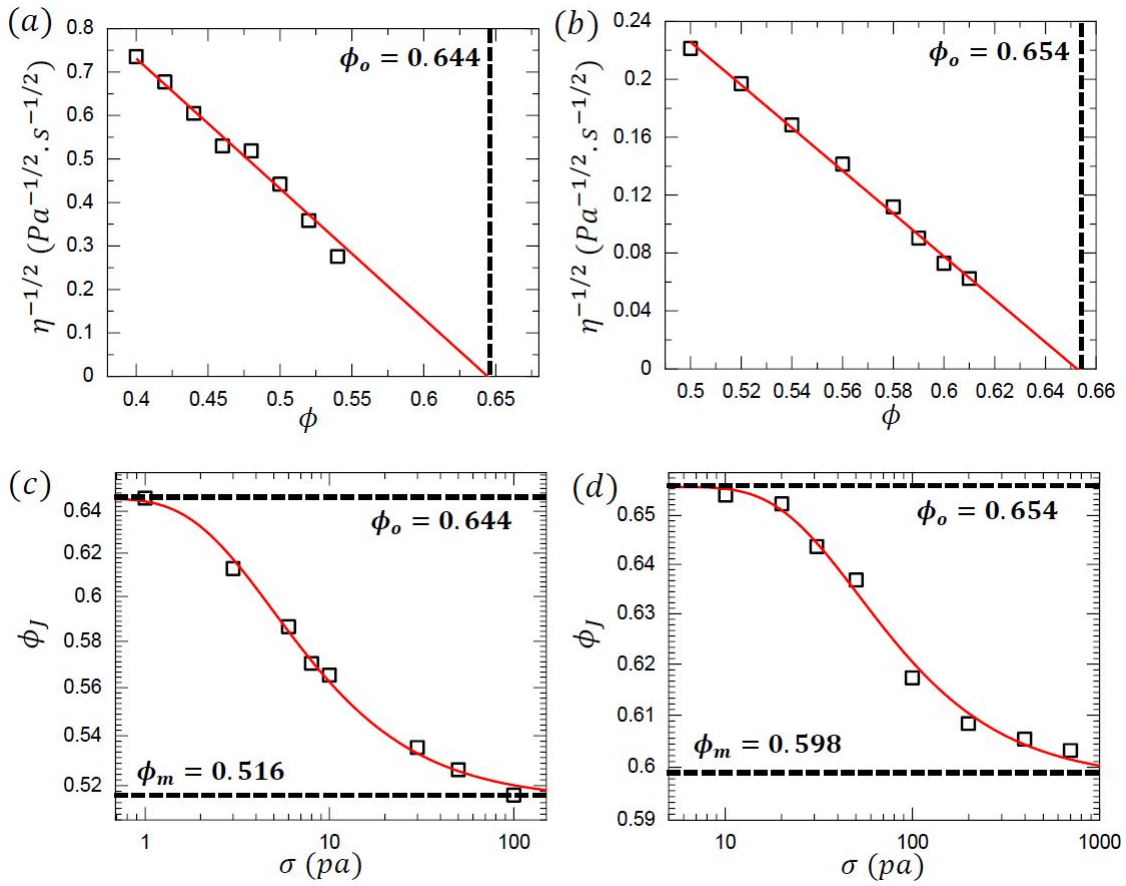

Figure 6.2: (a) and (b) Determination of ϕ_o, as marked by vertical dashed lines, from the Krieger Dougherty (KD) relation fitting for cornstarch (CS) and polystyrene (PS) system respectively. (c) and (d) Variation of jamming volume fraction ϕ_J with σ for CS and PS system. The red solid line indicates the fit to the Wyart-Cates(WC) model to get the parameters ϕ_m and σ^*. The top and bottom horizontal dashed lines indicate the obtained ϕ_0 and ϕ_m values. For CS system ϕ_0 =0.644 , ϕ_m=0.516 and $\sigma^* = 4.5\ Pa$; for PS system $\phi_0 = 0.654$, $\phi_m = 0.598$ and $\sigma^* = 59\ Pa$.

we note that the σ^* value obtained from the WC model is higher than the onset stress for shear thickening [15]. We also verify these system-dependent parameters by directly fitting the flow curves using WC model (Figure 6.3). Figure 6.1(b) and 6.1(d) show the variation of WC scaling function $F = \eta(\phi_0 - \phi)^2$ with WC variable $x_{WC} = \frac{f(\sigma)}{\phi_0 - \phi}$. It shows that for different ϕ, $\eta(\phi_0 - \phi)^2 \sim F\left(\frac{f(\sigma)}{\phi_0 - \phi}\right)$ diverges at different points (inset of Figure 6.1(b) and 6.1(d)), whereas, from equation 6.1, it is expected to diverge at $x_c = \frac{1}{\phi_0 - \phi_m}$, as marked by the dashed lines. To avoid this discrepancy, following [9], one can try modifying Wyart-Cates expression (Eq. 6.1) using a ϕ dependence in $f(\sigma)$. So the Eq. 6.1 can be modified as,

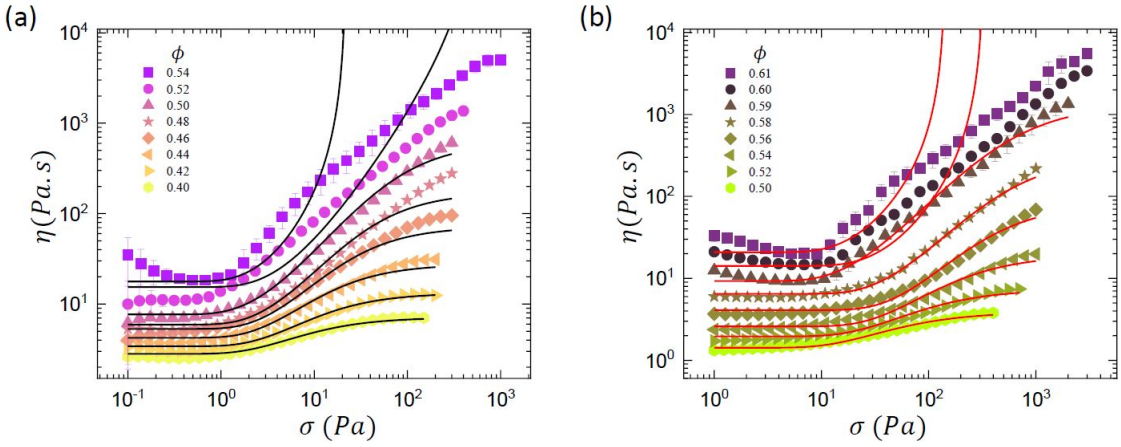

Figure 6.3: The flow curve data ($\eta - \sigma$ plot) of cornstarch (a) and polystyrene (b) system (symbols), same as the data shown in Figure 6.1(a) and 6.1(c) respectively. The flow curves are fitted to the Wyart-Cates(WC) model (solid lines) using the parameters ϕ_0 and ϕ_m values obtained in Figure 6.2. The WC model fitting is reasonably good for $\phi < \phi_m$, but for $\phi > \phi_m$ the WC model can not be fitted well, constraining the parameters ϕ_0, ϕ_m and the KD relation exponent β. For better fitting one can keep the parameters ϕ_0, ϕ_m, and β free, but then the values of these parameters become volume fraction dependent, which is not physical. Such discrepancy in fitting for the high volume fraction data reflects the deviation of experimental results from the theoretical prediction in the shear jammed regime.

$$\eta(\phi_0 - \phi)^2 \sim \left(\frac{1}{\phi_0 - \phi_m} - \frac{g(\sigma,\phi)}{\phi_0 - \phi}\right)^{-2} \tag{6.2}$$

where $g(\sigma,\phi) = C(\phi)f(\sigma)$ and $C(\phi)$ is a volume fraction dependent parameter called the anisotropy factor. Now plotting $\eta(\phi_0 - \phi)^2$ as function of $x = \frac{g(\sigma,\phi)}{\phi_0 - \phi}$ gives an excellent collapse at the diverging point $x_c = \frac{1}{\phi_0 - \phi_m}$ [Figure 6.4(a)]. It is to note that as the ϕ_0 and ϕ_m are system-dependent parameters, we get different diverging points x_c for different systems: $x_c = 7.8$ and 17.8 for the cornstarch and polystyrene system, respectively. In principle, one can choose a constant diverging point x_c irrespective of system type [9]. However, we choose the diverging point that emerges from the system parameters. We would like to point out that here, we incorporate only the essential modification required to collapse the diverging points [9].

Eq.6.2 suggests that, $\eta(\phi_0 - \phi)^2 \sim F\left(\frac{g(\sigma,\phi)}{\phi_0 - \phi}\right)$ should diverge with exponent -2. For better visualization of the exponent, Eq.6.2 can be recast as (see Appendix-2),

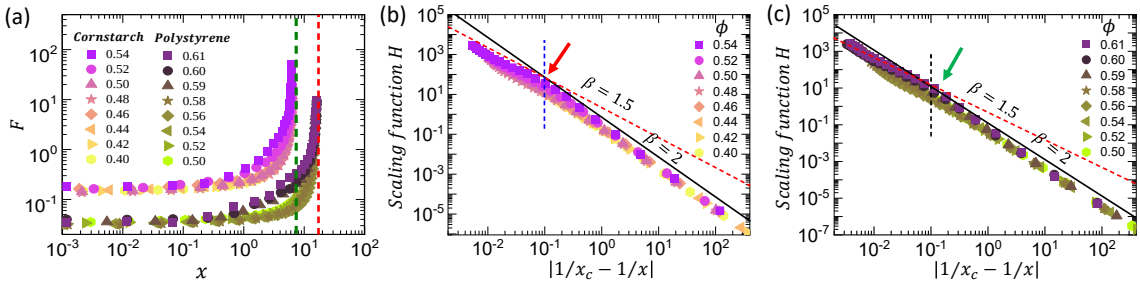

Figure 6.4: (a) Variation of WC scaling function F with modified WC variable x for cornstarch and polystyrene systems at different ϕ as shown in legends. Two dashed lines represent the divergence points x_c for the corresponding system. (b) and (c) Modified scaling function $H = \eta(g(\sigma,\phi))^2$ as function of new scaling variable $\left|\frac{1}{x_c} - \frac{1}{x}\right|$ for cornstarch and polystyrene system respectively at different ϕ. The crossover between the solid and dashed line (marked by the vertical dotted line) represents the change in the magnitude of slope (β) from 2 to 1.5 and the arrow indicates the crossover point [9].

$$\eta(g(\sigma,\phi))^2 \sim (\phi_0 - \phi_m)^2 \left(\frac{1}{x} - \frac{1}{x_c}\right)^{-2} \tag{6.3}$$

$$\eta(g(\sigma,\phi))^2 \sim H\left(\left|\frac{1}{x_c} - \frac{1}{x}\right|\right) \tag{6.4}$$

Plotting the scaling function $H = \eta(g(\sigma,\phi))^2$ as a function of scaling variable $\left|\frac{1}{x_c} - \frac{1}{x}\right|$, we can see that the viscosity η over a wide range of σ and ϕ collapse into a single curve, called universal scaling curve as shown in Figure 6.4(b) and Figure 6.4(c) for CS and PS systems, respectively. Interestingly, we observe that magnitude of the slope of the scaling curve (β) that represents the exponent of viscosity divergence, does not remain the same: β decreases from 2 below a certain value of scaling variable and approaches 1.5. Here we note that the smaller value of the scaling variable $\left|\frac{1}{x_c} - \frac{1}{x}\right|$ corresponds to the larger value of σ and vice versa. This suggests the change in the slope of the universal scaling curve happens beyond a certain value of the σ called the crossover point stress (σ_c). The crossover points, where the slope change starts, are marked by the red and green arrows and the σ_c for the CS system ($\phi = 0.54$) and PS system ($\phi = 0.61$) are 11 Pa and 67 Pa, respectively. The change in magnitude of the power-law slope from 2 to 1.5 is particularly evident for higher ϕ values (Figure 6.4(b) and Figure 6.4(c)), for which the flow curves can be obtained for larger stress values before the sample yields, as shown in Figure 6.1(a) and 6.1(c).

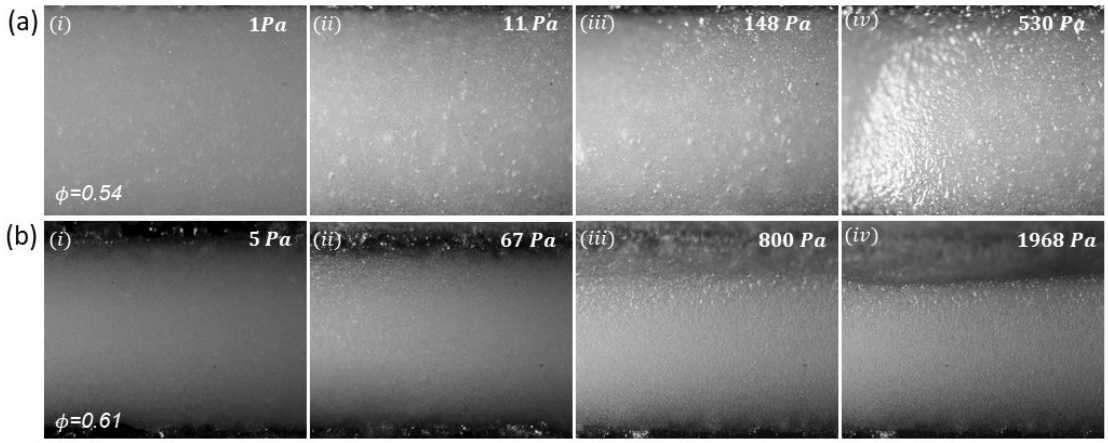

Figure 6.5: Sample boundary images for dense suspension of (a) CS at $\phi = 0.54$ and (b) PS ($d = 8 \pm 4\ \mu m$) at $\phi = 0.61$ with increasing σ during the flow curve. The corresponding σ values are mentioned inside the images.

In order to understand the physical origin of the change in slope in the universal scaling curve, we use in-situ sample boundary imaging during the rheological measurements [18, 19, 20, 16]. Figure 6.5 represents the boundary images of the sample at different applied σ (marked inside each panel) for CS (Figure 6.5(a)) and PS (Figure 6.5(b)) system for $\phi = 0.54$ and $\phi = 0.61$, respectively. During the flow curve measurement, we observe no change in surface intensity till $\sigma < \sigma_c$ (panel (i) of Figure 6.5(a) and 6.5(b)). However, for $\sigma > \sigma_c$ significant increase in the surface intensity is observed (panel (ii) and (iii) of Figure 6.5(a) and 6.5(b)). Such change in intensity arises due to the shear-induced protrusion of the particle at the suspension-air interface due to a mechanism called frustrated dilation [21, 22]. Shear-induced dilation in dense granular suspensions is related to the shear-induced proliferation of interparticle frictional contacts spanning the system [21, 22, 23, 16, 24, 25, 26]. The dilation starts at $\sigma \approx \sigma_c$ (panel (ii) of Figure 6.5(a) and 6.5(b), Movies S4 and S5 [27]). A similar dilation effect has been reported earlier for granular systems in the shear thickening regime [21, 22]. Here we should note that the particle protrusion at the interface during dilation is distinct from the free surface deformation observed in the flow of suspensions with intermediate particle volume fractions well below the jamming point. The free surface deformation in particulate suspensions has been widely studied [28, 29, 30]. It has been reported that the degree of surface deformation depends on particle size, particle concentration, viscosity and surface tension of the medium [30, 31, 32]. A recent study found that such deformation is purely due to hydrodynamic fluctuations resulting from the competing effects of fluctuation in particle motion and suppression

of the same due to viscous dissipation. While fluctuations grow with the increase in the particle concentration, the suspension viscosity also grows which eventually suppresses the fluctuations [31]. Thus, the free surface fluctuations decrease with an increase in particle volume fraction. On the contrary, the deformation of the air-suspension interface due to dilation is observed at a much higher concentration of the particles (close to jamming) where the stresses are transmitted through the frictional contacts. The signature of such frictional interactions in shear-thickening dense granular suspensions is well established in the literature from a combination of experimental and numerical studies [7, 33, 34, 35, 36]. We find from the imaging experiments that for $\sigma \approx \sigma_c$ the dilation is intermittent in nature (Movie S3 [27]). However, as σ goes beyond σ_c the dilation becomes stable and system-spanning. On further increase in σ, we observe the development of failures in the system in the form of boundary fracture or shear-band plasticity (panel (iv) of Figure 6.5(a) and 6.5(b)). The connection of our observation with the shear-induced transient structure formation and wall slippage in shear-thickening systems [37, 38, 39, 40, 41] need further exploration.

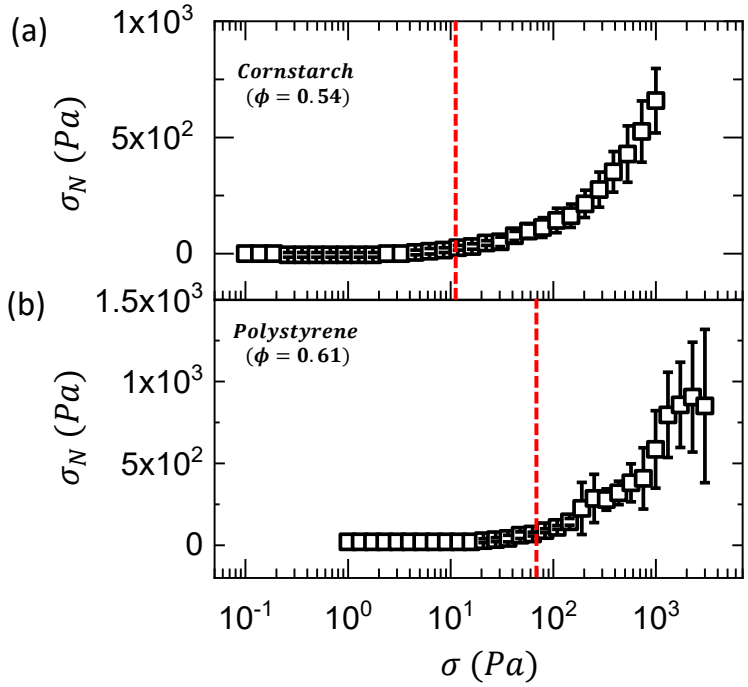

Figure 6.6: Variation of axial normal stress σ_N with shear stress σ during the flow curve for (a) CS system at $\phi = 0.54$ and (b) PS system $\phi = 0.61$. The corresponding crossover point stress σ_c is marked by the vertical dashed line.

To further characterize the flow regimes, we study the variation of the axial normal

stress in the system under shear. For smaller applied stress values below σ_c the normal stress (σ_N) remains negligible, however, after the crossover point ($\sigma \geq \sigma_c$) a significant positive σ_N starts to develop that increases with increasing σ (Figure 6.6(a) and 6.6(b)). Here we observe that the onset of dilation and positive normal stress coincides with σ_c. A very recent study experimentally demonstrates how the enhanced particle pressure (related to the normal stress difference) can transform lubricated contacts into frictional contacts during shear thickening [42]. The existence of such high, positive normal stresses comparable to the applied shear stress in dense granular suspensions has been attributed to the mechanism of frustrated dilation [21, 43]. We find that such positive normal stress becomes negligible at ϕ <0.42 for cornstarch and ϕ <0.52 for polystyrene systems. Interestingly, dense suspensions of smaller polystyrene particles (closer to the colloidal regime) require very high stresses $\sigma >> \sigma_c$ for the observation of dilation and positive σ_N (Figure 6.7). This is due to the high values of confining stresses (proportional to the

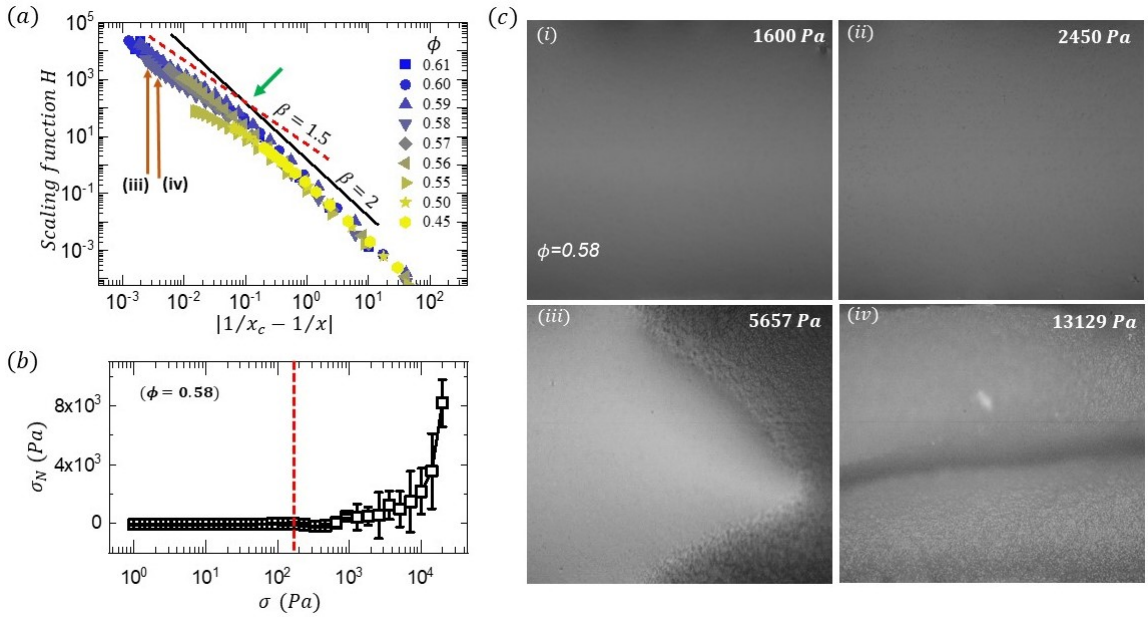

Figure 6.7: (a) Scaling curves for dense suspension of small polystyrene particles of diameter $d = 2.65 \pm 0.13\ \mu m$ dispersed in PEG 400 at different volume fractions as shown in the legend. The black solid line and red dashed line represent the slope -2 and -1.5 respectively. The crossover point is marked by the green arrow. (b) Variation of normal stress σ_N with shear stress σ during flow curve for small polystyrene system ($\phi = 0.58$). The corresponding cross-over stress $\sigma_c = 167Pa$ is marked by the vertical dashed line. (c) Sample boundary images at four different stress values for $\phi = 0.58$. Panel (iii) and (iv) represents the onset of dilation (at $\sigma = 5657\ Pa$) and fracture (at $\sigma = 13129\ Pa$) respectively which are found deep inside the regime of slope -1.5 as shown in (a).

inverse of particle diameter) [21].

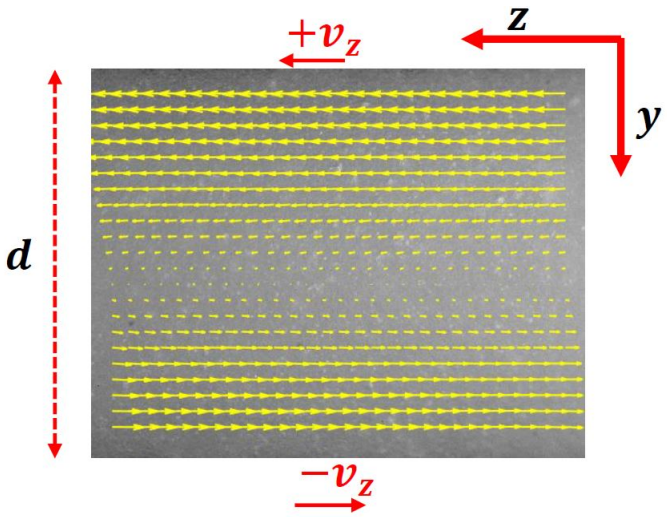

Figure 6.8: Typical PIV window for sample boundary image with top and bottom plate moving at velocity $+v_z$ and $-v_z$ respectively. Yellow arrows represent the velocity vector parallel to the plate (obtained from PIV). "d" is the gap between the two plates.

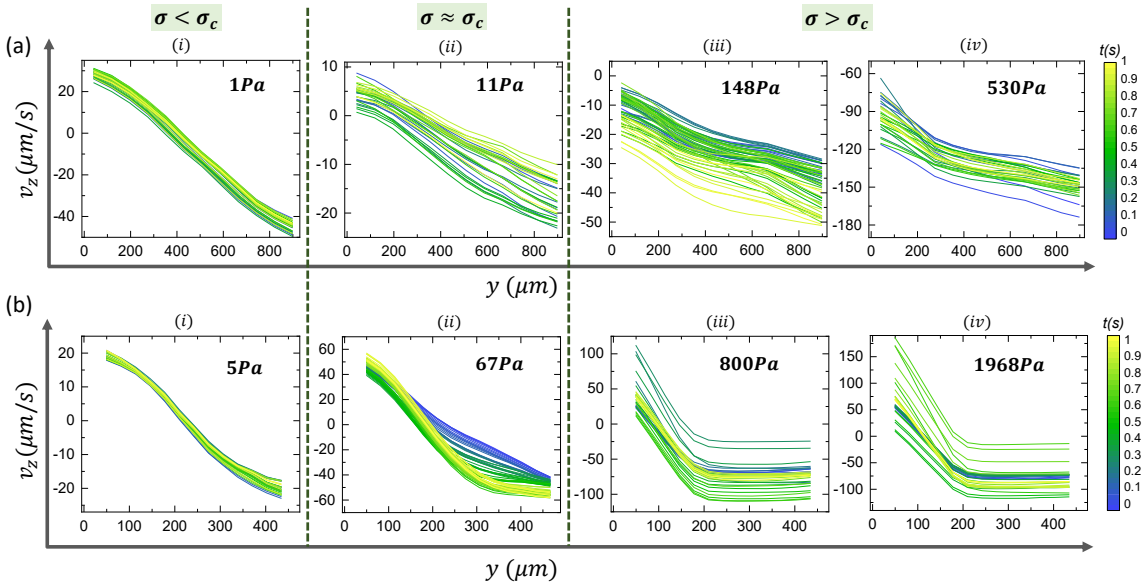

Figure 6.9: Velocity profiles at four different stress values, during the flow curve, for dense suspensions of (a) CS particles at $\phi = 0.54$ and (b) PS particles at $\phi = 0.61$. Each panel represents the velocity profiles for one second, as shown in the color bars, and the corresponding stress values are mentioned inside the panels.

Next, we quantify the flow dynamics in the different scaling regimes using Particle Image Velocimetry (PIV) technique. For a given applied stress (σ) we measure the average value of the velocity components (v_z) parallel to the plate motion. The variation of v_z across the gap (y) between the shearing plates gives the velocity profiles in the flow-gradient plane. Figure 6.8 shows a typical PIV window obtained from the in-situ boundary imaging of the sample. Here, as per our convention for the twin drive 50-50 counter movement mode, the v_z close to the top plate ($y = 0$) is positive, and the bottom plate is negative. Figure 6.9 represents the evolution of the velocity profile with increasing σ for both corn starch (CS) and polystyrene (PS) suspensions (Figure 6.9(a) and 6.9(b)) for $\phi = 0.54$ and $\phi = 0.61$, respectively. For $\sigma < \sigma_c$, as shown in panel (i) of Figure 6.9(a) and 6.9(b), the velocity profiles remain stationary in time and the nature remains close to a linear profile. The position of the zero velocity plane ($v_z = 0$) appears near the middle of the gap between the two plates. Interestingly, when σ approaches σ_c the velocity profiles lose the stationary behavior showing random shifting in time (Panel (ii) in Figure 6.9(a) and 6.9(b)). Here, the zero velocity plane starts shifting towards one of the plates. Similar to the dilation event at $\sigma \approx \sigma_c$, the velocity profiles are also spatio-temporally fluctuating in this stress regime. At $\sigma >> \sigma_c$ (Panel (iii) and (iv) in Figure 6.9(a) and 6.9(b)), we observe shear band plasticity and fracture in the system (Movies S4 and S5 [27]). Here, we have used the term plasticity in a broad sense to describe shear-induced failures in the sample. In the viscous scaling regime (at lower applied stresses), the flow remains mostly uniform; however, at larger applied stresses, non-affinity develops in the system. Such non-affinity is reflected as shear band formation, wall slippage, and crack opening. For shear-jammed dense suspensions, the banding comes due to failure in the system when it transforms to a solid-like shear-jammed state under high applied stresses since such a state can not sustain a steady flow. A jammed state can only flow heterogeneously by creating plasticity and fractures. Although the exact nature of flow heterogeneity depends on system details, the appearance of plasticity/non-affinity is a general feature of the flow of shear-jammed dense suspensions. At the crossover stress value, the random orientation direction of the velocity vectors indicates the existence of the significant velocity component in the y-direction. This is an additional signature of spatial heterogeneity of the strain field or, non-affine deformation in the system (Movie S4 [27]) [44]. Such heterogeneous flow in shear jammed dense suspensions has been reported earlier for polystyrene and cornstarch systems [16, 45]. In these systems, the onset of non-affinity or plasticity in the shear jammed state is characterized by the appearance of shear bands, and at the band interface, a crack opening takes place at higher stresses. We

observe that for the CS system (Panel (iii) and (iv) in Figure 6.9(a)), the entire sample moves in the direction opposite to the direction of motion of the top plate, whereas, the PS system shows two band structures moving opposite to each other (Panel (iii) and (iv) in Figure 6.9(b)). The density matching of the system (CS is not density matched with the solvent but, PS is) might play a role in creating such differences.

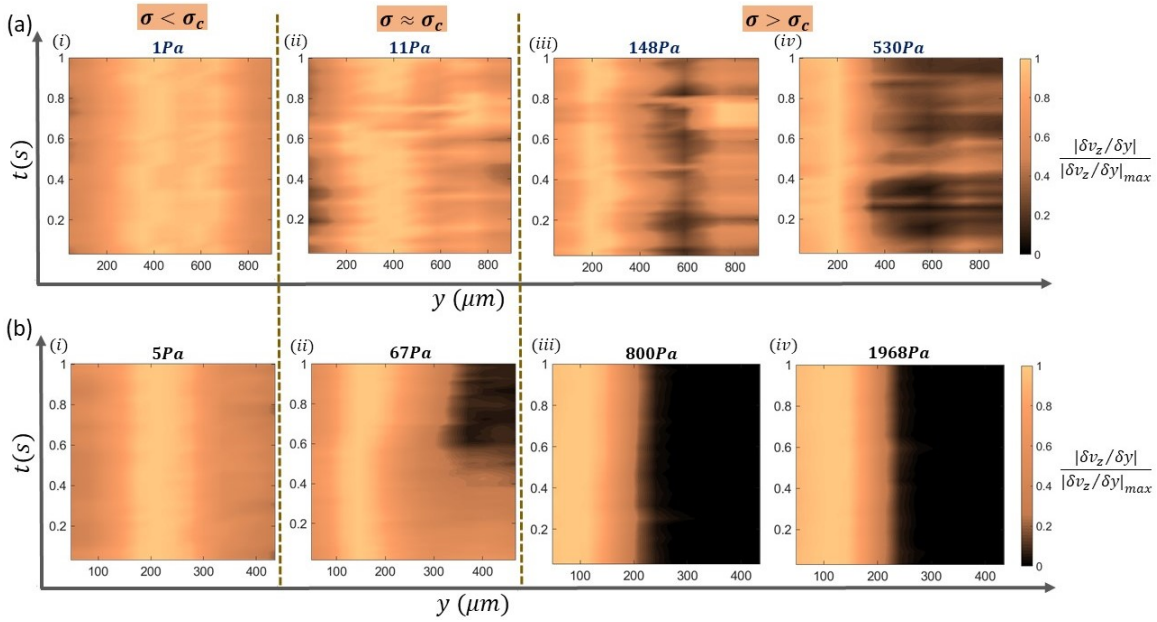

Figure 6.10: Space-time plot (in the y-t plane) of dimensionless velocity gradient (magnitude of the velocity gradient normalized by the maximum value of gradient magnitude as indicated by the color bar) across the shear gap at four different stress values, as mentioned near each panel, for dense suspensions of (a) CS particles at $\phi = 0.54$ and (b) PS particles at $\phi = 0.61$.

We now quantify the spatio-temporal fluctuations in the velocity profile with increasing applied stress, as mentioned above. Figure 6.10 shows the space-time plot (STP) of the magnitude of the normalized velocity gradient across the shear gap. The maximum magnitude of the gradient corresponding to a particular applied stress (σ) is considered to be the normalization factor. Thus, in our case the normalized gradient always remains between 0 and 1. We find that for the lower value of σ ($< \sigma_c$), the spatio-temporal fluctuations of velocity gradient are negligible, as evident from the uniform color in panel(i) of Figure 6.10(a) and 6.10(b). For $\sigma \approx \sigma_c$ when σ approaches 11 Pa and 67 Pa in CS and PS systems, respectively, the spatio-temporal fluctuations get significantly enhanced as reflected by the appearance of patterns in the STP (panel(ii) of Figure 6.10(a) and 6.10(b)). Such enhancement of spatiotemporal fluctuations is reminiscent of the steady

state stress fluctuations at a constant applied shear rate in strongly shear-thickening systems [46, 47, 48]. Such fluctuations originate from the formation and breakage of frictional contacts. In our case, we believe that the spatiotemporal fluctuations in the velocity profile also originate from the local jamming unjamming dynamics. In principle, one can compute a four-point correlation function of the velocity field, which could provide a quantitative measure of dynamic length scales and the extent of correlated motion in space and time—particularly near the crossover stress, where the onset of velocity fluctuations is observed. However, we find that such dynamics are closely linked to the plasticity and failures in the system. It will be interesting to further explore the role of local plasticity in controlling the stress fluctuations reported in the earlier studies. For sufficiently high σ ($>> \sigma_c$), the spatio-temporal fluctuation increases, further leading to the shear band plasticity and fracture in the system (panel(iii) and (iv) of Figure 6.10(a) and 6.10(b)). These observations point out that as the frictional contacts proliferate in the system with increasing σ, the flow becomes more and more heterogeneous, leading to material failure. As mentioned earlier, the details of the plasticity and failure depend on the nature of the sample. We find that for the CS system, the enhancement of fluctuations continues above σ_c. However, for the PS system, just above σ_c, we find a clear fracture where two different regions inside the sample with totally different velocity gradients can be identified, as shown in panels (iii) and (iv) of Figure 6.10(b). We observe that the part near the top plate has a maximum gradient, whereas the other part near the bottom plate has a negligible gradient. Such differences are more clearly visible in the Movies S4 and S5 [27].

6.4 Conclusions

In summary, we study the spatio-temporal flow behavior of two well-studied shear-thickening granular suspensions, in the context of the recently reported universal scaling behavior in shear-thickening systems. Similar to the earlier study, we also observe the power-law scaling in these systems with a cross-over point marking different scaling regimes. Remarkably, our in-situ boundary imaging reveals clear signatures of frictional flow, such as dilation, and positive normal stress, above the critical applied stress corresponding to the scaling cross-over. We observe a significant spatiotemporal fluctuation in the velocity profile associated with the shear-induced plasticity above the stress corresponding to cross-over point. Such spatiotemporal fluctuation in velocity profile might be associated with the growth and dynamics of the rigid clusters as observed in recent studies

[49, 50]. This is because, the local rigid clusters are the precursor of the formation of the jammed state which in turn is essential to observed plasticity in the system. Thus, our study experimentally verifies the transition from lubrication to frictional regime close to the cross-over point as predicted by the universal scaling theory for shear-thickening systems [9, 12]. Interestingly, we find that such one-to-one correlation exists only for granular suspensions. Close to colloidal regime, significant dilation takes place for stress values much beyond the onset stress for shear-thickening due to higher confining stresses in these systems. Thus, from boundary imaging, the visible signature of plasticity and scaling cross-over point do not match in this case (Figure 6.7). Deciphering the role of plasticity in controlling the scaling cross-over point for colloidal systems remains an interesting future direction to explore. Our observation highlights the role of plasticity in changing the slope of the scaling curve from -2 to -1.5. Such change in slope may be linked to the plasticity-induced softening of viscosity divergence in shear jammed dense suspensions [15], where the viscosity-divergence exponent close to jamming is given by a Krieger-Dougherty type relation. However, the generality of such connection needs to be tested for a wider range of shear-thickening systems.

6.5 Appendix

6.5.1 Appendix-1: Movie description

Movie S3 explains the intermittent nature of the dilation around the crossover point stress ($\sigma_c \approx 60\ Pa$) for polystyrene ($d = 8 \pm 4\ \mu m$) dense suspension at $\phi = 0.58$ [27]. The dilation phenomena are reflected in the increase in brightness of the sample boundary image. As the dilation is intermittent in nature around σ_c, this brightness disappears under shear and again reforms.

Movies S4 and S5 explain the flow and deformation behavior of cornstarch dense particulate suspension at $\phi = 0.54$ and polystyrene ($d = 8 \pm 4\ \mu m$) dense particulate suspension at $\phi = 0.61$ respectively [27]. In Movies S4 and S5, we have shown the sample boundary images and corresponding velocity vector images simultaneously for three different stress values at three different regimes of the scaling curve, (i) before the crossover point (ii) during the crossover point (iii) after the crossover point. For the lower stress, before the crossover point, the flow behavior of the sample is almost Newtonian as observed from the velocity vector images, and no change in sample surface intensity is observed. But during the crossover point stress (σ_c) the flow profile starts distorting

in addition to the visible change in sample surface intensity due to dilation. At higher stress, beyond the crossover point, plasticity starts dominating.

All the images are captured using a CMOS camera (Phantom Miro C210) with a $5X$ long working distance objective (Mitutoyo). The images are captured at a frame rate of 100Hz with resolution 1280×720 *pixels* for Movies S3 and S5, and 1280×1024 *pixels* for Movie S4.

6.5.2 Appendix-2: Scaling relation

Using the Wyart-Cates (W-C) model the viscosity η of a shear thickening system can be expressed as

$$\eta(\phi_0 - \phi)^2 \sim \left(\frac{1}{\phi_0 - \phi_m} - \frac{f(\sigma)}{\phi_0 - \phi}\right)^{-2} \tag{6.5}$$

where $f(\sigma) = e^{-\sigma^*/\sigma}$ denotes the fraction of frictional contacts, σ^* is the onset stress for frictional interaction, ϕ_0 is the isotropic jamming point and ϕ_m is the frictional jamming point representing the jamming volume fraction without and with the complete frictional interaction, respectively.

After incorporating careful modifications, such as, multiplying $f(\sigma)$ with $C = \left(\frac{\frac{1}{\phi_0 - \phi_m}}{\frac{f(\sigma)}{\phi_0 - \phi}}\right)$, the equation (6.5) becomes:

$$\eta \sim (\phi_0 - \phi)^{-2} \left(\frac{1}{\phi_0 - \phi_m} - \frac{Cf(\sigma)}{\phi_0 - \phi}\right)^{-2} \tag{6.6}$$

$$\eta \sim \left(\frac{\phi_0 - \phi}{\phi_0 - \phi_m} - Cf(\sigma)\right)^{-2} \tag{6.7}$$

Considering $g(\sigma, \phi) = Cf(\sigma)$

$$\eta(g(\sigma, \phi))^2 \sim \left(\frac{1}{Cf(\sigma)} \frac{\phi_0 - \phi}{\phi_0 - \phi_m} - 1\right)^{-2} \tag{6.8}$$

Taking common $\frac{1}{\phi_0 - \phi_m}$

$$\eta(g(\sigma, \phi))^2 \sim (\phi_0 - \phi_m)^2 \left(\frac{\phi_0 - \phi}{Cf(\sigma)} - (\phi_0 - \phi_m)\right)^{-2} \tag{6.9}$$

$$\sim (\phi_0 - \phi_m)^2 \left(\frac{1}{x} - \frac{1}{x_c}\right)^{-2} \tag{6.10}$$

$$\eta(g(\sigma, \phi))^2 \sim H\left(\left|\frac{1}{x_c} - \frac{1}{x}\right|\right) \tag{6.11}$$

Bibliography

[1] Sachidananda Barik, Akhil Mohanan, and Sayantan Majumdar. Role of plasticity in the universal scaling of shear-thickening dense suspensions. *Rheologica Acta*, pages 1–10, 2024.

[2] H. A. Barnes. Shear-thickening ("dilatancy") in suspensions of nonaggregating solid particles dispersed in newtonian liquids. *Journal of Rheology*, 33(2):329–366, 1989.

[3] Norman J. Wagner and John F. Brady. Shear thickening in colloidal dispersions. *Physics Today*, 62(10):27–32, 2009.

[4] O. Dauchot, G. Marty, and G. Biroli. Dynamical heterogeneity close to the jamming transition in a sheared granular material. *Phys. Rev. Lett.*, 95:265701, Dec 2005.

[5] Giulio Biroli. A new kind of phase transition? *Nature Physics*, 3:222–223, 2007.

[6] Carl P. Goodrich, Andrea J. Liu, and Sidney R. Nagel. Finite-size scaling at the jamming transition. *Phys. Rev. Lett.*, 109:095704, Aug 2012.

[7] Ryohei Seto, Romain Mari, Jeffrey F. Morris, and Morton M. Denn. Discontinuous shear thickening of frictional hard-sphere suspensions. *Phys. Rev. Lett.*, 111:218301, Nov 2013.

[8] M. Wyart and M. E. Cates. Discontinuous shear thickening without inertia in dense non-brownian suspensions. *Phys. Rev. Lett.*, 112:098302, Mar 2014.

[9] Meera Ramaswamy, Itay Griniasty, Danilo B. Liarte, Abhishek Shetty, Eleni Katifori, Emanuela Del Gado, James P. Sethna, Bulbul Chakraborty, and Itai Cohen. Universal scaling of shear thickening transitions, 2021.

[10] Romain Mari, Ryohei Seto, Jeffrey F. Morris, and Morton M. Denn. Shear thickening, frictionless and frictional rheologies in non-brownian suspensions. *Journal of Rheology*, 58(6):1693–1724, 2014.

[11] John Cardy. *Scaling and Renormalization in Statistical Physics*, volume 5 of *Cambridge Lecture Notes in Physics*. Cambridge University Press, 1996.

[12] Nelya Malbranche, Aritra Santra, Bulbul Chakraborty, and Jeffrey F. Morris. Scaling analysis of shear thickening suspensions. *Frontiers in Physics*, 10, 2022.

[13] Meera Ramaswamy, Itay Griniasty, James P Sethna, Bulbul Chakraborty, and Itai Cohen. Incorporating tunability into a universal scaling framework for shear thickening. *arXiv preprint arXiv:2205.02184*, 2022.

[14] C. K. Sarika, Sayantan Majumdar, and A. K. Sood. Shear jamming and fragility in fractal suspensions under confinement. *Soft Matter*, 18:8813–8819, 2022.

[15] Subhransu Dhar, Sebanti Chattopadhyay, and Sayantan Majumdar. Signature of jamming under steady shear in dense particulate suspensions. *Journal of Physics: Condensed Matter*, 32(12):124002, dec 2019.

[16] Sachidananda Barik and Sayantan Majumdar. Origin of two distinct stress relaxation regimes in shear jammed dense suspensions. *Phys. Rev. Lett.*, 128:258002, Jun 2022.

[17] Sebanti Chattopadhyay, Sharadhi Nagaraja, and Sayantan Majumdar. Effect of adhesive interaction on strain stiffening and dissipation in granular gels undergoing yielding. *Communications Physics*, 5(1):126, 2022.

[18] Sebanti Chattopadhyay, Sharadhi Nagaraja, and Sayantan Majumdar. Effect of adhesive interaction on strain stiffening and dissipation in granular gels undergoing yielding. *Communications Physics*, 5:126, 05 2022.

[19] Swarnadeep Bakshi, Vaisakh V M, Ritwick Sarkar, and Sayantan Majumdar. Strain localization and yielding dynamics in disordered collagen networks. *Soft Matter*, 06 2021.

[20] Sebanti Chattopadhyay and Sayantan Majumdar. Inter-particle adhesion induced strong mechanical memory in a dense granular suspension. *The Journal of chemical physics*, 156, 06 2022.

[21] Eric Brown and Heinrich M. Jaeger. The role of dilation and confining stresses in shear thickening of dense suspensions. *Journal of Rheology*, 56(4):875–923, 2012.

[22] Rijan Maharjan, Ethan O'Reilly, Thomas Postiglione, Nikita Klimenko, and Eric Brown. Relation between dilation and stress fluctuations in discontinuous shear thickening suspensions. *Phys. Rev. E*, 103:012603, Jan 2021.

[23] Varghese Babu, Deng Pan, Yuliang Jin, Bulbul Chakraborty, and Srikanth Sastry. Dilatancy, shear jamming, and a generalized jamming phase diagram of frictionless sphere packings. *Soft Matter*, 17:3121–3127, 2021.

[24] MI Smith, R Besseling, ME Cates, and V Bertola. Dilatancy in the flow and fracture of stretched colloidal suspensions. *Nature communications*, 1(1):114, 2010.

[25] Malcolm Whitlock. Flow behavior of concentrated (dilatant) suspensions. *Transactions of the Society of Rheology*, 2(1):239–254, 1958.

[26] Vincent T. O'Brie and Michael E. Mackay. Stress components and shear thickening of concentrated hard sphere suspensions. *Langmuir*, 16(21):7931–7938, 2000.

[27] http://hdl.handle.net/2289/8300.

[28] Anugrah Singh, Avinoam Nir, and Raphael Semiat. Free-surface flow of concentrated suspensions. *International Journal of Multiphase Flow*, 32(7):775–790, 2006.

[29] Bhaskar Jyoti Medhi, A. Ashok Kumar, and Anugrah Singh. Apparent wall slip velocity measurements in free surface flow of concentrated suspensions. *International Journal of Multiphase Flow*, 37(6):609–619, 2011.

[30] Thomas Loimer, Avinoam Nir, and Raphael Semiat. Shear-induced corrugation of free interfaces in concentrated suspensions. *Journal of Non-Newtonian Fluid Mechanics*, 102(2):115–134, 2002. A Collection of Papers Dedicated to Professor ANDREAS ACRIVOS on the Occasion of his Retirement from the Benjamin Levich Institute for Physiochemical Hydrodynamics and the City College of the CUNY.

[31] A Ashok Kumar, Bhaskar Jyoti Medhi, and Anugrah Singh. Experimental investigation of interface deformation in free surface flow of concentrated suspensions. *Physics of Fluids*, 28(11), 2016.

[32] BRIAN D. TIMBERLAKE and JEFFREY F. MORRIS. Particle migration and free-surface topography in inclined plane flow of a suspension. *Journal of Fluid Mechanics*, 538:309–341, 2005.

[33] Eric Brown and Heinrich M Jaeger. Shear thickening in concentrated suspensions: phenomenology, mechanisms and relations to jamming. *Reports on Progress in Physics*, 77(4):046602, apr 2014.

[34] Abhinendra Singh, Christopher Ness, Ryohei Seto, Juan J de Pablo, and Heinrich M Jaeger. Shear thickening and jamming of dense suspensions: The "roll" of friction. *Physical Review Letters*, 124(24):248005, 2020.

[35] Cécile Clavaud, Antoine Bérut, Bloen Metzger, and Yoël Forterre. Revealing the frictional transition in shear-thickening suspensions. *Proceedings of the National Academy of Sciences*, 114(20):5147–5152, 2017.

[36] Jean Comtet, Guillaume Chatté, Antoine Nigues, Lydéric Bocquet, Alessandro Siria, and Annie Colin. Pairwise frictional profile between particles determines discontinuous shear thickening transition in non-colloidal suspensions. *Nature communications*, 8(1):15633, 2017.

[37] Vikram Rathee, Daniel L Blair, and Jeffrey S Urbach. Localized stress fluctuations drive shear thickening in dense suspensions. *Proceedings of the National Academy of Sciences*, 114(33):8740–8745, 2017.

[38] Vikram Rathee, Joia Miller, Daniel L Blair, and Jeffrey S Urbach. Structure of propagating high-stress fronts in a shear-thickening suspension. *Proceedings of the National Academy of Sciences*, 119(32):e2203795119, 2022.

[39] Vikram Rathee, Daniel L Blair, and Jeffrey S Urbach. Localized transient jamming in discontinuous shear thickening. *Journal of Rheology*, 64(2):299–308, 2020.

[40] WH Boersma, PJM Baets, Jozua Laven, and HNj Stein. Time-dependent behavior and wall slip in concentrated shear thickening dispersions. *Journal of Rheology*, 35(6):1093–1120, 1991.

[41] R. N. Chacko, R. Mari, M. E. Cates, and S. M. Fielding. Dynamic vorticity banding in discontinuously shear thickening suspensions. *Phys. Rev. Lett.*, 121:108003, Sep 2018.

[42] Bruno Etcheverry, Yoël Forterre, and Bloen Metzger. Capillary-stress controlled rheometer reveals the dual rheology of shear-thickening suspensions. *Phys. Rev. X*, 13:011024, Feb 2023.

[43] John R. Royer, Daniel L. Blair, and Steven D. Hudson. Rheological signature of frictional interactions in shear thickening suspensions. *Phys. Rev. Lett.*, 116:188301, May 2016.

[44] Abhinendra Singh and Kuniyasu Saitoh. Scaling relationships between viscosity and diffusivity in shear-thickening suspensions. *Soft Matter*, 19(35):6631–6640, 2023.

[45] Ivo R Peters, Sayantan Majumdar, and Heinrich M Jaeger. Direct observation of dynamic shear jamming in dense suspensions. *Nature*, 532(7598):214–217, 2016.

[46] Omer Sedes, Abhinendra Singh, and Jeffrey F Morris. Fluctuations at the onset of discontinuous shear thickening in a suspension. *Journal of Rheology*, 64(2):309–319, 2020.

[47] Qin Xu, Abhinendra Singh, and Heinrich M Jaeger. Stress fluctuations and shear thickening in dense granular suspensions. *Journal of Rheology*, 64(2):321–328, 2020.

[48] Michiel Hermes, Ben M Guy, Wilson CK Poon, Guilhem Poy, Michael E Cates, and Matthieu Wyart. Unsteady flow and particle migration in dense, non-brownian suspensions. *Journal of Rheology*, 60(5):905–916, 2016.

[49] Michael van der Naald, Abhinendra Singh, Toka Tarek Eid, Kenan Tang, Juan J de Pablo, and Heinrich M Jaeger. Minimally rigid clusters in dense suspension flow. *Nature Physics*, pages 1–7, 2024.

[50] Abhay Goyal, Nicos S Martys, and Emanuela Del Gado. Flow induced rigidity percolation in shear thickening suspensions. *arXiv preprint arXiv:2210.00337*, 2022.

CHAPTER

SEVEN

Summary and outlook

"Our reason cannot sound life's mighty sea
And only counts its waves and scans its foam"
- Sri Aurobindo -

This chapter summarizes the key findings of this thesis and discusses the potential open direction for future research.

In this thesis, we broadly explore three different aspects of shear thickening and shear jamming phenomena using various dense particulate suspensions. (1) Stress relaxation and its connection with the structural relaxation (Chapters 3 and 4), (2) The effect of fractality and complex internal structure of the particle (Chapter 5), (3) Flow and deformation behavior in connection to the universal scaling approach (Chapter 6).

First, we study the relaxation dynamics of the shear-jammed state formed under the transient perturbation. We observed that the nature of stress relaxation strongly depends on the magnitude of the shear stress developed in the system under step strain perturbation. We find a transition in relaxation behavior from a smooth single-step relaxation to a discontinuous two-step relaxation process, as the stress developed in the system goes beyond a certain threshold. Using the in-situ boundary imaging technique we investigate the microscopic mechanism controlling such discontinuous relaxation behavior. We conclude that the sharp discontinuous stress drop is associated with the particle scale plasticity formed due to the high stress in the system and the slow relaxation process is governed by the relaxation of the internal force chain network as reflected in the relaxation of the dilation in the system. We further establish a correlation between the transient relaxation behavior with the steady-state shear jamming phase diagram obtained from the Wyart-Cates model. In the future, it will be interesting to explore the dynamics of such microscopic plasticity under different shearing conditions. We show that these localized plastic centers combined together to create the macroscopic fracture in the system, however, in a shear-jammed system, the exact mechanism of the fracture formation and its relaxation remains open for a future exploration. Also, the importance of particle shape and surface morphology on the relaxation behavior needs to be explored in detail.

Furthermore, we explore the effect of the drastic stress relaxation over the structural relaxation of the shear-jammed state. We observe an enhancement in the mechanical response under unidirectional repetitive step-strain perturbation; whereas the response becomes weak under alternative reverse direction perturbation. This highlights that the internal structure of the system retains the information of the previous shear-jammed state even after the orders of magnitude stress relaxation. We find that such novel memory effect is only observed for the volume fraction range required for shear jamming. Using the shear reversal experiment and simulation we find that the formation of shear-induced rigid clusters can potentially explain such novel memory effect in shear-jammed dense suspension. Although we observed that such memory effect is not very prominent in

smaller size particles, the effect of Brownian motion in a very dense environment and its effects on the rigid cluster formation need to be explored in detail. In the future, it will be interesting to explore various aspects that control the strength of memory and various means to encode and erase structural memories in the system.

Next, we study the shear-thickening behavior in the dense suspension of hydrophilic fumed silica particles of different fractality and internal structures. We find that, unlike the non-fractal system, the shear thickening is observed at a significantly lower volume fraction, and, the shear thickening onset stress increases exponentially with the volume fraction. Furthermore, for certain types of fumed silica systems, we observe a reversible weakening in the ST response at higher stress values which is again sensitive to the volume fraction of the system. We explain the mechanism of these interesting observations based on the complex internal structure and fractality of the fumed silica particles. In the future, the reversible weakening of the ST response needs to be explored in detail by looking at the flow and deformation behavior around that region. Due to the smaller particle size and the transparent nature of the sample our optical boundary imaging technique is limited to explore beyond the macroscopic flow field. So it will be interesting to investigate the shear-induced structural change using more sophisticated techniques like small angle X-ray scattering under shear.

Finally, we explored the recently proposed universal scaling theory for shear thickening or shear jamming systems. We study the flow and deformation behavior in different scaling regimes using the in-situ boundary imaging technique. Beyond the stress corresponding to the crossover point in the scaling curve, we observe that the flow behavior is controlled by friction-dominated phenomena such as granular dilation and shear band plasticity. Our experimental findings provide evidence that the crossover point on the scaling curve indicates the transition from the frictionless to the frictional regime, as previously predicted in theoretical models. Although this one-to-one correlation exists well for the granular system, for the colloidal system it does not. In a colloidal system, the role of friction-dominated phenomena in controlling the change in the slope of the scaling curve remains as a possible open direction to explore.

Additionally, it will also be interesting to explore the shear-induced annealing in the shear-jammed system and its effect on the onset of shear thickening, granular dilation, and plasticity. Again, understanding the microscopic mechanism of yielding in the shear-jammed system, in comparison to the static-jammed system, also presents an intriguing direction for future exploration.